2024

Shocks and cold fronts in merging galaxy clusters

Purva Diwanji

SHOCKS AND COLD FRONTS IN MERGING GALAXY CLUSTERS

Purva Diwanji

A DISSERTATION

Submitted in partial fulfillment of the requirements
for the degree of Doctor of Philosophy
in
The Department of Physics & Astronomy
to
The Graduate School
of
The University of Alabama in Huntsville

May 2024

Approved by:

Dr. Stephen A. Walker, Research Advisor/Committee Chair
Dr. Ming Sun, Committee Member
Dr. Max Bonamente, Committee Member
Dr. Richard Lieu, Committee Member
Dr. James Miller, Department Chair
Dr. Rainer Steinwandt, College Dean
Dr. Jon Hakkila, Graduate Dean

Abstract

SHOCKS AND COLD FRONTS IN MERGING GALAXY CLUSTERS

Purva Diwanji

A dissertation submitted in partial fulfillment of the requirements for the degree of Doctor of Philosophy

Physics & Astronomy

The University of Alabama in Huntsville

May 2024

Galaxy clusters, found at the nodes of the large-scale structures in the universe, are the most massive gravitationally bound and virialized structures in the Universe. They are formed via accretion, gravitational infall, and hierarchical mergers of smaller sub-clusters and galaxy groups. Mergers of galaxy clusters are the most energetic events in the Universe after the Big Bang, wherein the sub-clusters collide at velocities of $\sim$ 1000km/s, releasing energy of the order of 10^{64} ergs. During such a merger, the galaxies and dark matter of both clusters interact only gravitationally and move unhindered through the region of the collision. This dissertation presents the findings from the new deep Chandra observations (256 ks) of the merging galaxy cluster SPT-CLJ 2031-4037. The observations reveal intricate structures seen in a major merger akin to the Bullet Cluster. The X-ray data confirm the existence of two shock fronts, one to the northwest and one to the southeast, by directly measuring the temperature jump of gas across the surface brightness edges. The stronger shock front in the northwest has a density jump of 3.11 ± 0.32 across the sharp surface brightness edge and a Mach number $M = 3.23^{+0.89}_{-0.56}$, which makes this cluster one of the rare merging systems with a Mach number M>2. The northwestern shock is

compared with two models for shock heating - the instant heating model and the Coulomb collisional heating model, and it is determined that the temperatures across the shock front agree with the Coulomb collisional model of heating. For the shock front in the southeastern region, there is a density jump of 1.53 ± 0.14 and a Mach number $M = 1.36^{+0.09}_{-0.08}$. In addition, I will also present new results of cold fronts in the nearby Perseus Cluster, which are also produced by galaxy cluster merging activity, and provide insights into its merger history.

Acknowledgements

I want to express my heartfelt gratitude to my advisor, Dr. Stephen Walker, for his exceptional guidance, unwavering support, and infinite patience. He introduced me to X-ray Astronomy, taught me how to do interesting research, and molded me to become the best version of myself as an astronomer. He is one of the most hard-working and brilliant people I know and is equally kind and understanding. The countless hours spent in discussions with him have fostered my academic and personal growth tremendously. I am fortunate that I completed my Ph.D. under his mentorship, and I hope that I have imbibed all the qualities of a good scientist from him. His expertise, dedication, and attention to detail have played a pivotal role in the development of this dissertation as well as my entire research journey.

I also want to thank all the members of Dr. Walker's research group - Dipika, Leo, Sierra, and Mathew for creating an environment of shared knowledge, stimulating discussions, and camaraderie, which have contributed tremendously to my work. I am especially thankful to the post-doctoral researchers in the group, Dr. Mohammad Mirakhor and Dr. James Runge. Their guidance and willingness to share their experiences have been invaluable for the progress of my research.

I am deeply grateful to Dr. Miller for supporting me since the day I joined the department, to Dr. Lieu for imparting knowledge that goes far beyond the scope of any syllabus, to Dr. Sun for introducing me as a potential Ph.D. student to Dr. Walker, and Dr. Bonamente for showing me the importance of statistics in my research.

I would like to extend my heartfelt appreciation to Dr. Raghu for his invaluable mentorship and guidance throughout my academic journey. Dr. Raghu not only served as a mentor but also played a pivotal role in igniting the idea of pursuing a

Ph.D. in the United States. His unwavering support and belief in my potential have been instrumental in my pursuit of higher education.

I also wish to pay tribute to the late Dr. Pandya and the late Dr. Vyas, who laid the solid foundation of my understanding of physics. Their teachings and continuous support have significantly shaped my academic path. Despite their untimely departures, their influence on my educational and intellectual growth will forever be cherished.

I want to express my heartfelt appreciation to Ms. Colleen, Ms. Dora, Charlene, and Krissy for always going above and beyond to help me with all the paperwork and for being available whenever I had any concerns, academic or personal.

I want to thank my parents for going against all societal norms and supporting my goals and dreams always. I am forever indebted to them for all the sacrifices they have made for me. They have been my pillars of strength during this journey, and their confidence in me is the driving force of my success. I hope to make them proud always.

Most importantly, I would like to thank my husband, Kirtan, who has been the greatest source of encouragement. I am fortunate to have him as my partner in both life and academia. Together, we spent countless nights studying, shared moments of frustration, and celebrated victories while always being there for each other. His unconditional love and support have been instrumental to my success.

I could not have accomplished my goals without the blessings of my grandparents, Maa, Nana, Dada, and Daadi. Maa and Daadi paved the path that I walk on today. I am deeply indebted to my aunts - Fiya, Sonumasi, and Rupalmasi, for all their sacrifices and unwavering emotional support throughout my Ph.D. journey. I also want to thank Fuvaji and Jiju for always believing in me and Heer, Meet, and Manasvat for instilling confidence in me.

I am profoundly grateful to have met some of my closest friends at this department - Christina (who constantly inspires and amazes me), Kelsey and Adam (who taught me how to survive in this country), Matt (for all the Netflix binge sessions), Tim, Grant, Jared and Kiley (for some of the best nights spent playing Dungeons and Dragons), Sam and Rachel (my very own "Women in Astrophysics" gang), and Hemang and Amruta (whose house was practically a second home for me).

I want to express the most heartfelt gratitude to the best supporting squad one could ask for this journey - Manushi, Miloni, Khushboo, Jharna, Dhruvi and Irene. They never let me have self-doubts, constantly checked on me, and always believed in me.

I would be remiss not to mention Lydia Shull, Olivia Merical, Raven Hodges and Emily Eichhorn for helping me overcome some of my biggest struggles throughout this journey.

Finally, and most importantly, I want to thank my cats, Charlie and Zoey. Charlie always sat by me for every late-night assignment, every all-nighter before exams, all online classes, and every minute of dissertation writing. Zoey's constant purring and hilarious antics provided much-needed stress relief. Their unspoken support carried me through some of my toughest moments and made my journey a million times better.

Dedication

To Mamma and Daddy

Thank you for continuously instilling me with strength and courage, for your unwavering faith in me, and for consistently being my support. Everything that I have become today, I owe entirely to you.

Table of Contents

List of Figures

List of Tables

List of Symbols

Symbol	Description
P	Pressure
T	Temperature
α	Pitch angle in Synchrotron radiation
β	Ratio of thermal pressure to magnetic pressure
b	Impact parameter
k	Boltzmann constant
B	Magnetic Field strength

Chapter 1. Introduction

1.1 Galaxy Clusters

Galaxy clusters are the most massive gravitationally bound and virialized ($E_{th} = -\frac{E_{grav}}{2}$) structures in the Universe. They consist of anywhere from hundreds of galaxies (poor clusters) to thousands of galaxies (rich clusters) bound together. The mass of galaxy clusters is typically of the order of $\sim 10^{14} M_{\odot}$ - $10^{15} M_{\odot}$ of which dark matter constitutes roughly 84%, around 13% is in the intracluster medium, which also contains most of the baryonic matter and the remaining 3% in the stars of the galaxies. The ICM has gas densities ranging from 10^{-5} cm^{-3} in the outskirts of the cluster to about 10^{-1} cm^{-3} in the central regions. Observations by *Uhuru* (the first X-ray satellite) indicate that clusters of galaxies are the most common bright extragalactic X-ray sources, and they are extremely luminous in their X-ray emission, with luminosities of $10^{43} - 10^{45} ergs\ s^{-1}$ (Sarazin, 1986). Figure 1.1 illustrates the composite image of the Coma cluster in optical and X-ray wavelengths. This image was obtained by combining results from the Sloan Digital Sky Survey (SDSS) and *Chandra* X-ray Observatory. The yellow specks are the galaxies observed at the optical wavelengths. The purple blob in the center is the hot ICM, which emits in X-ray owing to its very high temperature.

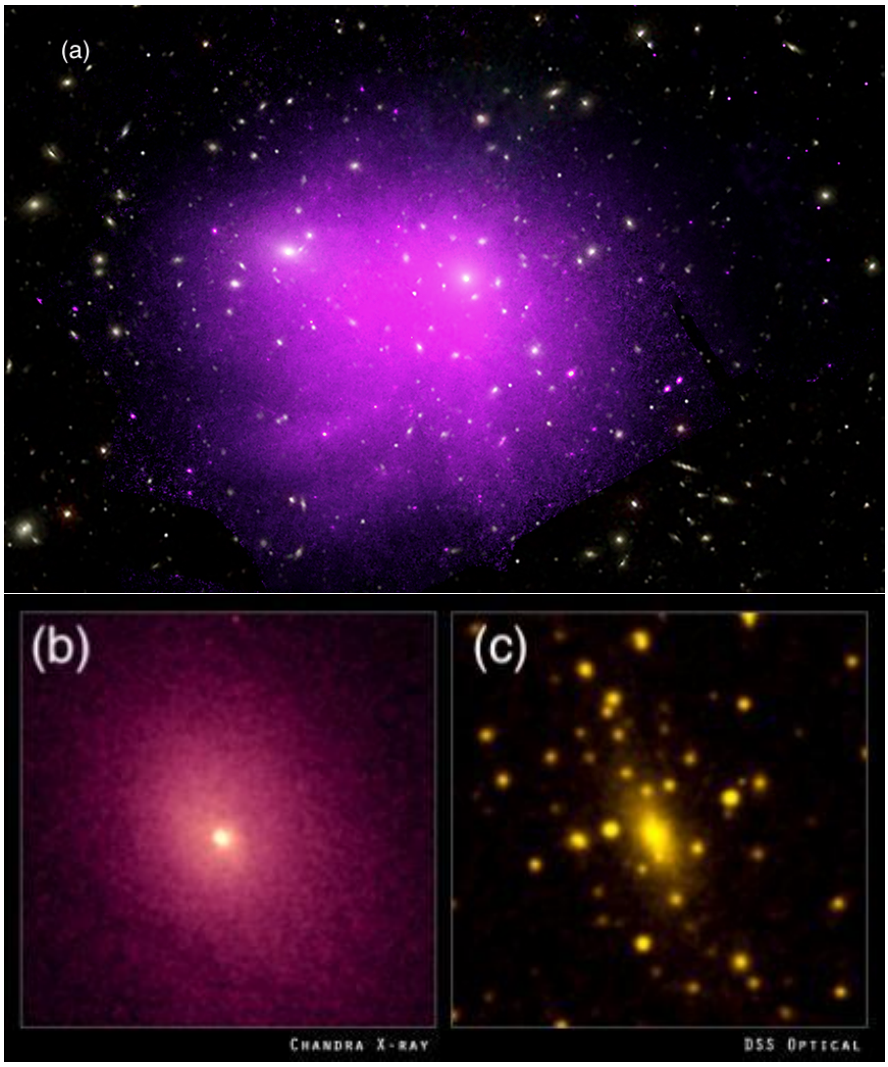

Figure 1.1: A composite image of the Coma cluster in the optical and X-ray wavelengths, obtained from the Sloan Digital Sky Survey and NASA's *Chandra* X-ray telescope, respectively. The galaxies (yellow flecks) are apparent at visible wavelengths but are not seen in X-ray as they do not emit a significant amount of X-ray radiation. The galaxies are spread out over the entire cluster, with the older, elliptical galaxies closer to the center of the cluster and younger spiral galaxies in the outskirts. The giant purple blob in the center is the Intracluster Medium (ICM), the hot, X-ray luminous plasma that contains the majority of the baryonic matter of the cluster. It forms about $12 - 13\%$ of the cluster mass. (Image obtained from *Chandra*).

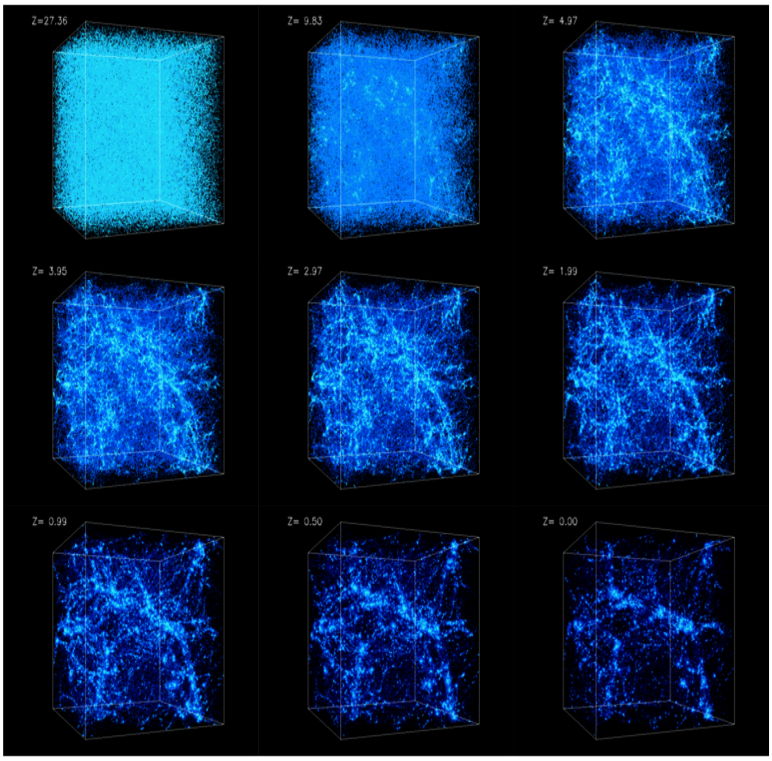

Figure 1.2: The image shows the evolution of structure formation in the Universe using the ΛCDM model in a 43 Mpc box from a redshift $z \sim 30$ to the present time, $z \sim 0$. Initially, the distribution of matter appears to be uniform, but as time goes on, perturbations cause the matter to coalesce. With the passage of time, the filaments grow and become increasingly distinct and eventually form the cosmic web observed today. The simulations were performed at the National Center for Supercomputer Applications by Andrey Kravtsov (The University of Chicago) and Anatoly Klypin (New Mexico State University). Visualizations are by Andrey Kravtsov and can be found here.

Galaxy clusters are high-density structures resulting from the initial perturbations in the early universe. Most of them have only recently undergone gravitational collapse and can be observed at the intersections of the filaments in the Cosmic web. The panels in Figure 1.2 show the evolution of structure formation in the Universe from redshift $z \sim 30$ to $z \sim 0$ according to ΛCDM cosmology.

As seen in the figure, initially, there is a uniform distribution of particles, but as time passes, they coalesce and form filaments of the cosmic web observed today.

1.2 Dark Matter

Dark matter constitutes a major part of galaxy clusters. The first evidence of the existence of Dark Matter was provided in 1933 by Fritz Zwicky, whose calculations of the mass of the galaxies within the Coma cluster from the observed values far exceeded the value estimated from the luminosity of its galaxies. This was the first indication that Dark Matter was holding the galaxies together in the galaxy clusters (Andernach and Zwicky, 2017).

The Bullet Cluster (1E0657-56) is one of the most well-known cluster mergers observed so far because of the strong shock observed and the geometry of the merger (Markevitch, 2006a). Figure 1.3 shows a composite image of the Bullet Cluster in visible and X-ray wavelengths as captured by the Hubble Space Telescope (HST) and *Chandra* Observatory, respectively. The image shows a collision between two galaxy clusters, where the regions with the reddish hue represent the ICM, and the blue region indicates the dark matter corresponding to each galaxy cluster. Since Dark Matter interacts only through gravitational force, it passes through the region of the merger without any distortion. The X-ray emitting plasma consists of particles that interact via gravitational and electromagnetic forces, which causes it to lag behind, resulting in an offset from the dark matter. The gravitational lensing around the Bullet Cluster indicates the presence of mass on the outskirts of the merger. The most visible (or luminous) matter, however,

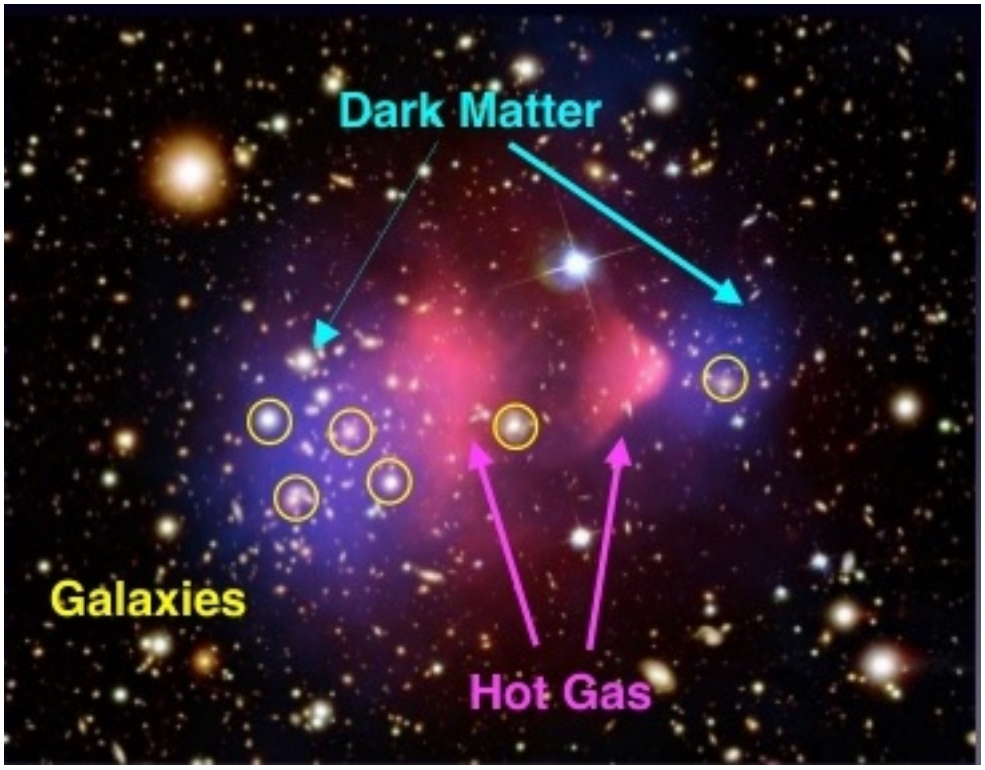

Figure 1.3: The Bullet Cluster is one of the most powerful pieces of observational evidence of the existence of Dark Matter. Figure 1.3 shows a composite image of the Bullet Cluster in visible and X-ray wavelengths as captured by the Hubble Space Telescope (HST) and *Chandra* Observatory, respectively. The image shows a collision between two galaxy clusters, where the regions with the reddish hue represent the ICM, and the blue region indicates the dark matter corresponding to each galaxy cluster. (Credit: X-ray: NASA/CXC/CfA/M.Markevitch et al.; Optical: NASA/STScI; Magellan/U.Arizona/D. Clowe et al.; Lensing Map: NASA/STScI; ESO WFI; Magellan/U.Arizona/D.Clowe et al.)

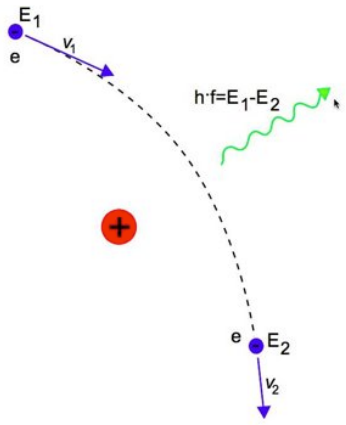

Figure 1.4: The ICM emits in X-ray via thermal Bremsstrahlung. Bremsstrahlung radiation is produced when electrons are accelerated in a field of ions, typically in an ionized plasma like the ICM.

lies in the center. This offset between the X-ray and the lensing is strong evidence for the existence of dark matter.

1.3 The Intracluster Medium (ICM)

Although Galaxy Clusters contain hundreds of galaxies, the majority of the baryonic mass lies in the ICM. The ICM is a hot ionized plasma that permeates a galaxy cluster. It consists mainly of ionized hydrogen and helium and contains most of the baryonic matter of the cluster. The metallicity of the ICM ranges from a third to half of the Sun's metallicity (Mantz et al., 2017). The temperature of the ICM typically ranges from 10^7 - 10^8 K. The particle density of the ICM varies from 10^{-1} cm^{-3} in the central regions of the cluster to $\sim 10^{-4}$ cm $^{-3}$ in the outskirts. The characteristic luminosity of X-ray emission from the clusters lies between 10^{43} - 10^{45} ergs s^{-1}.

The ICM mainly emits in the X-ray via the thermal Bremsstrahlung process. Bremsstrahlung radiation is produced by the acceleration of electrons in a field of ions, for example, an ionized plasma like the ICM. The X-ray emission from thermal bremsstrahlung is characterized by a continuous spectrum that extends to high energies. The intensity of the emission depends on the density and temperature of the ICM, as well as the number of high-energy electrons present. By analyzing the X-ray emission from thermal bremsstrahlung, it is possible to determine the temperature, density, and metallicity of the ICM (Takizawa, 1999).

The approximations made here are (Peterson and Fabian, 2006):

1. The photons are assumed to be free of any interactions with the electrons or the ions once they are created.

2. It is assumed that the electron and radiation densities are low enough that the rate of radiative decay is much higher than the rate of electron density-dependent collisional excitation, further leading to the assumption that the ionized atoms can be treated as if all their electrons are in the ground state.

3. The final approximation is that the electrons and ions have a Maxwellian distribution and have achieved a common temperature.

The power per unit volume per unit energy is given approximately by:

$$\frac{d^2P}{dVdE} \approx 10^{-11} n_e n_H T^{-\frac{1}{2}} e^{-\frac{E}{kT}} \text{ cm}^{-3} \text{ s}^{-1}, \tag{1.1}$$

where n_e and n_H are the electron and Hydrogen densities, respectively, T is the electron temperature (because it is not possible to measure the temperature of the ions), and E is the photon energy.

Integrating over all frequencies, the total power per unit volume is:

$$\frac{dP}{dV} = 10^{-27} n_e n_H T^{\frac{1}{2}} \text{ergs cm}^{-3}\text{s}^{-1}. \tag{1.2}$$

Hence, the emission is directly proportional to gas density squared.

1.4 Shocks

Galaxy Clusters are formed due to hierarchical mergers of smaller sub-clusters (Press and Schechter, 1974). Mergers of galaxy clusters are the most energetic events in the Universe after the Big Bang, wherein the sub-clusters collide at velocities of $\sim 10^3$ km s^{-1}, releasing energy of the order of 10^{64} ergs. This energy is dissipated into the ICM via shocks and turbulence and may also cause acceleration of ultrarelativistic particles (Markevitch and Vikhlinin, 2007). When accelerated particles move through a medium at a supersonic speed, they cause the medium to compress and heat up, forming a shock wave (or a bow shock). Shocks (or shock waves) are surface discontinuities consisting of a separation between two fluids (Vietri, 2008). Although the two fluids are separate, there is a flux of mass, momentum, and energy between them. The strength of a shock is determined by its Mach number, M.

When a disturbance propagates through a medium at a higher rate than the sound speed in that medium, shock waves occur. The Mach Number (M)

is a dimensionless quantity used to study such shock waves. It is defined as the ratio of the speed of the disturbance passing through a medium (u) to the speed of sound in the medium (v_s):

$$M = \frac{u}{v_s}. \tag{1.3}$$

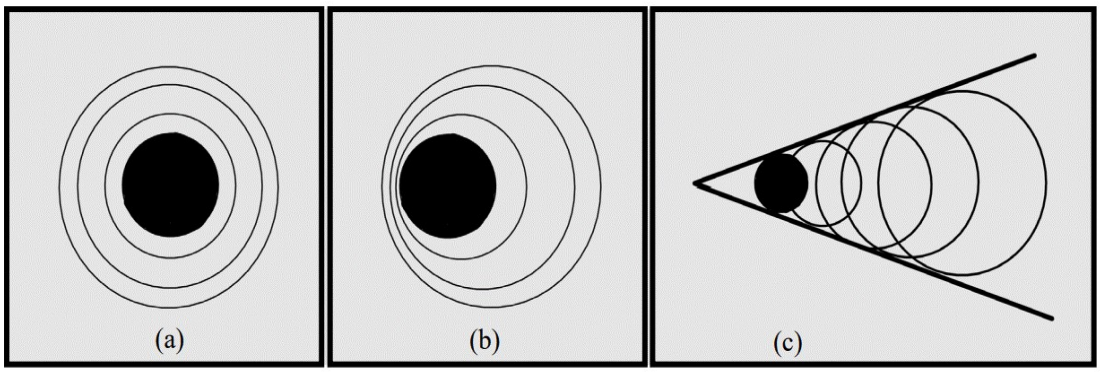

Figure 1.5: This figure shows how circular wavefronts emitted by a point source move, depending on the speed of the source. Panel (a) shows uniform wavefronts when the source is stationary. Panel (b) shows how these wavefronts compress and elongate in front of and behind the moving emitter respectively. As the speed of the source increases, the wavefronts start to overlap constructively. As the speed becomes $u > v_s$, or as $M >= 1$, these wavefronts form a single conical-shaped wavefront seen in panel (c).

Figure 1.5 indicates the development of a Mach cone. (a) represents a point source that emits acoustic waves while it is stationary. As it starts moving, it emits circular waves with the waves in front of it compressed while the ones behind it are elongated, as shown in (b). These circular wavefronts then start to overlap when $u > v_s$. This implies that the speed of the propagation of the

disturbance is supersonic, or $M \geq 1$. As shown in (c), a Mach cone forms when the object starts moving at supersonic speeds.

Shocks cause irreversible changes in the thermodynamic properties (pressure (P), density (ρ), and temperature (T)) of a fluid. A shock front may be considered as a discontinuity across which there is an abrupt change in these fundamental quantities because of the motion of the shock.

Figure 1.6 shows a shock front in the rest frame of the undisturbed gas on the left and the rest frame of the shock front (shock frame) on the right side. In the rest frame of the undisturbed gas, the shock front moves with a velocity w, and the shocked gas moves with a velocity w_2 ($w > w_2$). The shock is observed here because the shock front moves with a velocity $w > v_{s1}$, where v_{s1} is the speed of sound in the undisturbed gas. In the shock frame, the shocked gas moves away from the shock front with velocity v_2 and the undisturbed gas moves towards the shock front with velocity v_1.

In the rest frame of the shock, the following laws of conservation of mass, momentum, and energy are applicable (Blundell and Blundell, 2010):

Conservation of mass: The mass flux Φ_m, *i.e.*, the mass crossing unit area in unit time, is equal on both sides of the shock and is denoted by

$$\rho_1 \left|\vec{v}\right|_1 = \rho_2 \left|\vec{v}\right|_2 = \Phi_m, \tag{1.4}$$

where ρ_1, ρ_2 = pre- and post-shock gas densities and $\vec{v_1}, \vec{v_2}$ = pre- and post-shock velocities respectively.

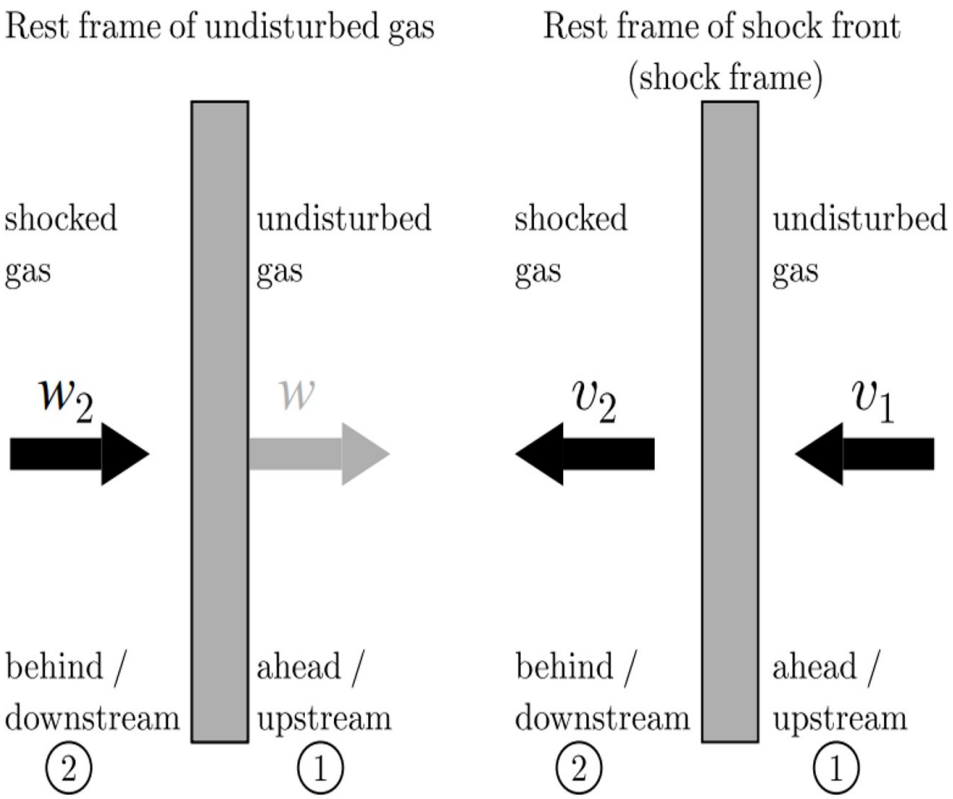

Figure 1.6: The figure from (Blundell and Blundell, 2010) shows the structure of a shock front in the rest frame of the undisturbed gas on the left and the rest frame of the shock front (shock frame) on the right side. With respect to the shock frame, region 1 consists of the undisturbed 'upstream' gas, and region 2 contains the shocked 'downstream' gas. The gas in region 1 (pre-shock region) has lower pressure P, temperature T, and density ρ but higher velocity $\vec{v}$ than the shocked gas in region 2 (post-shock region).

Conservation of momentum: The momentum flux, i.e., the force per unit area(P) in unit time, and the rate at which the momentum is transported across the unit area ($\rho\vec{v}$) is equal on both sides of the shock front:

$$P_1 + \rho_1 \left|\vec{v}\right|_1^2 = P_2 + \rho_2 \left|\vec{v}\right|_2^2 , \tag{1.5}$$

where P_1, P_2 = pre- and post-shock gas pressures respectively.

Conservation of energy: The rate at which gas pressure does work per unit area and the rate of transport of internal and kinetic energy per unit area is constant across the shock front:

$$P_1 \left|\vec{v}\right|_1 + (\rho_1 \tilde{u_1} + \frac{1}{2}\rho_1 \left|\vec{v}\right|_1^2) \left|\vec{v}\right|_1 = P_2 \left|\vec{v}\right|_2 + (\rho_2 \tilde{u_2} + \frac{1}{2}\rho_2 \left|\vec{v}\right|_2^2) \left|\vec{v}\right|_2 , \tag{1.6}$$

where $\tilde{u}$ = internal energy per unit mass,

$P\left|\vec{v}\right|$ = rate of work done per unit area by the gas pressure, and

$(\rho\tilde{u} + \frac{1}{2}\rho\left|\vec{v}\right|^2)\left|\vec{v}\right|$ = rate of transport of internal and kinetic energy per unit area.

Treating the gas as an ideal gas, the Rankine Hugoniot conditions can be derived for the pressure, density, and temperature jumps using these laws of

conservation as follows:

From Equation (1.4), we get:

$$\rho_2 v_2^2 = \frac{\phi_m^2}{\rho_2} \Rightarrow v_2^2 = \frac{\phi_m^2}{\rho_2^2} \tag{1.7}$$

and

$$\rho_1 v_1^2 = \frac{\phi_m^2}{\rho_1^2} \Rightarrow v_1^2 = \frac{\phi_m^2}{\rho_1^2}. \tag{1.8}$$

Rewriting Equation (1.5), we get:

$$P_2 - P_1 = \rho_1 v_1^2 - \rho_2 v_2^2 \tag{1.9}$$

and

$$P_2 - P_1 = \frac{\phi_m^2}{\rho_1} - \frac{\phi_m^2}{\rho_2} = \phi_m^2 \left(\frac{1}{\rho_1} - \frac{1}{\rho_2} \right). \tag{1.10}$$

Using this, we have:

$$v_1^2 - v_2^2 = \phi_m^2 \left(\frac{1}{\rho_1^2} - \frac{1}{\rho_2^2} \right) = \phi_m^2 \left(\frac{1}{\rho_1} - \frac{1}{\rho_2} \right) \left(\frac{1}{\rho_1} + \frac{1}{\rho_2} \right) \tag{1.11}$$

or,

$$v_1^2 - v_2^2 = (P_2 - P_1) \left(\frac{1}{\rho_1} + \frac{1}{\rho_2} \right). \tag{1.12}$$

To find the density jump, we need to solve the laws of conservation simultaneously. Considering the gas as an ideal gas, the internal energy per unit mass is given by:

$$\tilde{u} = \frac{P}{(\gamma-1)\rho} \Rightarrow P = (\gamma-1)\rho\tilde{u}. \tag{1.13}$$

Using Equation (1.13) in Equation (1.6), we get:

$$(\gamma-1)\rho_2\tilde{u_2}v_2 + \rho_2\tilde{u_2}v_2 + \frac{1}{2}\rho_2 v_2^3 = (\gamma-1)\rho_1\tilde{u_1}v_1 + \rho_1\tilde{u_1}v_1 + \frac{1}{2}\rho_1 v_1^3. \tag{1.14}$$

Simplifying the above equation, we get:

$$\gamma\rho_2\tilde{u_2}v_2 + \frac{1}{2}v_2^2(\rho_2 v_2) = \gamma\rho_1\tilde{u_1}v_1 + \frac{1}{2}v_1^2(\rho_1 v_1). \tag{1.15}$$

Using Equation (1.4) and dividing the above equation by ϕ_m:

$$\gamma\tilde{u_2} + \frac{1}{2}v_2^2 = \gamma\tilde{u_1} + \frac{1}{2}v_1^2. \tag{1.16}$$

From Equation (1.13), we have,

$$\gamma\frac{P_2}{(\gamma-1)\rho_2} + \frac{1}{2}v_2^2 = \gamma\frac{P_1}{(\gamma-1)\rho_1} + \frac{1}{2}v_1^2. \tag{1.17}$$

Therefore,

$$v_1^2 - v_2^2 = \frac{2\gamma}{\gamma-1}\left[P_2\rho_2^{-1} - P_1\rho_1^{-1}\right]. \tag{1.18}$$

Using Equation (1.12), we get:

$$(P_2 - P_1)(\left(\frac{1}{\rho_1} + \frac{1}{\rho_2}\right) = \frac{2\gamma}{\gamma-1}\left[P_2\rho_2^{-1} - P_1\rho_1^{-1}\right]. \tag{1.19}$$

Simplifying this equation, we get:

$$\gamma P_2\rho_2^{-1}+\gamma P_2\rho_1^{-1}-\gamma P_1\rho_2^{-1}-\gamma P_1\rho_1^{-1}-P_2\rho_2^{-1}-P_2\rho_1^{-1}+P_1\rho_2^{-1}+P_1\rho_1^{-1} = -2\gamma P_1\rho_1^{-1}+2\gamma P_2\rho_2^{-1}. \tag{1.20}$$

Further simplification gives:

$$\rho_2^{-1}[-P_2(\gamma+1)-P_1(\gamma-1)] = -\rho_1^{-1}[P_2(\gamma-1)+P_1(\gamma+1)], \tag{1.21}$$

which in turn gives:

$$\frac{\rho_2^{-1}}{\rho_1^{-1}} = \frac{P_2(\gamma-1)+P_1(\gamma+1)}{P_2(\gamma+1)+P_1(\gamma-1)}. \tag{1.22}$$

From Equation (1.10), we know that:

$$\phi_m^2 = \frac{P_2-P_1}{\rho_1^{-1}-\rho_2^{-1}} = \frac{(P_2-P_1)}{\rho_1^{-1}(1-\frac{\rho_2^{-1}}{\rho_1^{-1}})}, \tag{1.23}$$

$$\phi_m^2 = \frac{\rho_1(P_2-P_1)}{1-\frac{P_2(\gamma-1)+P_1(\gamma+1)}{P_2(\gamma+1)+P_1(\gamma-1)}} \tag{1.24}$$

and

$$\phi_m^2 = \frac{1}{2}\rho_1\left[P_2(\gamma+1)+P_1(\gamma-1)\right]. \tag{1.25}$$

Substituting using Equation (1.4),

$$v_1^2 = \frac{1}{2\rho_1}\left[P_2(\gamma+1)+P_1(\gamma-1)\right]. \tag{1.26}$$

The Mach number of this shock is given by $M_1 = v_1/v_{s1}$, where $v_{s1} = \sqrt{\gamma p_1/\rho_1}$, so that

$$M_1^2 = \frac{v_1^2 \rho_1}{\gamma P_1}. \tag{1.27}$$

Substituting into Equation (1.26),

$$\rho_1 v_1^2 = M_1^2 \gamma P_1 = \frac{1}{2}\left[P_2(\gamma+1) + P_1(\gamma-1)\right] \tag{1.28}$$

and

$$P_1\left[2M_1^2\gamma - (\gamma-1)\right] = P_2(\gamma+1). \tag{1.29}$$

which gives the pressure jump,

$$\frac{P_2}{P_1} = \frac{2M_1^2\gamma - (\gamma-1)}{\gamma+1}. \tag{1.30}$$

Using Equation (1.22), we have:

$$\frac{\rho_2}{\rho_1} = \frac{P_2(\gamma+1) + P_1(\gamma-1)}{P_2(\gamma-1) + P_1(\gamma+1)}. \tag{1.31}$$

Dividing numerator and denominator on r.h.s. by P_1 and substituting Equation (1.30)

$$\frac{\rho_2}{\rho_1} = \frac{[2M_1^2\gamma - (\gamma-1)] + (\gamma-1)}{[2M_1^2\gamma - (\gamma-1)] + (\gamma+1)} = \frac{2M_1^2\gamma(\gamma+1)}{aM_1^2\gamma(\gamma-1) + 2(2\gamma)}, \tag{1.32}$$

which gives the equation for the density jump:

$$\frac{\rho_2}{\rho_1} = \frac{(\gamma+1)M_1^2}{2+(\gamma-1)M_1^2}. \tag{1.33}$$

Therefore, the Equation for the pressure jump is:

$$\frac{P_2}{P_1} = \frac{2\gamma M_1^2 - (\gamma-1)}{\gamma+1} \tag{1.34}$$

and the Equation for the density jump is:

$$\frac{\rho_2}{\rho_1} = \frac{|\vec{v}|_1}{|\vec{v}|_2} = \frac{(\gamma+1)M_1^2}{2+(\gamma-1)M_1^2}. \tag{1.35}$$

And the Equation for the temperature jump is:

$$\frac{T_2}{T_1} = \frac{\frac{P_2}{\rho_2}}{\frac{P_1}{\rho_1}} = \frac{[2\gamma M_1^2 - (\gamma-1)][2+(\gamma-1)M_1^2]}{(\gamma+1)^2 M_1^2}, \tag{1.36}$$

where M_1 = Mach number of the shock

and $\gamma = 5/3$ for a non-relativistic monoatomic gas.

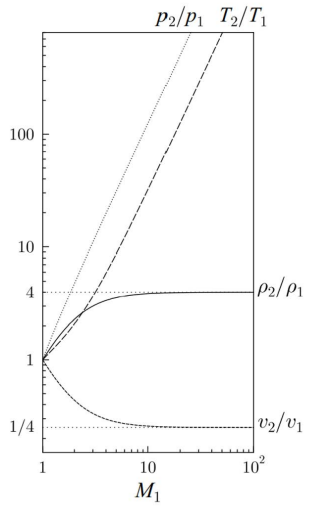

Figure 1.7: The figure shows the plots for the pressure, temperature, and density jumps according to the Rankine-Hugoniot jump conditions for a non-relativistic monoatomic gas, as a function of M_1. In the limit $M \to \infty$, the maximum value for the density jump (ρ_2/ρ_1) is 4. However, the pressure jump increases without any limit. As a result, the temperature jump may also increase without limit. (Blundell and Blundell, 2010)

Figure 1.7 shows the plots for the pressure, temperature, and density jumps according to the Rankine-Hugoniot jump conditions for a non-relativistic monoatomic gas as a function of M_1. In the limit $M \to \infty$, the maximum value for the density jump (ρ_2/ρ_1) is 4. However, the pressure jump increases without any limit. As a result, the temperature jump may also increase without limit (Blundell and Blundell, 2010).

1.4.1 Shocks in Galaxy Clusters

Shocks in the ICM may occur due to any of the following phenomena:

1. Due to very strong AGNs in the central regions of clusters blowing bubbles into the ICM, weak shocks ($M \sim 1$) are created within a few hundred kpc radius of the center (Jones, 2002; McNamara et al., 2005; Nulsen et al., 2005; Forman et al., 2007).

2. Simulations show that at the cluster outskirts, cold intergalactic medium (IGM) accretes to the cluster potential, causing very strong shocks with $M \sim 10 - 100$ (Miniati et al., 2000). However, as this is happening at several megaparsecs from the cluster center, the X-ray surface brightness, and by extension, the gas density, is too low for any of the current X-ray missions.

3. During a merger event between two clusters of galaxies, the dark matter halos pass through each other without any interactions. The gas in the ICM of these two clusters interact, and the infalling gas moves at a supersonic speed. This leads to the formation of a shock front. Figure 1.8 shows the X-ray image of 1E0657 (or Bullet Cluster), which is an example of such a merger shock (Markevitch, 2006a).

Shock fronts formed as a result of major mergers travel through the cluster, thereby etching on the ICM the story of the large-scale structure formation. Merger shocks typically have $M \leq 3$. Table 1.1 lists the galaxy clusters wherein mergers resulted in strong shocks. Evidently, there are very few systems like this, which is why they make for very interesting research.

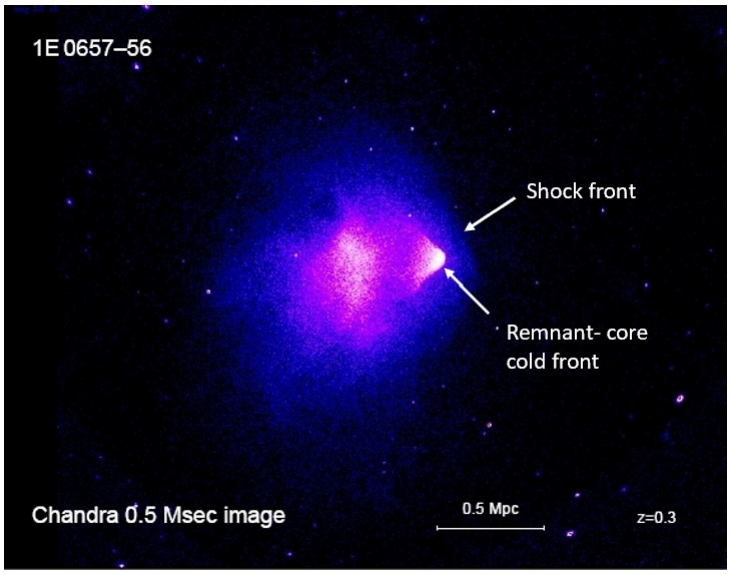

Figure 1.8: An X-ray image of the Bullet Cluster (Markevitch, 2010) at redshift $z = 0.3$, as observed by the *Chandra* X-ray Observatory. The "bullet" refers to the smaller sub-clusters moving westward after passing through a bigger cluster in the merger. This merger creates a strong shock ($M = 3.0 \pm 0.4$) in front of the cold bullet, as indicated in the image.

Table 1.1: A list of galaxy cluster merger systems that exhibit strong shocks. There are very few systems that indicate such strong mergers, making them interesting case studies.

Galaxy Cluster	R.A.	Dec.	z	Mach Number	Reference
Bullet Cluster	06:58:31.1	+55:56:49	0.296	3.0 ± 0.4	Markevitch (2006a)
A2146	15:56:08.9	+66:21:21	0.234	2.3 ± 0.2	Russell et al. (2012)
A665	08:30:45.2	+65:52:55	0.182	3.0 ± 0.6	Dasadia et al. (2016)
A520	04:54:19.0	+02:56:49	0.203	$2.4^{+0.4}_{-0.3}$	Wang et al. (2018)

1.4.2 Mach Number

The Mach number for a shock can be determined from the X-ray surface brightness profile across the shock front by fitting it to a gas density model. The method for obtaining the surface brightness profile has been detailed in Section 3. Figure 1.9 shows the radial profile of the X-ray brightness across the shock front of the Bullet Cluster. The discontinuity in the density is determined by fitting this profile with a density jump model with an abrupt spherical density jump (Markevitch and Vikhlinin, 2007). The best-fit model gives the density jump as a factor of 3. Rearranging the Rankine Hugoniot condition obtained in Equation (1.35), we get the following equation (Russell et al., 2010):

$$M = \left[\frac{2\frac{\rho_2}{\rho_1}}{\gamma + 1 - (\frac{\rho_2}{\rho_1})(\gamma - 1)} \right]^{\frac{1}{2}}. \tag{1.37}$$

Using this equation, the Mach number obtained for the Bullet Cluster is 3.0 ± 0.4.

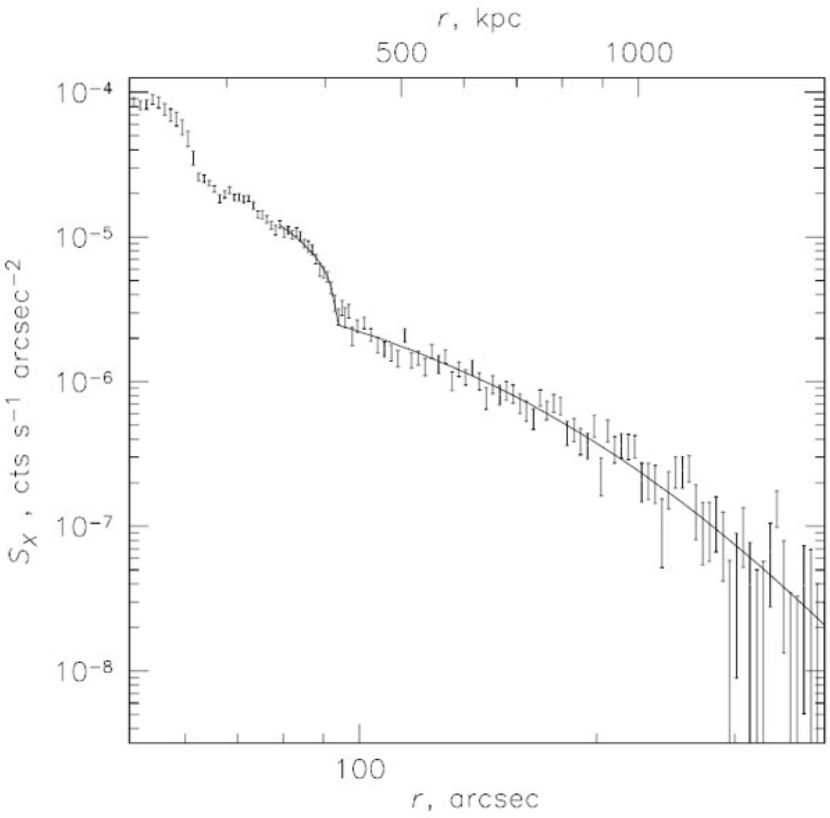

Figure 1.9: The X-ray surface brightness profile of the bullet cluster fitted with a density jump model. (Markevitch and Vikhlinin, 2007)

Mach number can also be determined by using the temperature jump across the shock front. The method for obtaining this profile is also discussed in detail in Section 3. Equation 1.36 can be rearranged to obtain the equation for Mach number:

$$M = \left[\frac{(\gamma+1)^2((\frac{T_2}{T_1})-1)}{2\gamma(\gamma-1)} \right]^{\frac{1}{2}}. \tag{1.38}$$

The left panel in Figure 1.10 shows the temperature profile for the projected temperature values of the Bullet Cluster. The temperature jump obtained from this value agrees with the Mach number obtained from the density jump. The pre-shock temperature can be used to obtain the sound speed in the gas. Once the Mach number has been determined, the shock velocity can also be calculated.

1.4.3 Electron-ion Equilibration

Cluster merger shock fronts provide the opportunity to investigate the electron-ion equilibration time in the magnetized ICM. The post-shock temperature of the ICM is the temperature at which the electrons and ions equilibrate after a specific time. The timescale for this equilibration depends on how the electrons are heated. When the shock front propagates through a collisional plasma, the ions are dissipatively heated by the shock. The electrons, however, are not strongly heated by the shock. They are expected to undergo adiabatic compression, given by the following equation:

$$T_{e,2} = T_{e,1}(\frac{n_2}{n_1})^{\gamma-1}, \tag{1.39}$$

where T_{e1}, T_{e2} = pre-shock and post-shock electron temperatures

and n_1, n_2 = pre-shock and post-shock electron densities,

and $\gamma = 5/3$ for a non-relativistic monoatomic gas.

The electron temperature then equilibrates with that of the ions via Coulomb collisions. These collisions occur on a Spitzer timescale given by:

$$\tau_{eq}(e,p) = 6.2 \times 10^8 yr (\frac{n_e}{10^{-3}})^{-1} * (\frac{T_e}{10^8 K})^{3/2}, \tag{1.40}$$

where T_e is the electron temperature, and n_e is the electron density (Sarazin, 1986).

However, shocks in a magnetized plasma like the ICM are likely to be collisionless. Observations of solar wind shocks found that the width of the shock front over which the temperature jump (of the electrons and ions) occurs is several orders of magnitude lesser than the mean free path of Coulomb collision because of the interactions produced by the coupling of the particles with the electric and magnetic fields (see Ness et al. 1964, Hull et al. 2001). Hence, the time over which the electrons get heated would be expected to be much shorter than the Coulomb collisional timescale.

The Bullet cluster provided the first-ever experimental setup to measure the electron-ion equilibration timescale. While the temperature of the protons (T_i) cannot be measured in X-rays, it is possible to measure T_e, and the gas density jump across the shock front. The gas density jump can be used, along with the pre-shock electron temperatures, to predict the post-shock adiabatic and instant-equilibration temperatures, using the adiabatic and the Rankine-Hugoniot jump conditions, respectively. The Mach number of the Bullet cluster is sufficiently

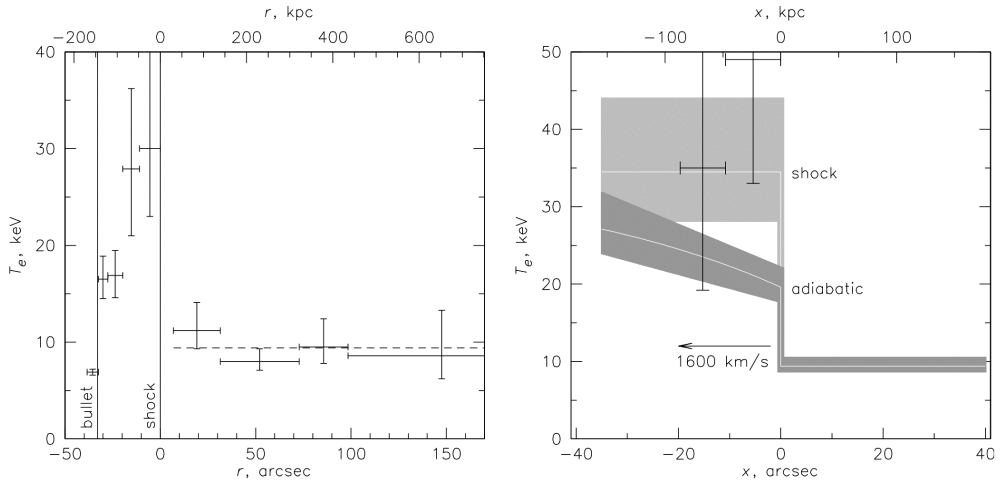

Figure 1.10: Left: Projected temperature profile across the shock region. Right: Deprojected temperature values overlaid on the two possible models of shock-heating: instant equilibration (represented by a light gray band, labeled "shock") and adiabatic compression with subsequent equilibration over the Spitzer timescale (represented by the dark-gray band, labeled "adiabatic"). The velocity is the post-shock velocity, assumed to be constant in the immediate vicinity of the shock.(Markevitch and Vikhlinin, 2007)

high so that the adiabatic and instant-heating electron temperatures are different enough to distinguish between them and determine the equilibration model.

In Figure 1.10, the left panel shows the projected temperature profile of the Bullet Cluster across the shock. The shock front is at 0". The region to the right shows the pre-shock temperatures. As can be seen in the first two bins to the left of the shock front, there is a clear jump in the electron temperature. The temperature goes down again in the region close to the bullet; however, this likely corresponds to a second surface brightness edge in the cluster (see fig 1.9) and is, in all probabilities, caused by residual cool gas from the sub-clusters, and is not related to the primary shock.

The right panel in Figure 1.10 shows the deprojected temperature values overlaid on the two possible models of shock-heating: instant equilibration (represented by a light gray band in the figure) and adiabatic compression with subsequent equilibration over the Spitzer timescale (represented by dark-gray band in the figure). The plot assumes a constant post-shock velocity in the immediate shock vicinity.

Looking at the plot, it is clear that the temperatures are consistent with the instant-heating model. However, the deprojected temperatures are so high ($\sim 30 - 50keV$) that they cannot be constrained by *Chandra* because its pass band lies in the range of $0.7 - 7.0keV$ as shown in Figure 2.5, and so, only their lower limits are meaningful. Thus, the adiabatic heating model is excluded at a 95% confidence level (Markevitch, 2003).

These measurements for the electron-ion equilibration have also been performed for the stronger ($M = 2.3 \pm 0.2$) shock in A2146, which showed a preference for the Coulomb equilibration at a 95% confidence level (Russell et al., 2012). Thus, a definite method for electron-ion equilibration has not yet been determined. A merger system that provides the answer to this important question with greater certainty will provide remarkable insight into the physics of the ICM.

1.5 Cold Fronts

Cold Fronts are sharp contact discontinuities in the density and temperature of the ICM (for a review, see Markevitch and Vikhlinin 2007). Unlike shock fronts, the brighter and denser side of this discontinuity is the colder one, and there is no change in the pressure across the cold fronts. The discovery of cold fronts gave us a new way to determine the transport properties of the ICM. Cold fronts have been observed in merging galaxy clusters mainly due to the exceptional angular resolution of *Chandra*. One of the first cold fronts discovered by *Chandra* was in the merging cluster A2142, shown in Figure 1.11 (Markevitch et al., 2000a).

Clusters of galaxies are dynamic objects owing to the ongoing cosmological structure formation. The motion of gas within the cluster provides the condition for the formation of cold fronts. There are two classes of cold fronts - "remnant-core" cold fronts and "sloshing" cold fronts (Tittley and Henriksen, 2005a).

Remnant cold fronts form when a smaller galaxy group or sub-cluster falls into a larger cluster, and the infalling cluster undergoes "Ram-pressure stripping." Ram-pressure stripping happens when the infalling cluster is stripped of the outer layer of its atmosphere because of the heat wind generated as a result of moving through the ICM of the larger cluster. Prominent examples of such cold fronts are the Bullet Cluster (Markevitch, 2003) (see Figure 1.8) and A3667 (Vikhlinin et al., 2001a).

"Sloshing" cold fronts form when the merger between two sub-clusters is off-axis, thereby causing an offset of the dense core gas from its equilibrium position in the cluster potential. The ICM then sloshes around in the potential well, much like wine sloshes around in a wine glass, as shown in fig 1.12 (Markevitch et al., 2000a; Tittley and Henriksen, 2005a). Sloshing cold fronts are mostly seen in cool-core clusters, which are clusters that have not seen any merger activity for some time. Prominent examples of merger systems with sloshing cold fronts are the Virgo Cluster (Forman et al., 2010; Werner et al., 2016) and A2142 (Markevitch et al., 2000a). As shown in 1.11, two fronts in A2142 were identified on the opposite sides of the cluster core and were originally proposed to be remnant-core cold fronts. However, longer *Chandra* observations indicate that they are indeed sloshing cold fronts (Markevitch and Vikhlinin, 2007).

As shown in 1.11, two fronts in A2142 were identified on the opposite sides of the cluster core and were originally proposed to be remnant-core cold fronts. However, longer *Chandra* observations indicate that they are indeed sloshing cold fronts (Markevitch and Vikhlinin, 2007). Figure 1.13 shows the temperature

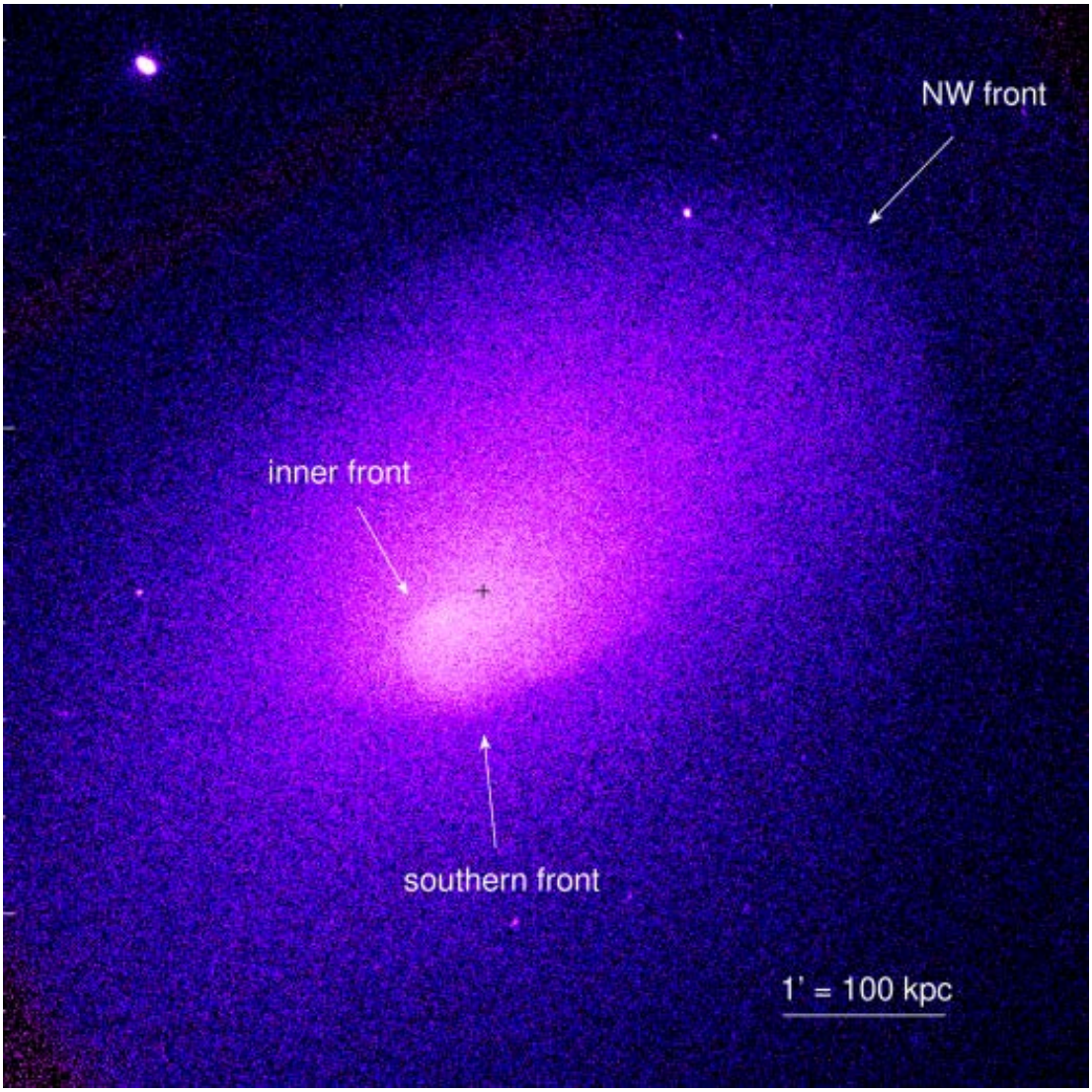

Figure 1.11: ACIS image of A2142, the galaxy cluster where the first cold fronts were discovered. At least two brightness edges are seen: one between the blue and the black region to the Northwest of the center (NW Front) and one between the purple and blue regions to the south of the center (Southern Front) (Markevitch and Vikhlinin, 2007).

Figure 1.12: Sloshing cold fronts form when there is an off-axis merger between two sub-clusters. Such a merger causes the ICM to slosh around its equilibrium position, much like wine sloshes around in a wine glass.(Markevitch and Vikhlinin, 2007)

profiles, X-ray brightness profiles, density profiles, and pressure profiles across the two sharp edges in the *Chandra* image of A2142. Panel (b) shows the temperature profiles across both the edges, with the southern edge on the left and the NW edge on the right. With an observed density jump of $r \sim 2$ and post-shock temperature of $T_1 \sim 7.5keV$ inside the NW edge, the pre-shock gas temperature is expected to be $T_0 \simeq 4keV$. However, the observed temperature in the less dense region of the gas is, in fact, higher than in the more dense region. This indicates that the brightness edge is not a shock but a cold front. A similar effect is observed in the southern edge as well.

1.5.1 Kelvin-Helmholtz Instabilities (KHI) and Magnetic Draping

All the formation scenarios for cold fronts predict the existence of velocity shear (Zuhone and Roediger, 2016). Such interfaces with shear velocities often develop Kelvin-Helmholtz instabilities (Chandrasekhar, 1961). Hence, one of the questions that often need to be answered when studying cold fronts is whether or not they are stable to KHIs because these instabilities eventually lead to the dissolution of the sharp interface.

KHI's may be suppressed in the presence of a strong magnetic field aligned with the shear flow interface (Vikhlinin et al., 2001c). The strength of the magnetic field is described by equation 1.5.1

$$\beta = \frac{p_{th}}{p_{mag}},$$

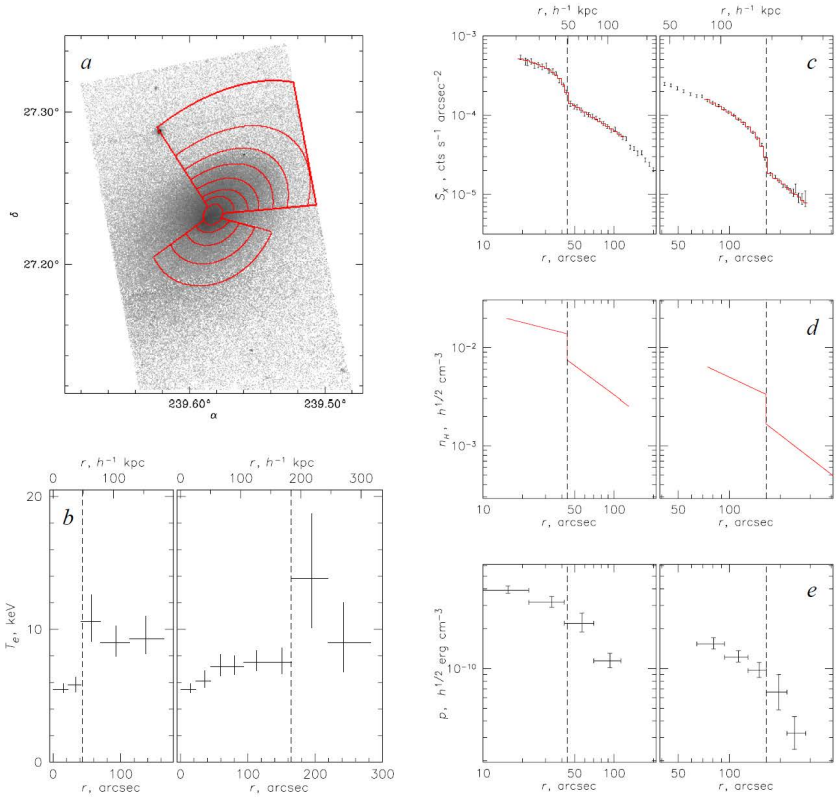

Figure 1.13: (a) Exposure-corrected X-ray image of A2142 with red sectors indicating the regions over which the temperature profiles are extracted. The first region is to the south of the center (Southern edge), and the second region is to the northwest (NW edge) of the center. In panels (b)-(e), the plots to the left refer to the Southern edge, and the ones to the right refer to the NW edge. (b) shows the temperature profiles across the two regions. (c) shows the X-ray brightness profiles across these two edges. The red histogram here is the brightness model corresponding to the best-fit gas density model in (d). (e) shows the pressure profiles obtained using temperature and density profiles. (Markevitch et al., 2000a)

where p_{th} is the thermal pressure and p_m is the magnetic pressure. A high value of β indicates that the thermal pressure dominates over the magnetic pressure, while a low value of β suggests that the magnetic pressure is significant compared to the thermal pressure.

The effect of the magnetic field on KHI and the dissolution of structure can be seen in Figure 1.14. Panels (a)-(c) show the snapshots of the cold front at 2.65 Gyr, 3.0 Gyr, and 3.5 Gyr, respectively. The cold front is unmagnetized, and hence, the KHIs are not suppressed at all. As can be seen from the figure, this results in the breakdown of the sharp interface. Panels (d)-(f) represent the evolution of the cold front for $\beta = 1000$ at 2.65 Gyr, 3.0 Gyr, and 3.5 Gyr, respectively. The magnetic field in this case is slightly higher compared to that in panels (a)-(c), and as a result, the sharp interface does not dissolve as much as it does in the complete absence of magnetic field lines. Further, in panels (g)-(i), $\beta = 200$, the magnetic field is even higher, and the sharp interface maintains its structure far better than in the previous cases.

The magnetic field strength, parameterized by β, is negligible in most of the volume of the galaxy cluster (Zuhone and Roediger, 2016). However, the suppression of instabilities at the interface of the cold front indicates the presence of "magenetic draping", or the stretching of magnetic field lines over the cold front as shown in fig 1.15

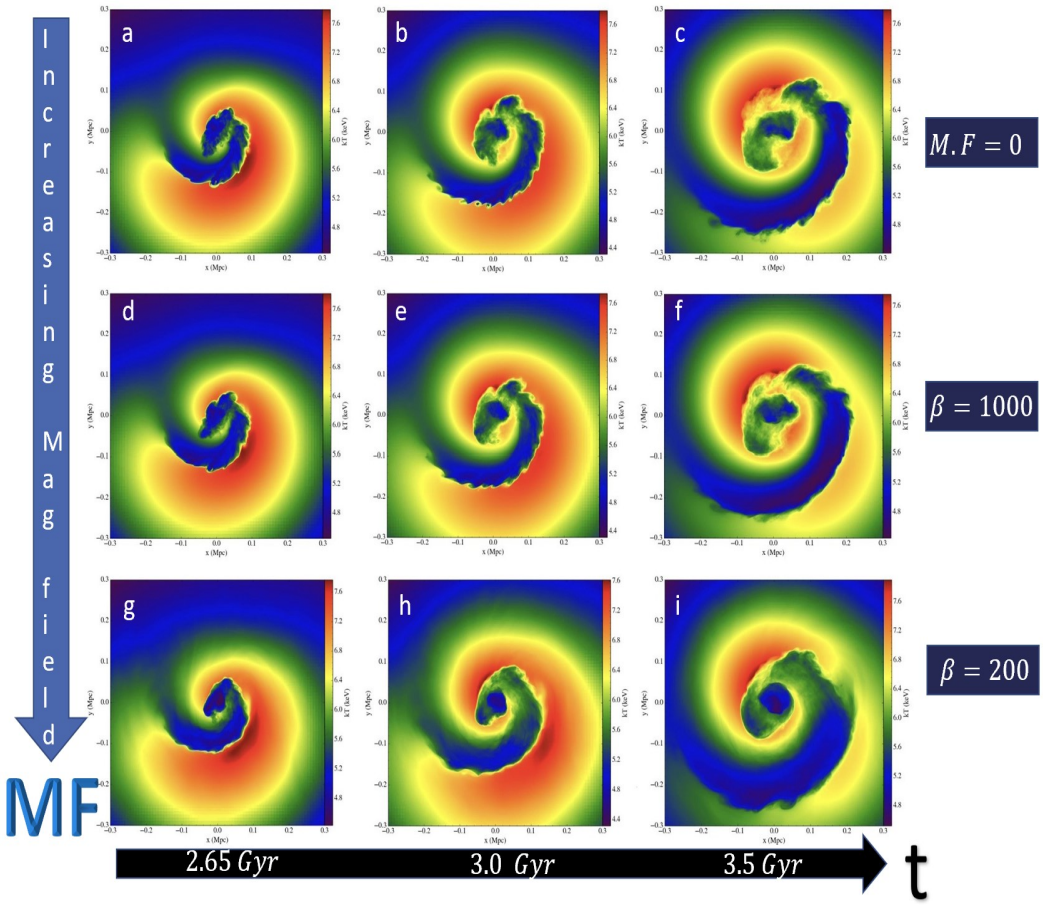

Figure 1.14: Figures (a)-(f) represent the effect of Magnetic fields on the stability of the cold front. Panels (a)-(c) show the evolution of an unmagnetized cold front at 2.65 Gyr, 3 Gyr, and 3.5 Gyr, respectively. Panels (d)-(f) show the cold front at the same time when $\beta = 1000$. Panels (g)-(i) show the evolution of the cold front when $\beta = 200$ at 2.65 Gyr, 3.0 Gyr, and 3.5 Gyr, respectively. This work made use of data from the Galaxy Cluster Merger Catalog.

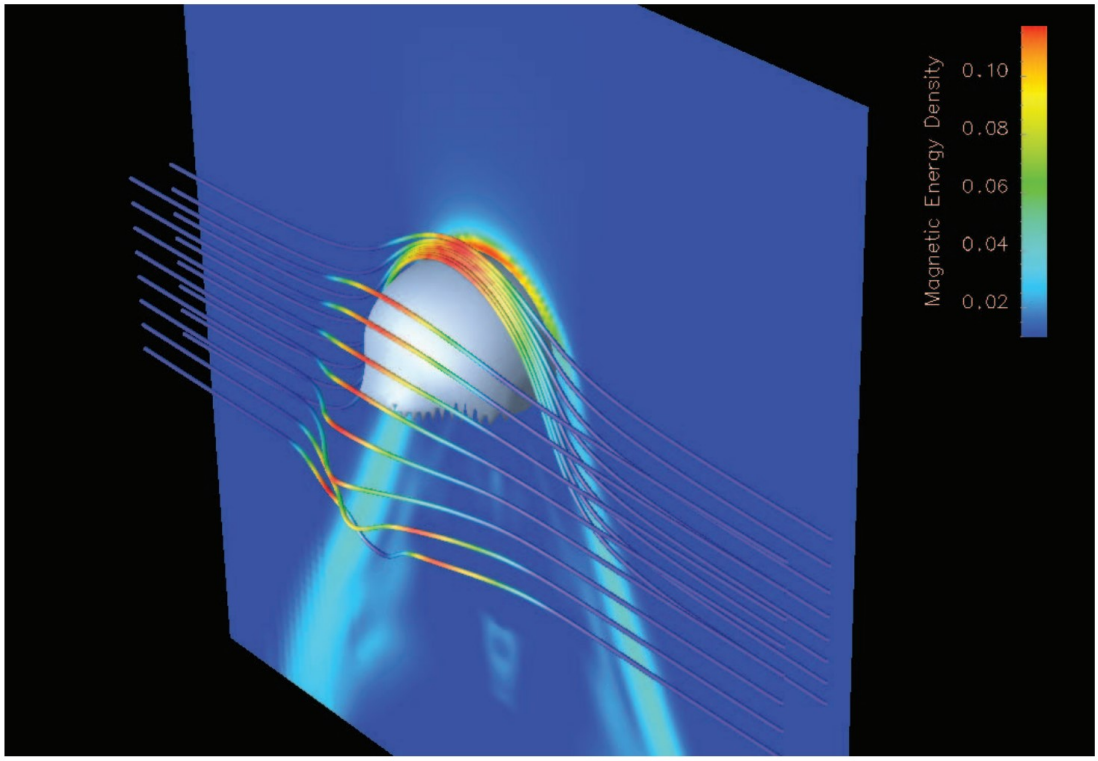

Figure 1.15: A three-dimensional simulation of an overdense projectile, in this case, a cold front, passing through a uniformly magnetized ICM, with the magnetic field lines draped around it (Dursi and Pfrommer, 2008). The cutting plane and the field lines are colored according to the magnetic energy.

1.5.2 Diffusion and Thermal Conduction

For a lot of the cold fronts, the width of the interface is unresolved even by *Chandra* because often, this width is smaller than the Coulomb mean free path. The diffusion of particles and thermal conduction across the cold front interface is expected to be very efficient. The values of temperature and densities of the gas on either side of the front imply a quick thermal conduction timescale, which in turn would blur out jumps in temperature and density. However, observations for many clusters show sharp interfaces, indicating that both diffusion and thermal conduction are strongly suppressed (Zuhone and Roediger, 2016).

Chapter 2. Observatories

2.1 *Chandra* X-ray Observatory

The *Chandra* X-ray Observatory (Figure 2.1) is an X-ray imaging space telescope launched by NASA on July 23, 1999, on board the space shuttle Columbia. Figure 2.1 shows an artist's conception of *Chandra* in space. *Chandra* is jointly managed by NASA's Marshall Space Flight Center (MSFC), Chandra X-ray Center (CXC), and Smithsonian Astrophysical Observatory (SAO). The Chandra X-ray Observatory is part of NASA's Great Observatories program, which includes the Hubble Space Telescope and the Spitzer Space Telescope. These observatories are placed in different orbits to cover a wide range of wavelengths and provide complementary observations of the universe.

Chandra has been designed to detect and obtain the X-ray images and spectra of highly energetic events such as the merger of galaxy clusters, matter around black holes, and many others that can help understand the structure and evolution of the universe. *Chandra* orbits at an altitude of about 133,000km (82,646 mi) above the Earth, with an orbital period of 64 hours and a continuous observation time of 55 hours.

The angular resolution of *Chandra* is 0.5 arcseconds on axis, which is better than any other previous or current X-ray observatories. This high angular

Figure 2.1: An artist's impression of *Chandra* X-ray Observatory in space. Image credits: NASA/CXC

resolution is due to Chandra's use of four nested mirrors that focus X-rays onto the detector. This has resulted in sharper and more detailed images of the high-energy universe from *Chandra* compared to any other telescope.

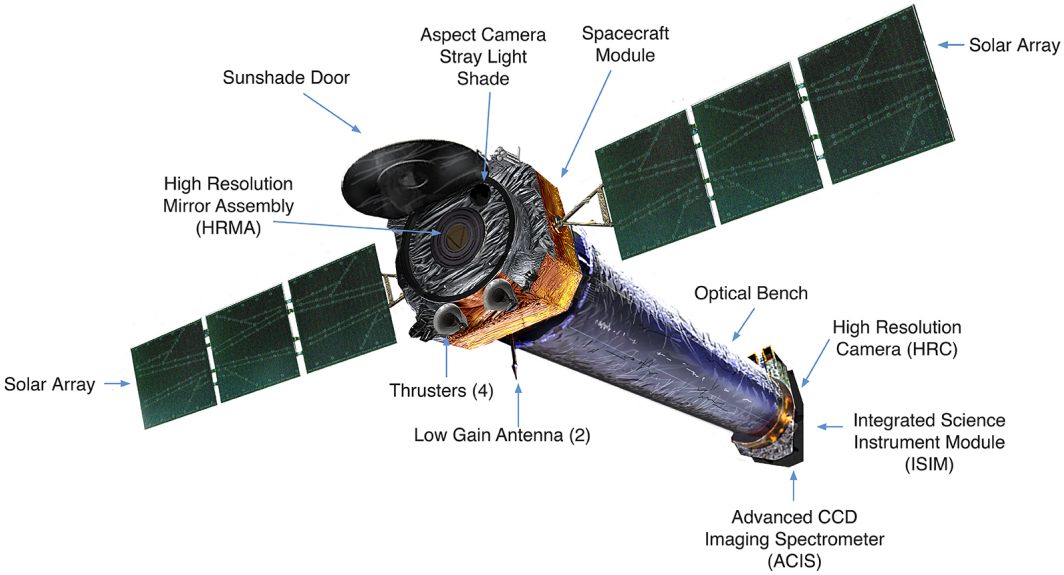

Figure 2.2: A labelled diagram of the *Chandra* X-ray observatory. There are four science instruments aboard the spacecraft, in addition to the mirror assembly, the solar panels, and the spacecraft and science modules. Image credits: *Chandra* X-ray Center (CXC).

As shown in Figure 2.2, there are four major Science instruments on board the *Chandra* observatory:

1. Advanced CCD Imaging Spectrometer (ACIS)

2. High Resolution Camera (HRC)

3. High Energy Transmission Grating Spectrometer (HETGS)

4. Low Energy Transmission Grating Spectrometer (LETGS)

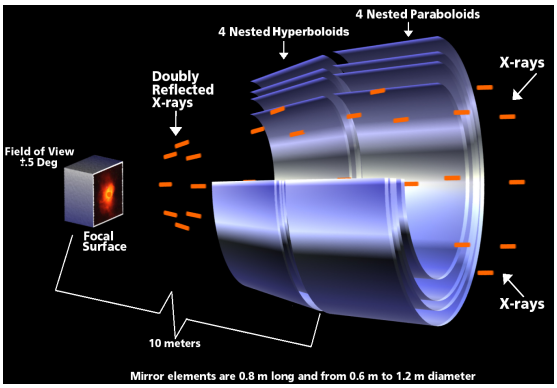

Figure 2.3: Nesting of mirrors on the *Chandra* observatory. Image credits: NASA

The Chandra X-ray Observatory's nested mirror system, shown in Figure 2.3, is designed to capture and focus X-rays with high precision. The fundamental principle behind the Chandra telescope's nested mirror system is grazing incidence optics. Unlike traditional optical telescopes that use reflection at normal incidence (a 90-degree angle), Chandra's mirrors are designed to work at extremely shallow angles, typically less than a degree. This grazing incidence allows the mirrors to reflect X-rays effectively. The mirrors in Chandra are arranged in a series of concentric shells. There are four sets of these nested mirrors, each consisting of several individual mirror segments. These mirror shells are designed to funnel and focus incoming X-rays toward a common focal point. The mirror surfaces are polished to an extreme level of smoothness to minimize the scattering of X-rays. As the X-rays undergo multiple reflections off the nested mirrors, they converge at a common focal point. This focal point is where the X-rays are concentrated and ultimately detected by the telescope's detectors. Because of the grazing

incidence optics and nested mirror design, Chandra can achieve exceptionally high-resolution X-ray images of astronomical objects. This capability is crucial for studying fine details and structures within X-ray-emitting sources in space.

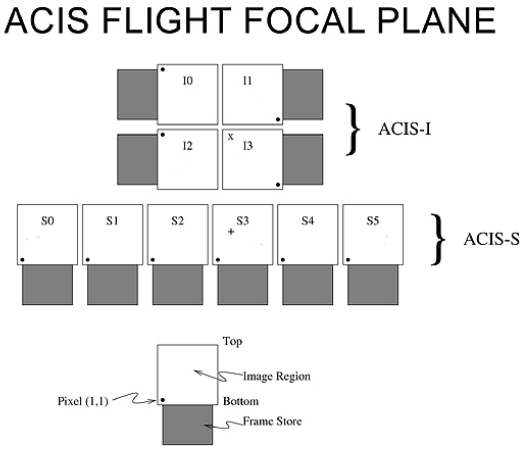

Figure 2.4: ACIS schematic layout overhead view to illustrate the location of the imaging (ACIS-I) and spectroscopic (ACIS-S) arrays of CCD ships. Image credits: NASA

The ACIS is a focal plane instrument (Figure 2.4) that consists of 10 Charged-Coupled Devices (CCDs) arranged in two arrays, ACIS-I and ACIS-S. The ACIS-I array is a 2x2 arrangement of chips, and ACIS-S is a strip of 6 chips. The spatial resolution of *Chandra* is 0.5 arcsec on-axis over the energy range of 0.2 to 10.0 keV. This instrument is used for its capability to measure the energy of incoming photos while simultaneously producing an X-ray image using these photons. The field of view of ACIS-I is $16' \times 16'$, and that for all 6 chips of the ACIS-S is $8' \times 48'$.

Figure 2.5 shows the effective area of *Chandra*. The effective area is measured in units of cm^2. *Chandra's* pass band lies between the energies of

$0.7 - 7.0keV$. This means that it is not possible to obtain information for energies that lie beyond this range.

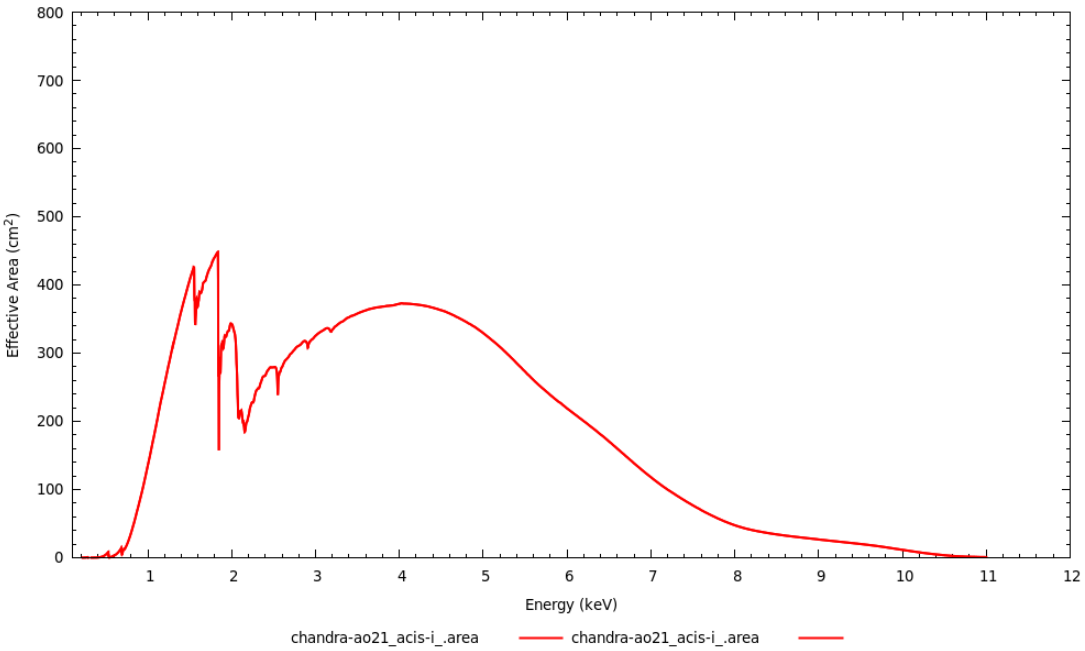

Figure 2.5: Effective area of *Chandra* in its 21st cycle.

The Chandra X-ray Observatory provides specific software tools to download and analyze Chandra data. The primary software package for this purpose is the Chandra Interactive Analysis of Observations (CIAO). CIAO is designed to handle data reduction and processing of Chandra X-ray data. It also provides tools for spectral analysis, imaging of the X-ray data, source detection, and data visualization. Other software tools like XSPEC and SAOImage DS9 are also commonly used in conjunction with CIAO for more specialized tasks.

2.2 *NuSTAR*

The NuSTAR telescope (Figure 2.6), short for Nuclear Spectroscopic Telescope Array, is a space-based X-ray telescope designed to observe high-energy X-rays from astrophysical sources. It is a mission managed by NASA's Jet Propulsion Laboratory (JPL) in collaboration with the California Institute of Technology (Caltech). NuSTAR was designed to study the high-energy universe by focusing on the hard X-ray band (3 to 79 keV). This energy range allows NuSTAR to observe the most energetic phenomena in the universe, such as black holes, supernovae, neutron stars, and active galactic nuclei.

NuSTAR is equipped with two main scientific instruments:

1. Focal Plane Module (FPMA and FPMB)

2. Optics Module

The FPM is NuSTAR's primary instrument for collecting X-ray data. It consists of two co-aligned detectors, FPMA and FPMB. The FPMs can record X-rays in the energy range of approximately 3 to 79 keV (kilo-electron volts).

2.3 *XMM-Newton*

The *XMM Newton* X-ray Observatory is an X-ray space telescope operated by the European Space Agency (ESA). It was launched on December 10, 1999, and has since been an essential instrument for observing and studying X-ray emissions from celestial objects. Figure 2.7 shows an artist;s illustration of the *XMM Newton*

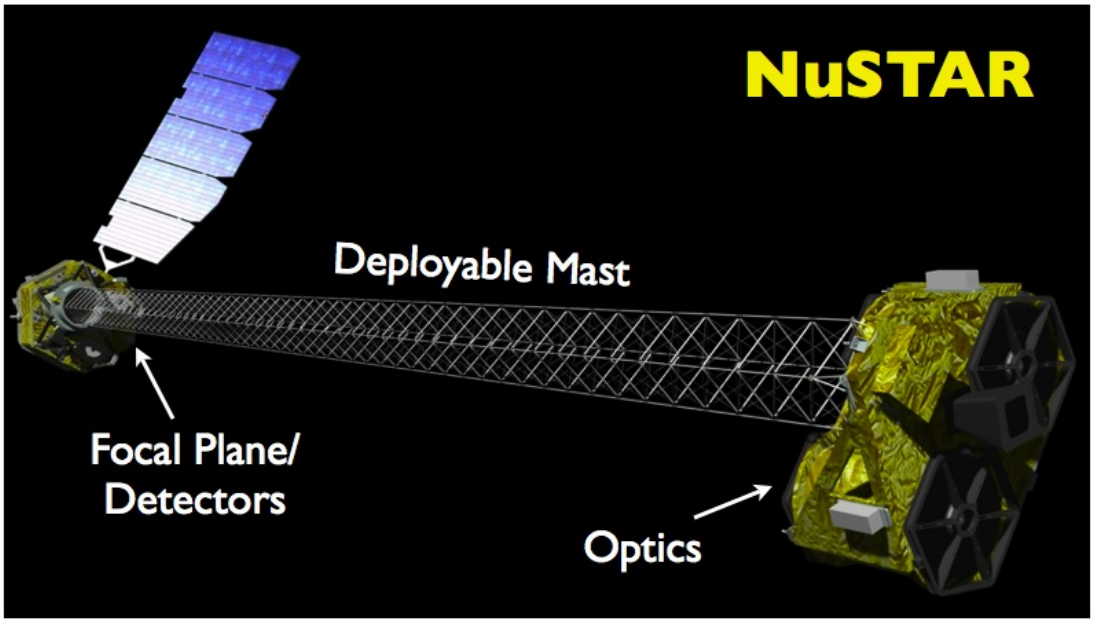

Figure 2.6: An artist's impression of NuSTAR in orbit. NuSTAR consists of a 10m (30′) mast that separates the optics modules on the right from the detector modules on the left. Image credit: NASA, Caltech

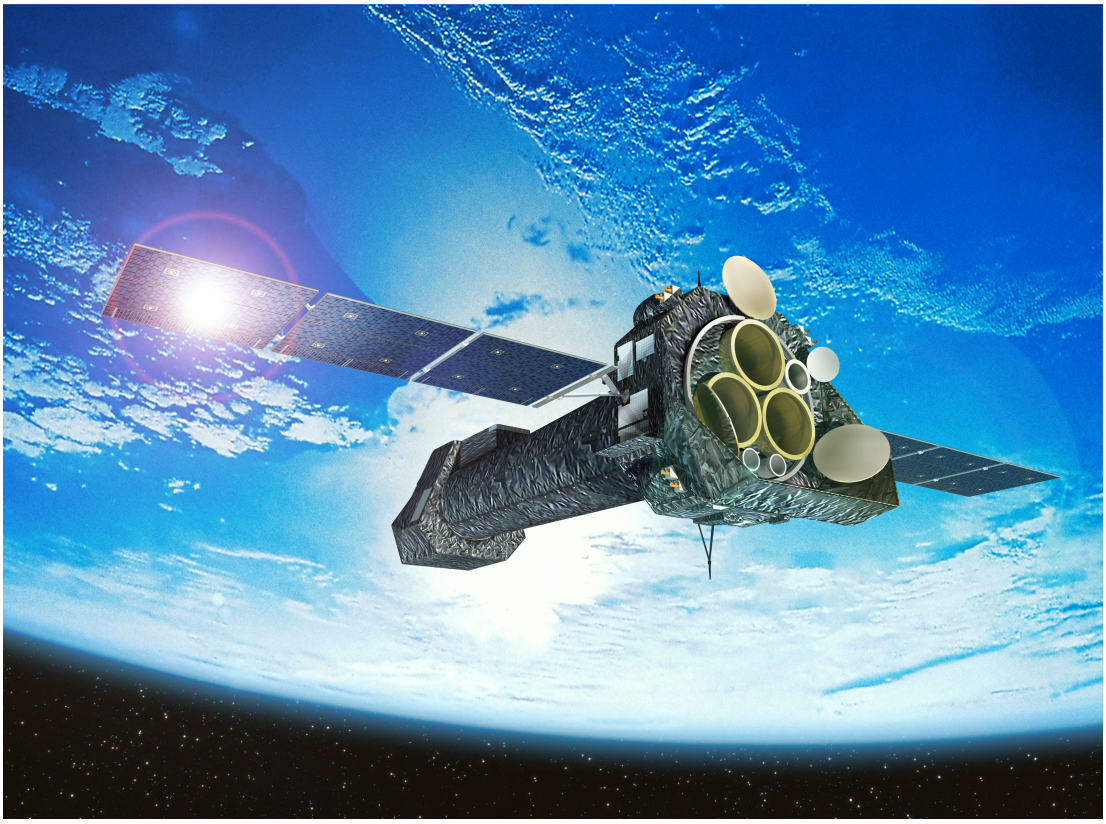

Figure 2.7: An artist's illustration of the *XMM Newton* spacecraft. Image credits: ESA. Illustration by Ducros

XMM-Newton features three X-ray telescopes with a nested mirror design. The mirrors are coated with thin layers of gold to maximize X-ray reflection. Each telescope has a diameter of 58 centimeters and a focal length of 7.5 meters.

XMM-Newton is equipped with three high-throughput X-ray instruments:

1. European Photon Imaging Camera (EPIC)
2. Reflection Grating Spectrometer (RGS)
3. Optical Monitor (OM)

2.4 Comparison of the Three X-ray Observatories

Figure 2.8 compares the effective area of *Chandra, XMM Newton*, and *NuSTAR*. The effective area of an X-ray telescope is a crucial parameter that determines its ability to collect X-ray photons. It represents the telescope's effective collecting area as a function of X-ray energy. Chandra's effective area lies between 0.7 and 7.0 keV. *Chandra* has a relatively smaller effective area compared to some other X-ray telescopes. *XMM-Newton's* effective area also varies with energy, but it is designed to have a larger collecting area. *NuSTAR* is optimized for observing high-energy X-rays and has a substantial effective area at higher energies. NuSTAR's strength is its high effective area in the hard X-ray regime (above 10 keV), which allows it to study extremely energetic phenomena, such as black holes and supernovae remnants.

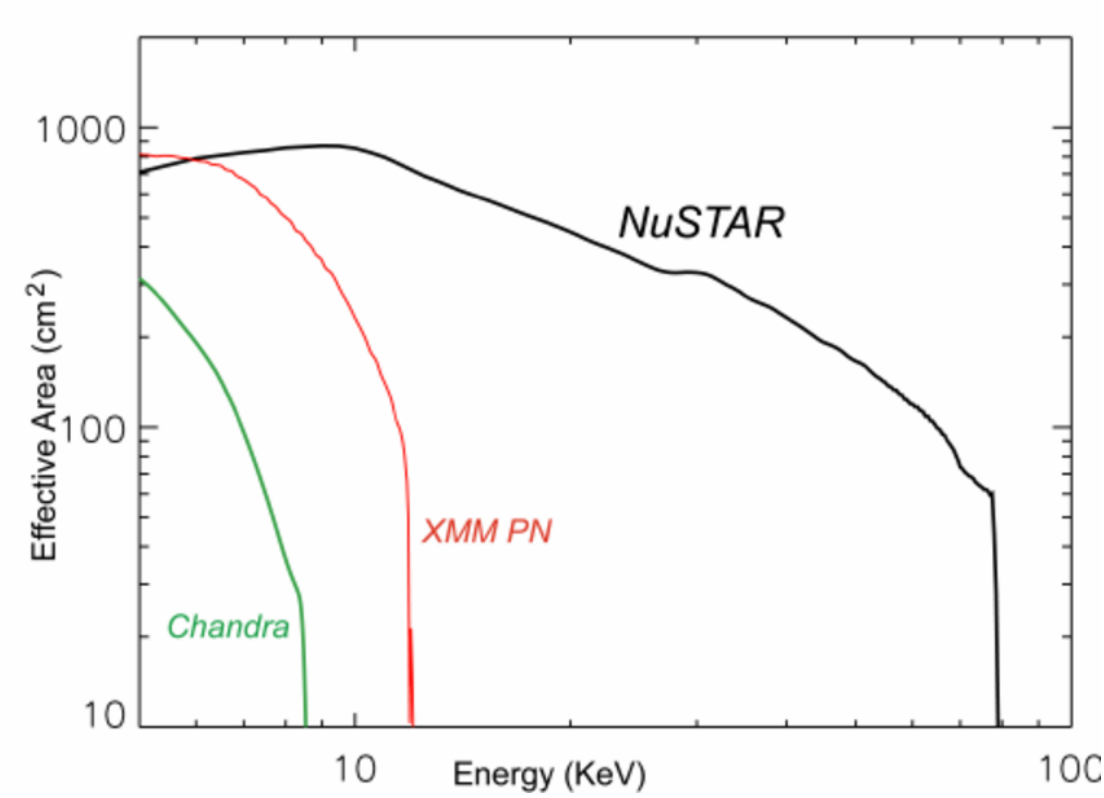

Figure 2.8: The effective areas of *Chandra, XMM* and *NuSTAR* plotted as a function of energy. *Chandra's* effective area is the least compared to others, but it has a high spatial resolution, which makes it ideal for detailed imaging of X-ray sources.

2.5 *ROSAT*

The ROSAT (from ROentgen SATellite or Röntgensatellit in German) observatory was a space-based X-ray telescope that was a joint mission between Germany, the United States, and the United Kingdom. It was launched by the German Aerospace Center (DLR) and NASA on June 1, 1990, on a Delta II rocket. ROSAT was operational from 1990 to 1999. The left panel of Fig. 2.9 shows the launch of ROSAT using a Delta II vehicle. The right panel of Fig. 2.9 shows an artist's impression of ROSAT in flight.

The main purpose of the ROSAT observatory was to conduct the first comprehensive all-sky survey and study various astronomical objects using imaging X-ray telescopes (Trümper, 1990). The primary objective of the survey was to detect and catalog X-ray sources across the entire sky. This all-sky survey, known as the ROSAT All-Sky Survey (RASS) resulted in the creation of the ROSAT All-Sky Survey Bright Source Catalogue (RASS-BSC) (Voges et al., 1997). The survey allowed for the detection and characterization of X-ray emission from stars, galaxies, and galaxy clusters (Ebeling et al., 1998).

The ROSAT telescope was placed in a highly elliptical Low Earth Orbit (LEO) during its mission. The orbital altitude of ROSAT varied between approximately 580 kilometers (360 miles) and 580,000 kilometers (360,000 miles) above the Earth's surface. ROSAT took approximately 90 minutes to complete one full orbit around the Earth.

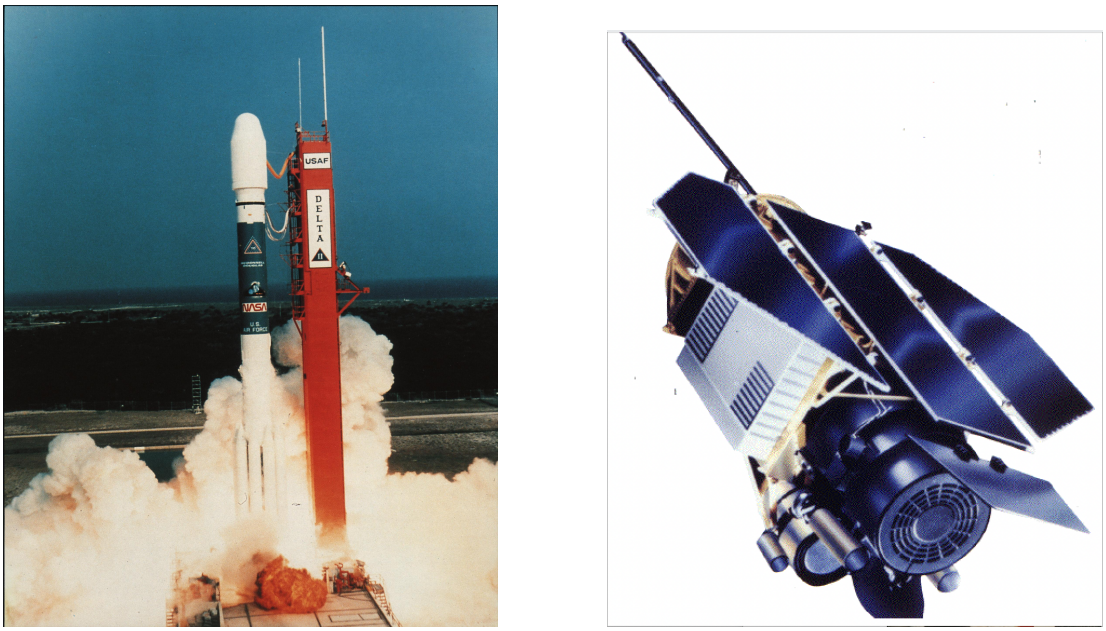

Figure 2.9: *Left:* ROSAT was launched on with a Delta II vehicle on June 1, 1990. *Right:* An artist's impression of ROSAT in flight. Image credit: Max-Planck-Institut für extraterrestrische Physik (MPE)

The ROSAT observatory was equipped with two main scientific instruments:

1. X-ray Telescope (XRT)

2. Wide Field Camera (WFC)

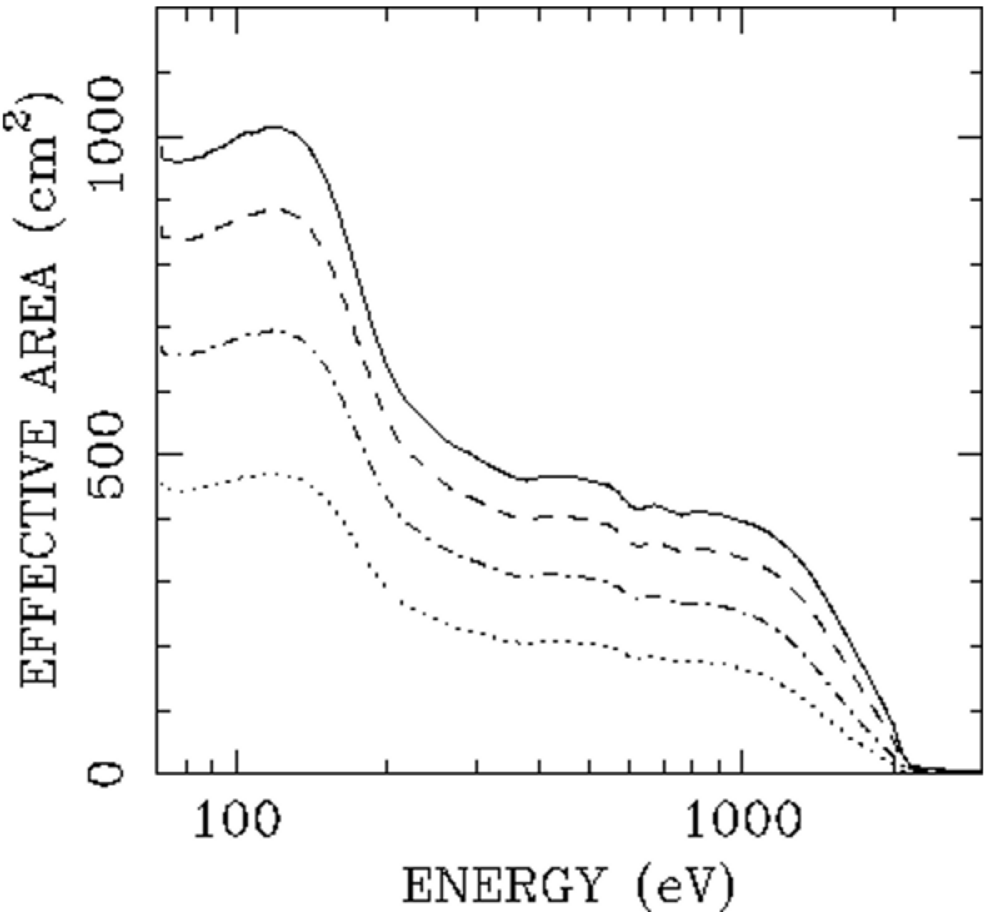

Figure 2.10: Effective area of the XMA as a function of energy. Image credit: HEASARC.

The X-ray Telescope (XRT) was the primary instrument of ROSAT. It operated in the X-ray wavelength range of 6 – 100 Å (Trümper, 1990). The XRT consists of the X-ray Mirror Assembly (XMA), two Positional Sensitive Proportional Counters (PSPC), a High-Resolution Imager (HRI), two detectors, and a deflector, as shown in the schematic diagram in the left panel of Fig. 2.10. The XMA consisted of 4 nested grazing incidence Wolter-I mirrors with a diameter of

83 cm. The nested mirror shells were designed to minimize X-ray scattering and improve the telescope's sensitivity. The focal plane detector of the XRT was a PSPC, which recorded the position and energy of incoming X-ray photons. The HRI was an imaging proportional counter with high spatial resolution designed for detailed studies of individual X-ray sources. It used microchannel plates to amplify incoming X-ray photons, resulting in high sensitivity and spatial resolution down to sub-arcsecond levels.

The primary software used for analyzing ROSAT data is the Standard Analysis Software System (SASS). SASS was developed by the Max-Planck-Institut für Extraterrestrische Physik (MPE) and is designed to process and analyze X-ray data obtained by the ROSAT observatory. SASS provides tools and algorithms for data reduction, source detection, and spectral analysis of ROSAT data (Voges et al., 1997).

2.6 *Suzaku*

Suzaku (shown in Figure 2.11), also known as the ASTRO-E2 mission, was a Japanese X-ray astronomy satellite operated by the Japan Aerospace Exploration Agency (JAXA). It was launched on July 10, 2005, and remained in operation until September 2015. Suzaku was designed to observe X-rays from various sources and conduct high-precision X-ray spectroscopy and imaging.

Suzaku's main scientific instruments included:

1. X-ray Imaging Spectrometer (XIS)

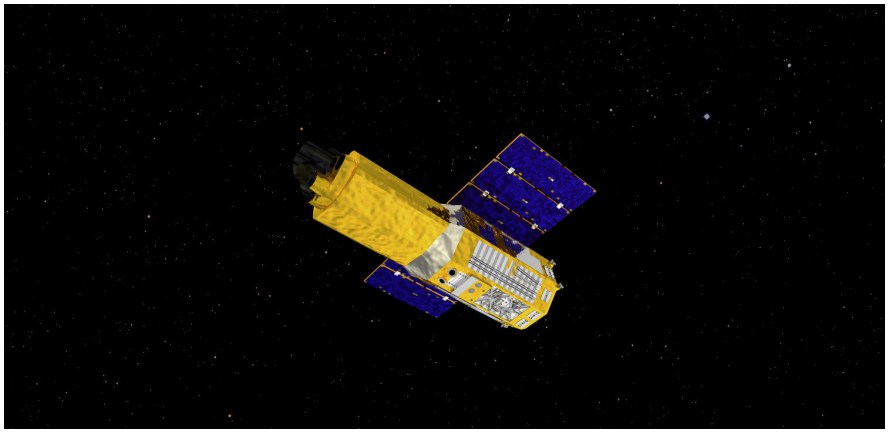

Figure 2.11: An artist's illustration of the Suzaku spacecraft. Image credit: ISAS/JAXA

2. Hard X-ray Detector (HXD)

The XIS instrument consisted of four X-ray CCD cameras with high-resolution spectroscopy capabilities. It was designed to capture X-ray images and provide detailed spectral information for various sources, such as supernova remnants, active galactic nuclei (AGNs), and clusters of galaxies. The HXD was used for observing high-energy X-rays in the hard X-ray band. It featured a combination of various detectors, making it suitable for detecting and characterizing hard X-ray sources.

Chapter 3. Analysis

3.1 Data Reduction

All the data pre-processing and reduction processes mentioned here are done using CIAO (Fruscione et al., 2006). The data is downloaded by using *download_chandra_obsid* script. Once the data has been downloaded, the data needs to be preprocessed before image analysis can be performed.

The first step is to run the *chandra_repro* script. This script automates all the steps to be followed for reprocessing a Chandra data set, which consists of using the data from the primary and secondary directories to create a new $level = 2$ event file and a new $level = 2$ Type II PHA file with the appropriate Ancillary Response Files (ARFs) and Redistribution Matrix Files (RMFs). The ARF file contains information about the effective area as a function of energy for any observation and is analogous to the sensitivity curve in optical astronomy. Fig 2.5 shows the ARF for the 21st annual cycle of *Chandra*, updated according to the latest calibration measurements. The Redistribution Matrix File (RMF) maps the relationship between each instrument channel and the appropriate incident photon energy. It is analogous to the line spread function in optical and IR astronomy.

The second step is to merge the event files from all the observations and reproject it to a common tangent point using *reproject_obs*. This merged file can be used in DS9 to analyze the data, create images, or extract spectra.

The third step is to create an exposure-corrected image using the script *flux_obs*. This script creates exposure maps for the reprojected observations obtained in the previous step and divides the latter with the former to create an exposure-corrected image, which can be further analyzed using DS9.

The lc clean routine removes flares and periods of anomalously low count rates from light curves. It is based on the program created by Maxim Markevitch. In the following Figures 3.1 to 3.10, I demonstrate the use of this script with our new, deep *Chandra* data of the merging cluster SPT J2031-4037. For all eight observations (21539, 23843, 24505, 24506. 24507, 24508, 24508, 24510, 26215, and 26479), the data was mostly clean and produced a total exposure time of 225 ks.

All the observations were free from significant anomalies or flares, as can be seen in the figures.

Once the data has been preprocessed and the image has been obtained in DS9, source and background regions are created in order to perform spectral analysis on these regions. The *specextract* script is used to extract spectra over the source and background regions.

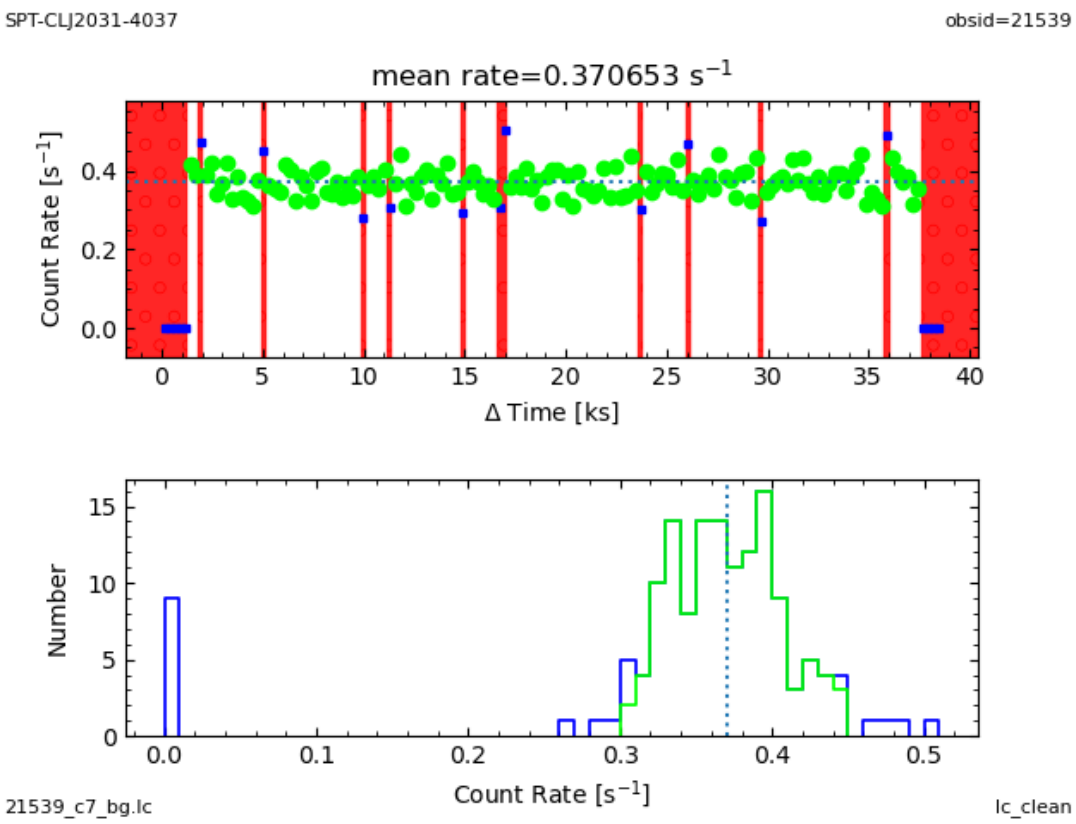

Figure 3.1: Light curve for 21539. This is done to remove periods of anomalously low counts and high flares. The lc_clean script removes anomalies that are 3 σ away from the mean (in blue).

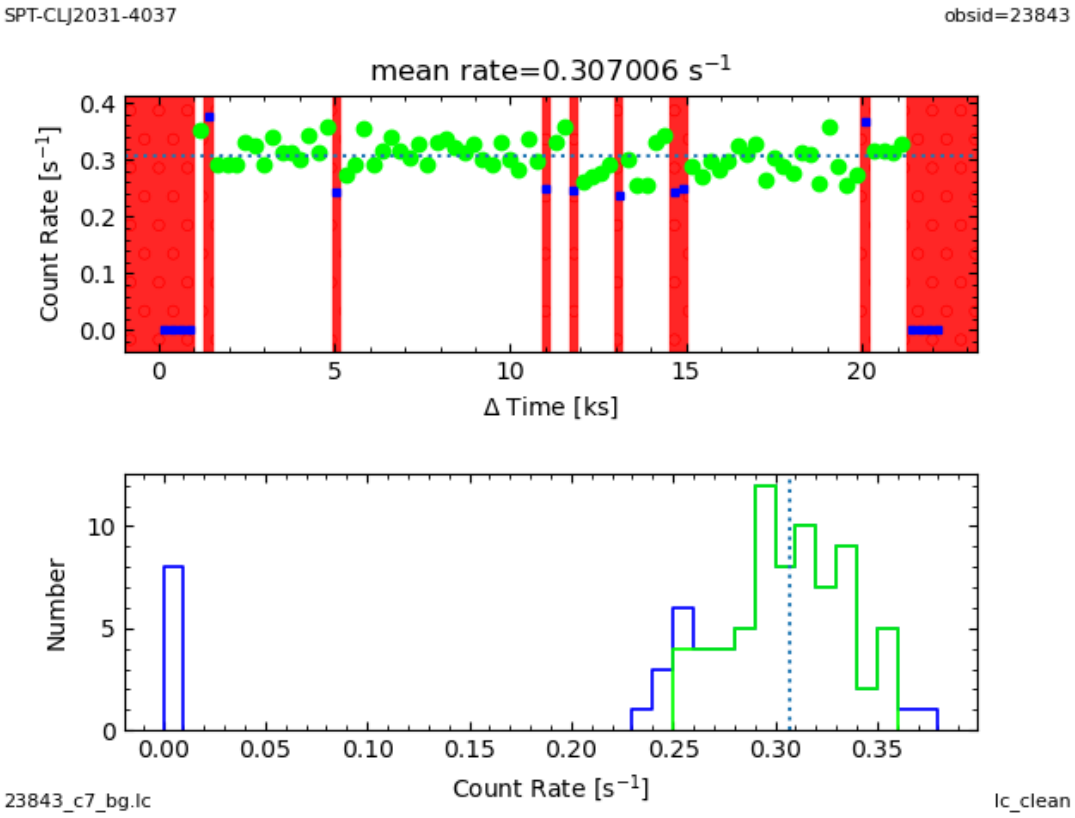

Figure 3.2: Light curve for 23843.

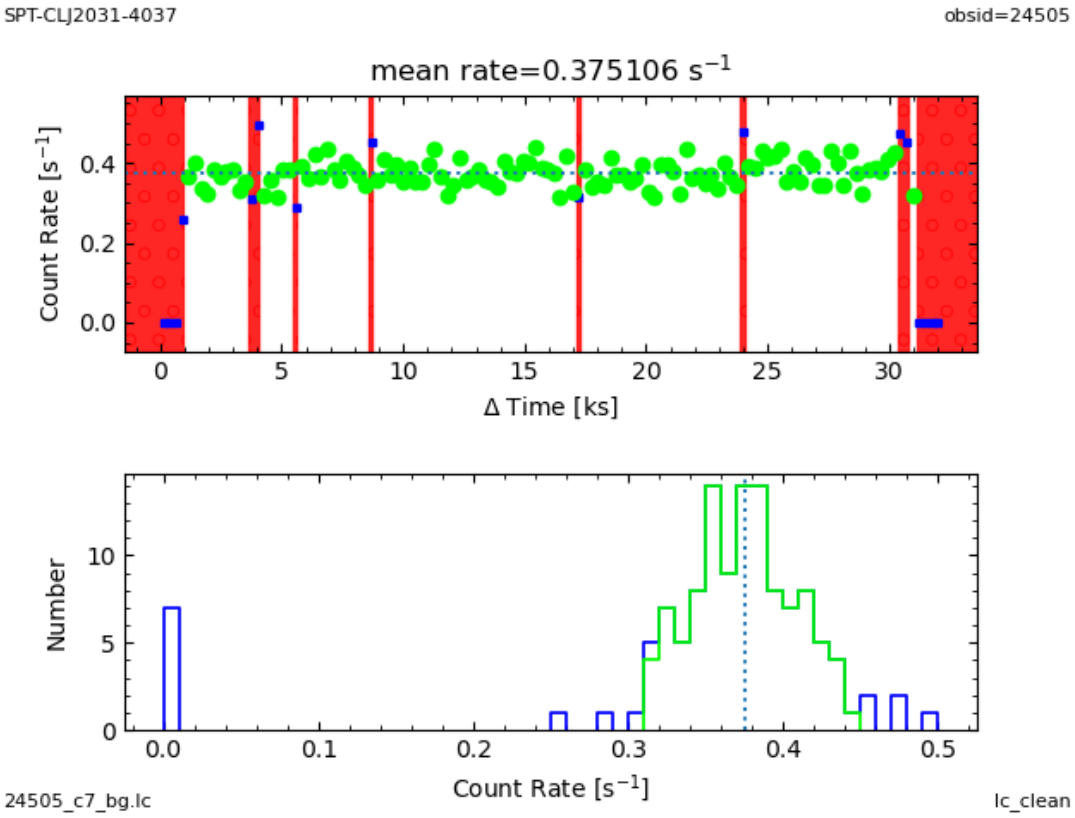

Figure 3.3: Light curve for 24505.

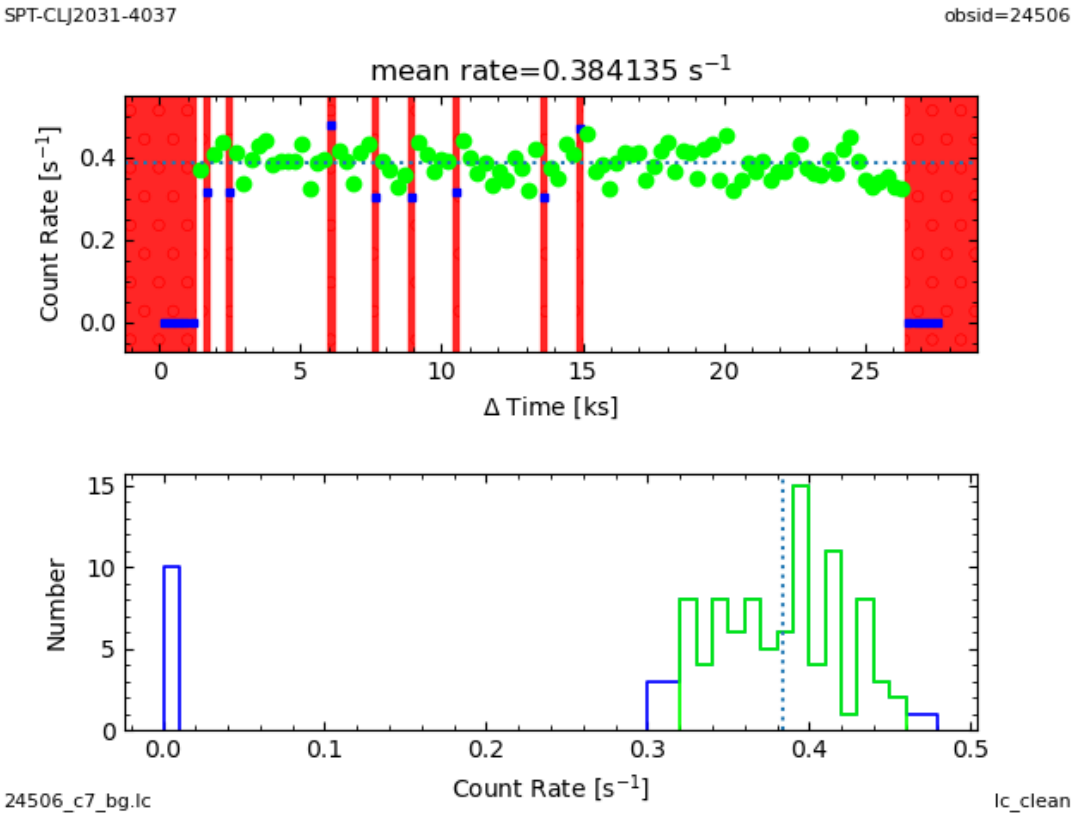

Figure 3.4: Light curve for 24506.

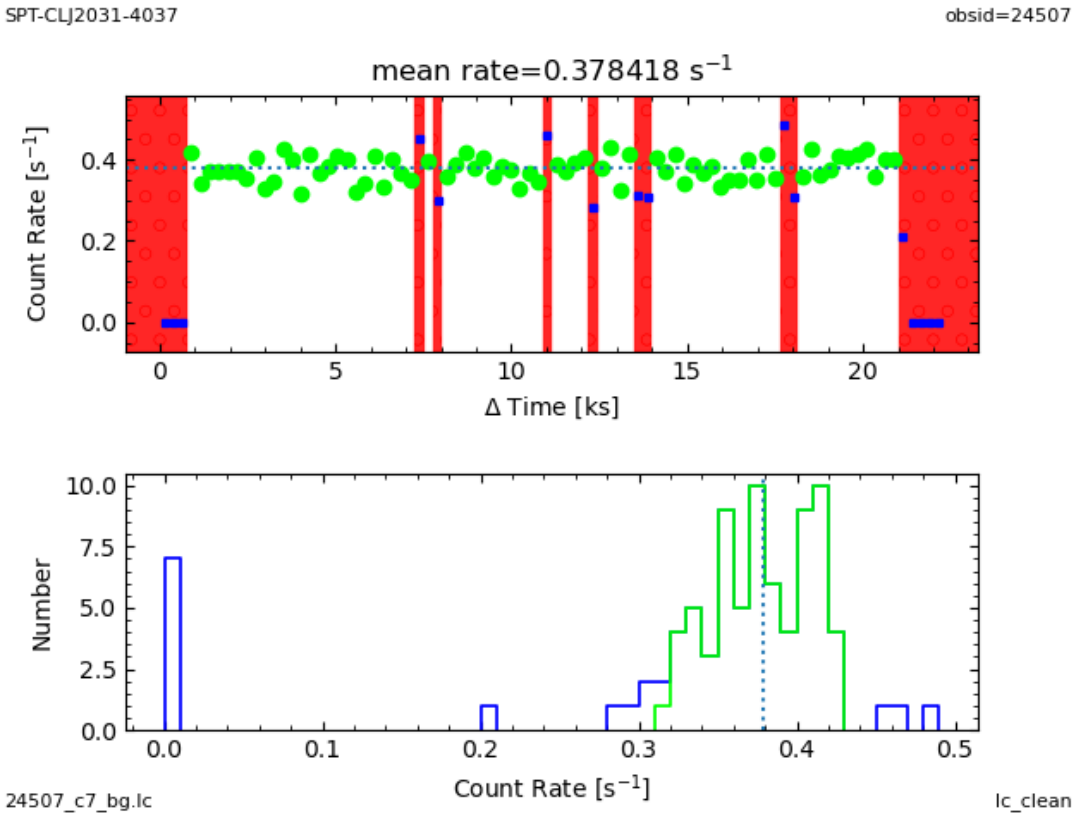

Figure 3.5: Light curve for 24507.

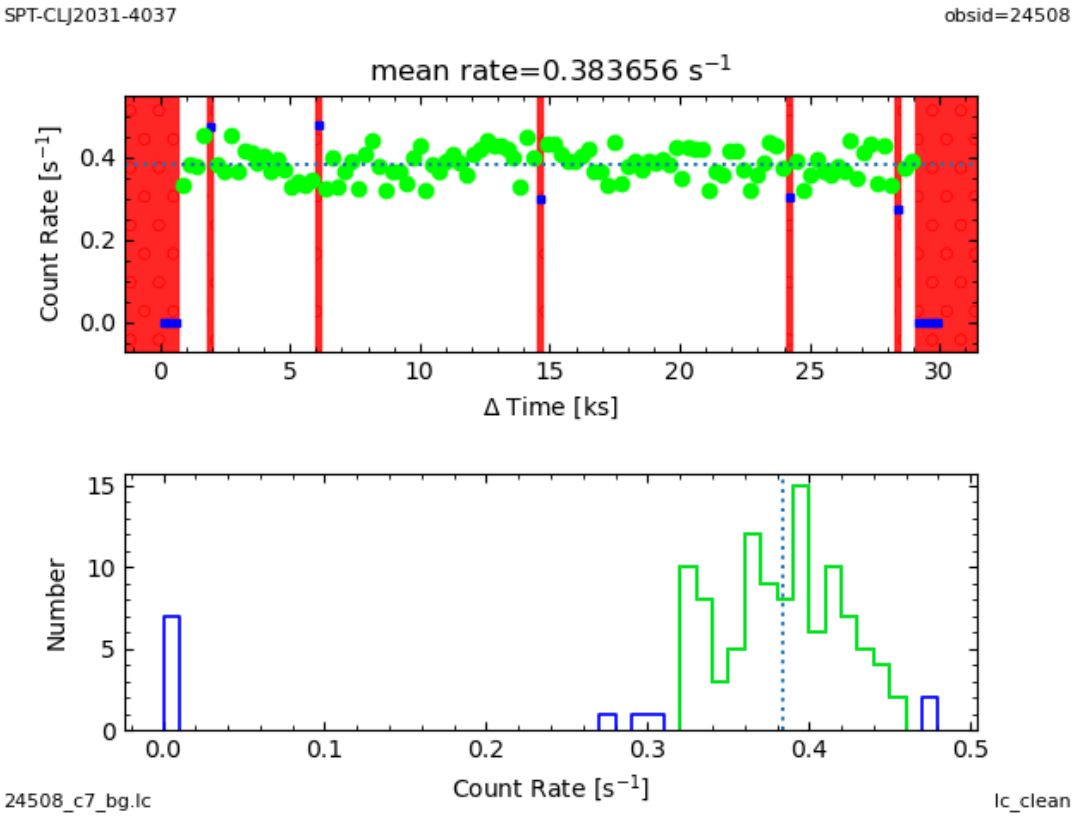

Figure 3.6: Light curve for 24508

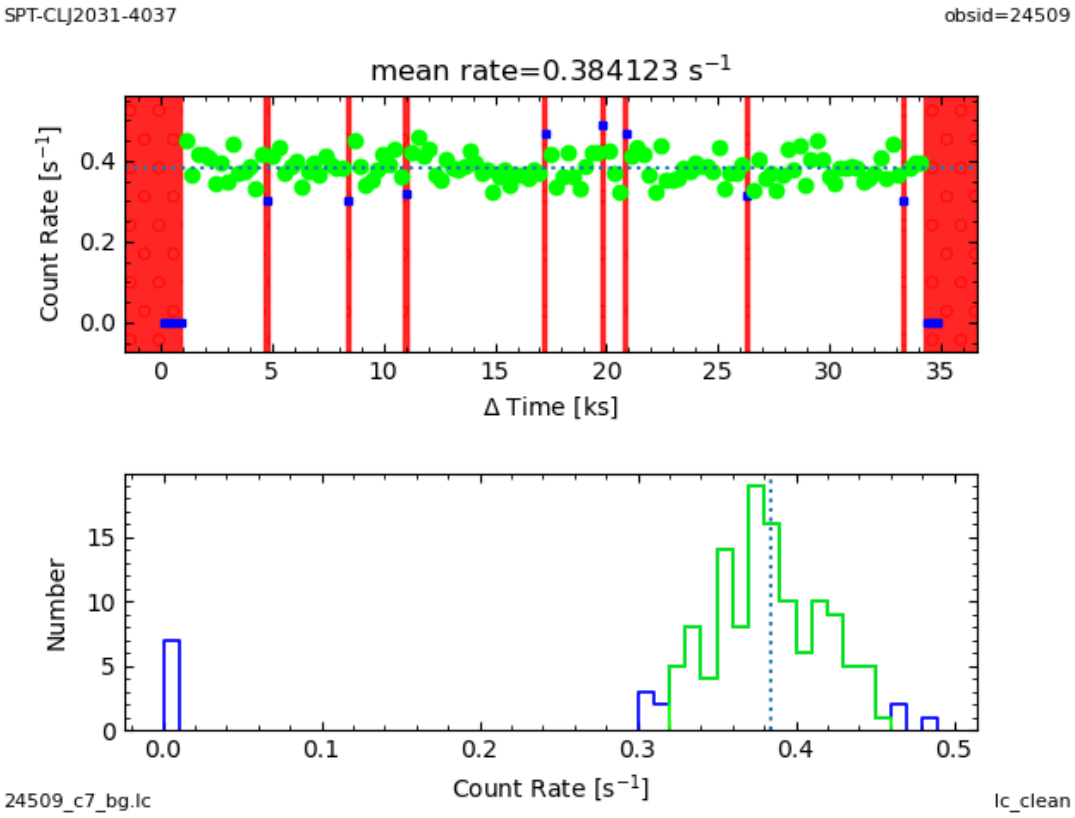

Figure 3.7: Light curve for 24509

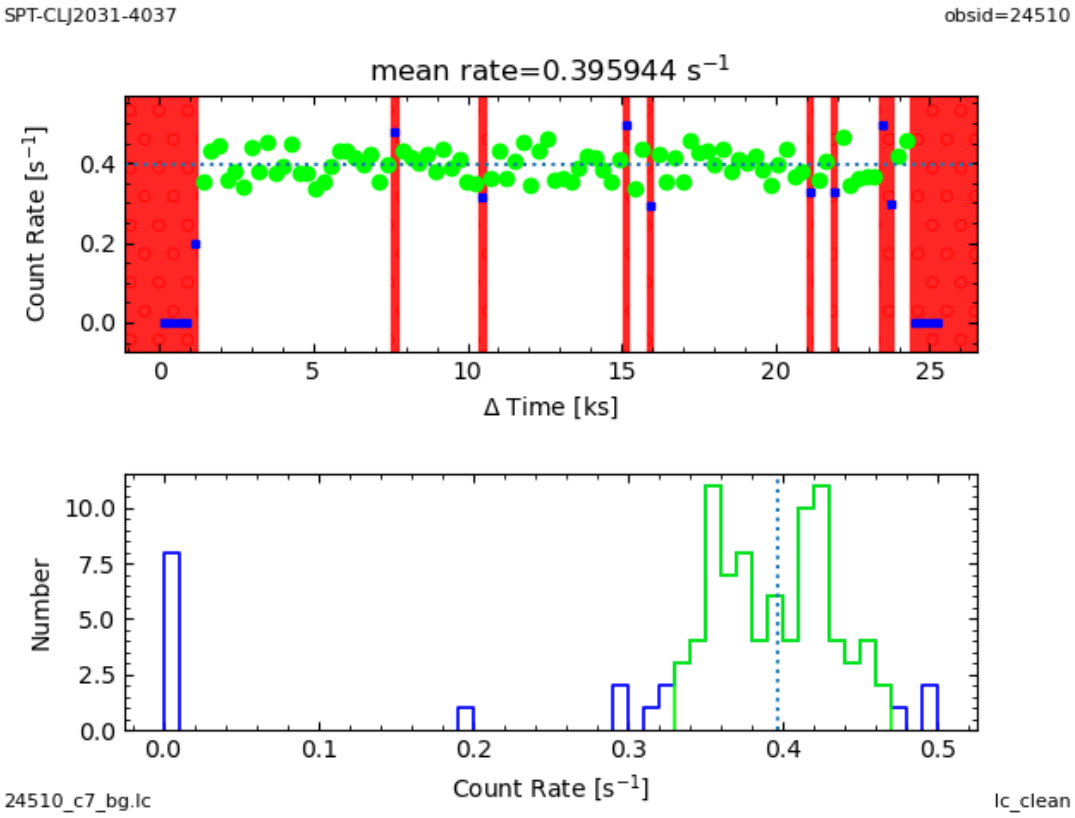

Figure 3.8: Light curve for 24510

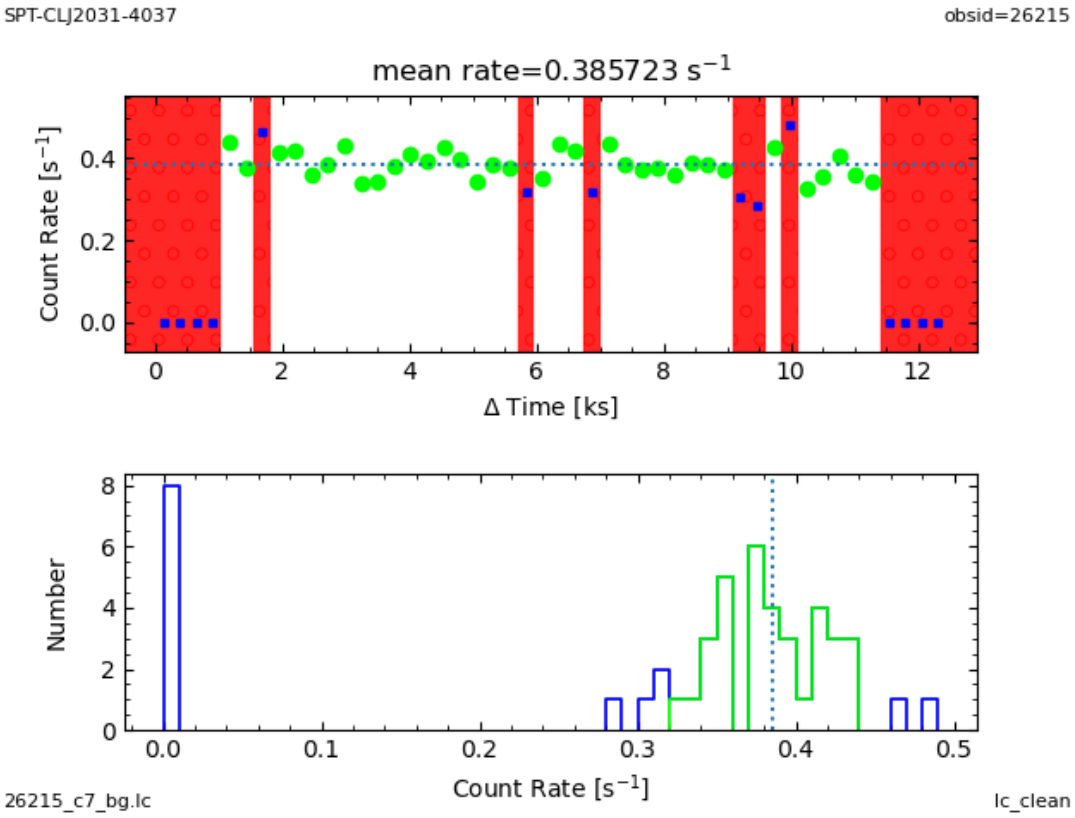

Figure 3.9: Light curve for 26215

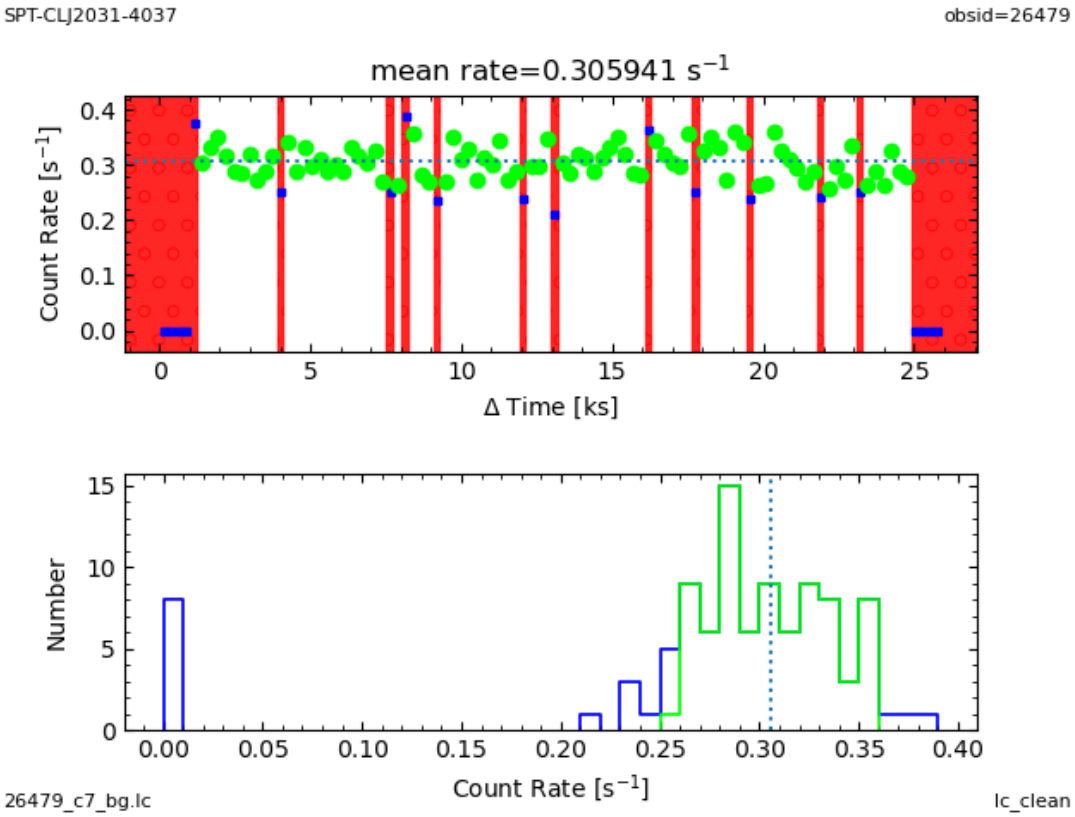

Figure 3.10: Light curve for 26479

3.2 Image Analysis Using GGM

Gaussian gradient magnitude (GGM) refers to a mathematical operation that computes the magnitude of the gradient of an image using a Gaussian filter. The GGM is computed by convolving an image with a Gaussian filter, which is a smoothing filter that is typically used to reduce noise and blur an image. The convolution operation computes the weighted sum of the pixel intensities in the image, with the weights determined by the Gaussian function. The resulting output is an image that highlights areas of rapid intensity changes, such as edges or boundaries, in the original image. GGM can be used in various image processing tasks, such as edge detection, feature extraction, and image enhancement. We use GGM to analyze our images by detecting the gradients in the surface brightness. The steeper the gradient, the brighter the surface brightness edges appear in the image.

3.3 Spectral Analysis

Once the data has been cleaned and reduced, the "source region" is selected for analysis, and a "background region" is used to estimate and subtract the background contribution. The *specextract* script creates source spectra and background spectra.

The data that is obtained from *Chandra* is in the form of photon counts (C) within specific instrument channels (I). The observed spectrum of the source is related to the actual spectrum of the source $f(E)$ by:

$$C(I) = \int f(E)R(I,E), dE, \tag{3.1}$$

where $R(I,E)$ is the instrumental response and is proportional to the probability that an incoming photon of energy E will be detected at channel I.

Although this would imply that rearranging equation 3.1 will determine the actual spectrum, generally, it is not possible. Alternatively, a model spectrum $f(E)$, which may be described in terms of a few parameters, is chosen and is 'fit' to the observed data, which is convoluted with the instrumental response. The extracted spectra for can be fitted using XSPEC, an X-ray spectral fitting program. In order to fit our *Chandra* data, the PHABS (APEC) multiplicative model has been used.

The PHABS (Photoabsorption Model) is a component which accounts for the absorption of X-ray photons by intergalactic gas and dust along the line of sight from the source to the observer. The PHABS model calculates the X-ray absorption as a function of energy using the cross-sections of the absorbing elements. It is parameterized by the hydrogen column density (N_H), which represents the amount of absorbing material along the line of sight.

The APEC (APEC Thermal Plasma Emission Model)is a component which models the emission of X-ray photons from a hot, optically thin thermal plasma. It is based on the Astrophysical Plasma Emission Code (APEC), which calculates the X-ray emission spectrum of a hot gas in collisional equilibrium. The parameters of the APEC model typically include the temperature of the plasma

(kT), the elemental abundances, and the normalization factor (which is related to the emission measure of the plasma).

Fitting with this model gives us the temperature values of the electrons in the ICM of the cluster, thus generating a temperature profile.

3.4 Surface Brightness and Density Profiles

To extract surface brightness profiles and density profiles of *Chandra* data, PROFFIT is used. PROFFIT (ProFit for X-ray spectral analysis) is a software tool designed for the analysis of X-ray surface brightness and density profiles from Chandra X-ray Observatory data. The basic tool used by me for extracting surface-brightness profiles is SECTOR. This tool extracts the surface brightness profiles from the input image for any custom binning. The center of the surface-brightness profile can either be computed automatically or supplied by the user. These profiles can then be fitted by a model to obtain the density profiles. For my analysis of SPT J2031, I have used the broken power-law gas density model for the fitting.

Chapter 4. A Rare, Strong Shock Front in the Merging Cluster SPT-CLJ 2031-4037

4.1 Introduction

Galaxy clusters, found at the nodes of the large-scale structures in the universe, are the most massive gravitationally bound and virialized structures in the Universe. They are formed via accretion, gravitational infall, and hierarchical mergers of smaller sub-clusters and galaxy groups (Markevitch and Vikhlinin, 2007). Mergers of galaxy clusters are the most energetic events in the Universe after the Big Bang, wherein the sub-clusters collide at velocities of $\sim 10^3$ km s^{-1}, releasing energy of the order of 10^{64} ergs (Markevitch et al., 1999). During such a merger, the galaxies and dark matter of both clusters interact only gravitationally and move unhindered through the region of the collision (Clowe et al., 2006).

X-ray observations of the intracluster medium (ICM) in merging clusters reveal a disturbed morphology consisting of sharp surface brightness edges, such as shock fronts and cold fronts (Russell et al., 2022). Many of these previously unobserved phenomena were revealed only due to *Chandra's* sub-arcsecond spatial resolution. X-ray observations of merging galaxy clusters, when combined with gravitational lensing studies, directly demonstrate the existence of dark matter (Clowe et al., 2004, 2006; Bradač et al., 2006) and give estimates on the constraints

on the dark matter self-interaction cross-section (Spergel and Steinhardt, 2000; Markevitch et al., 2004; Randall et al., 2008). The synchrotron radiation of relativistic particles produced as a result of cluster mergers (Brunetti, 2003) results in radio halos and radio relics (Feretti et al., 2002; Ferrari et al., 2008; Cassano, 2009) and inverse Compton hard X-ray emission at high energies (Fusco-Femiano et al., 1999, 2005; Rephaeli and Gruber, 2002).

A fraction of the kinetic energy released during mergers is dissipated into the ICM via shocks and turbulence and may also cause non-thermal phenomena such as amplification of magnetic fields in the ICM and acceleration of ultrarelativistic particles in the cluster (Sarazin, 2008; Markevitch and Vikhlinin, 2007; Blandford and Eichler, 1987). Shock fronts, seen as sharp discontinuities in surface brightness in X-ray observations, provide a rare chance to observe and investigate such merger systems and their geometry. Shock fronts can be used to measure gas bulk velocities and also to understand transport processes in the ICM, including electron-ion equilibration and thermal conduction, magnetic fields, and turbulence (Markevitch and Vikhlinin, 2007; Takizawa, 1999).

Currently, observations of shock fronts are the only method to determine how electrons and ions equilibrate after heating and to obtain bulk gas velocities in the plane of the sky (Russell et al., 2010). The measurement of temperature and density of the gas before and after the occurrence of the shock, and thereby the jumps in these quantities as well, can be used to compute the Mach number of the shock front using the Rankine-Hugoniot jump conditions. Thus, the *Chandra* observations of the merger shocks allow for mapping of post-shock electron

temperature, determination of Mach number and shock speed, and estimation of the electron heating timescale, providing a comprehensive analysis of these phenomena in a single observation (see Russell et al. (2022) and the references within).

While a number of clusters have been found to have shock-heated regions, the detection of a cluster merger with sharp surface brightness edges and a distinctive high-temperature jump is rare due to the requirement of favorable merger geometry (ZuHone and Su, 2022). In fact, only a handful of merger shock fronts with a high Mach number, $M > 2.0$ have been discovered by *Chandra*, such as the Bullet Cluster with $M = 3.0 \pm 0.4$ (Markevitch, 2006b), A2146 with $M = 2.3 \pm 0.2$ (Russell et al., 2010, 2012, 2022), A665 with $M = 3.0 \pm 0.6$ (Dasadia et al., 2016), El Gordo with $M \geq 3$ (Botteon et al., 2016), A520 with $M = 2.4^{+0.4}_{-0.3}$ (Wang et al., 2018), and A98 with $M = 2.3 \pm 0.3$ (Sarkar et al., 2022). *Chandra* has also determined shock fronts with $M < 2.0$, such as A2744 with $M = 1.41^{+0.13}_{-0.08}$ (Owers et al., 2011), A754 with $M = 1.57^{+0.16}_{-0.12}$ (Macario et al., 2011), A521 with $M = 2.4 \pm 0.2$ (Bourdin et al., 2013) and A2034 with $M = 1.59^{+0.06}_{-0.07}$ (Owers et al., 2014).

Understanding the method of shock heating of the ICM is fundamental to understanding the heating of the ICM in galaxy clusters. However, it remains a matter of great debate (Wang et al., 2018). At present, there are two models to explain the shock-heating of the ICM - the Coulomb collisional model and the instant shock-heating model. At the passage of a shock front, the ions in the ICM gas are heated dissipatively, whereas the electrons, owing to their higher

thermal velocity, are compressed adiabatically and undergo Coulomb collisions to eventually reach thermal equilibrium with the ions. The Coulomb-collisional model of heating is observed in Abell 2146 (Russell et al., 2022). However, if the equilibration timescale is much shorter than the Coulomb timescale, then the electrons attain thermal equilibrium with the ions instantaneously (ZuHone and Su, 2022). This instant model of heating is observed in solar wind shocks and has been used to explain the shock heating in the Bullet Cluster (Markevitch, 2006b), A520 (Wang et al., 2018), and A98 (Sarkar et al., 2022).

High Mach number shocks are the best way to determine the model that best explains the shock-heating. The higher the Mach number of a shock, the more it separates the two models. Shock fronts with high Mach numbers are rare occurrences, making them extremely valuable for cluster astrophysics as they offer insights into the heating of the ICM that cannot be obtained through any other means. Current X-ray observatories are only capable of measuring the electron temperature, and direct measurements of the ion temperature are not feasible. Thus, cluster shocks, where the electron-ion equilibration occurs over distances of $\sim$ 200 kpc behind the shock, provide us with a powerful method of investigating the electron and ion temperatures.

SPT-CLJ2031-4037 (hereafter SPT J2031) is a massive merger system with $M_{500} \sim 8 \times 10^{14}$ $M_\odot$ (Chiu et al., 2018), and X-ray luminosity $L_{[0.1-2.4keV]} = 1.04 \times 10^{45}$ erg s^{-1} (Piffaretti et al., 2011) at redshift $z = 0.34$ (Böhringer et al., 2004). The morphologically disturbed cluster (Nurgaliev et al., 2017) was first discovered in a ROSAT-ESO Flux Limited X-ray (REFLEX) Galaxy Cluster sur-

vey (Böhringer et al., 2004) as RXCJ2031.8-4037. It was also cataloged via the Sunyaev-Zel'dovich effect by the South Pole Telescope (SPT) (Plagge et al., 2010; Williamson et al., 2011) and by the Planck Satellite (Planck Collaboration et al., 2016). The redshift of this system is similar to that of the Bullet Cluster (redshift $z = 0.3$), and hence, the sizes of their angular features are comparable.

Recent radio observations of SPT-CLJ2031-4037 performed with the GMRT at 325 MHz and with VLA (L-band observation) at 1.7 GHz revealed diffuse radio emission in the cluster (Raja et al., 2020). The emission observed with the GMRT, which is $2.7' \times 2.1'$ in size, was found to surround the central BCG when compared with the optical observations. The spectral index of the radio halo between the frequencies 325 MHz and 1.7 GHz was reportedly -1.35 ± 0.07. Based on these results (Raja et al., 2020) speculated a merger event in the past, which can be confirmed with deep X-ray observations.

SPT-CLJ2031-4037 has also been recently observed by *NuSTAR*, where analysis of the deep observations reveals that the hard X-ray emission in the cluster can be described by a non-thermal component even though the possibility of a purely thermal origin is not ruled out (Mirakhor et al., 2022).

Previous 10 ks *Chandra* observation revealed two surface brightness peaks, indicating that it is very likely a major merger. To investigate the possible occurrence of a shock front, I obtained deep *Chandra* observations.

In this chapter, I present results from deep *Chandra* observations of SPT J2031, which include the detection of a strong merger shock, the spatially resolved temperature map, and the preferred method of shock-heating. In section 4.2 I

outline details of the observations and discuss the data reduction. In sections 4.3 and 4.4, I present the image analysis and show the emissivity, temperature map, pseudo-pressure map, and the GGM filtered image. In section 4.5, I analyze the primary shock and the southeastern edge in more detail by obtaining the surface brightness profiles and temperature profiles. The post-shock electron temperature profiles are compared to the Coulomb collisional and instant shock heating models for electron-ion equilibration.

I assume a flat cosmology with $H_0 = 70$ km s^{-1} Mpc^{-1}, $\Omega_m = 0.3$, $\Omega_\Lambda = 0.7$. The redshift is $z = 0.34$, where 1" corresponds to 4.892 kpc. All the error bars are at a 68% confidence level unless stated otherwise.

4.2 Chandra Data Analysis

SPT-J2031 was observed by the *Chandra* Advanced CCD Imaging Spectrometer (ACIS) detector in the Very Faint (VFAINT) mode for a total of 256 ks spread over 10 observations (PI: S. A. Walker). All observations were done with the ACIS-S. The Obs. ID, dates of observation, approximate exposure time, and cleaned exposure time are listed in Table 4.1.

Table 4.1: Details of the deep ($\sim 250ks$) *Chandra* observations of the SPT-CLJ2031-4037 Cluster utilized for the analysis shown in this paper.

Obs ID	RA	Dec	Date	Exp time (ks)	Cleaned time (ks)
21539	20 31 51.10	-40 37 22.10	2019 Aug 05	36.0	32.8
24505	20 31 51.64	-40 37 19.64	2021 Aug 04	29.7	27.6
24508	20 31 51.64	-40 37 19.64	2021 Aug 09	27.7	26.4
24510	20 31 51.64	-40 37 19.64	2021 Aug 23	22.75	20.7
24509	20 31 51.64	-40 37 19.64	2021 Aug 28	32.6	30.6
24507	20 31 51.64	-40 37 19.64	2021 Nov 28	19.8	17.7
26215	20 31 51.64	-40 37 19.64	2021 Nov 28	9.9	8.4
24506	20 31 51.64	-40 37 19.64	2021 Nov 30	24.7	22.7
23843	20 31 51.64	-40 37 19.64	2022 Jul 26	19.8	17.8
26479	20 31 51.64	-40 37 19.64	2022 Jul 29	23.3	20.4

4.2.1 Data Reduction

All data reduction was performed using CIAO, *Chandra's* data analysis system (Fruscione et al., 2006) (version 4.14), and CALDB, the calibration database (version 4.10.2) provided by the *Chandra* X-ray Center (CXC). The primary data set given by the detector is a list of photons with measurements like the spatial resolution of the X-ray photons that arrive at the detector, the time of arrival, and the energy of that photon, called the event 1 file. The event 1 files were reprocessed using the *chandra_repro* script, taking into account the most recent calibrations to the detector by applying the latest charge transfer inefficiency (CTI) correction, time-dependent gain adjustment, gain map to obtain the appropriate response files, new bad pixel files, and the processed level 2 event files.

The *deflare* routine, which uses the *lc_clean* script created by M. Markevitch, was used to detect and get rid of flares and periods of anomalously low count rates from the input light curves. As can be seen in Table 4.1, the data were mostly clean, and the final cleaned exposure was 225 ks.

The cleaned and reprocessed files were reprojected to create a merged image using *merge_obs* in the soft band ($0.5 - 2.5$ keV) and in the broad band ($0.7 - 7.0$ keV), and a merged event file and exposure-corrected images were created. The *merge_obs* script combines the *reproject_obs* and *flux_obs* scripts. The *reproject_obs* script finds the appropriate ancillary response files (ARF) for all the event 2 files, matches up with the observations, and creates a new single event file

by merging the event files of individual observations. The *flux_obs* script creates exposure maps and the exposure-corrected image. The bright point sources in the exposure-corrected image were removed by first excluding the regions by eye, and the excluded regions were filled in using the *dmfilth* script. This script replaces the pixel values in the excluded regions of the image with values interpolated from the surrounding regions using a Poisson probability distribution.

Blank-sky observations were extracted using the *blanksky* script and were then reprojected to match the coordinates of the observation. The blank-sky backgrounds were normalized by matching their count rate in the $9.5 - 12$ keV energy band to that of the observed data set, thus ensuring uniformity.

4.3 Image Analysis

Figure 4.1 shows an exposure-corrected image of the cluster created by combining all the individual *Chandra* observations, with the point sources removed in the $0.5 - 7.0$ keV energy band. The geometry of the image suggests that the system recently underwent a merger where the sub-clusters passed through each other along the east-west direction. The X-ray emission is seen extended from the SE to the NW direction. There are two sharp surface edges that can be seen here: "Primary Shock" in the northwestern region, and the "SE edge" in the southeastern region. The brightest X-ray peak lies behind the SE edge and is marked by a blue cross in Figure 4.1. A secondary X-ray peak marked by a red cross in Figure 4.1 lies behind the Primary shock in the Northwest. In previous shallow 10 ks observations, only two bright peaks could be observed,

and no edges were visible. These deep *Chandra* observations have helped resolve the sharp brightness edges and allow us to produce a more detailed temperature map.

In Figure 4.2, *Chandra* X-ray contours from our new observations are superimposed on an HST (Hubble Space Telescope) image of SPT J2031. The grayscale image is the HST image of SPT J2031 obtained by using the F814W filter. The *Chandra* contours are overlaid on this optical image in green. The white dashed circles show the two Brightest Cluster Galaxies (BCG). BCG 1 is close to the primary X-ray peak, and BCG 2 is approximately at the location of the primary shock front and offset from the secondary X-ray peak. The direction of the merger axis is estimated to be roughly from the Northwest (NW) to the southeast (SE), passing through the center of the two galaxy distributions.

The BCG 2 shown in the figure is SMACSJ2031.8-4036, which has been extensively studied by deep HST and MUSE as it is a strong lensing cluster. According to the mass modeling presented in Richard et al. (2015), the eastern component has a mass $M_{east} = 2.4 \times 10^{14} \mathrm{M}_{\odot}$.

In galaxy cluster mergers, the galaxies within the sub-cluster behave like collisionless particles and lead the baryonic gas after the collision. This lag between the motion of the sub-cluster galaxies and the baryonic gas can result in an offset between the centroids of the main mass distribution and the elongated peak in the X-ray emission (Canning et al., 2011). Comparing the contours representing the brightest X-ray peaks in Figure 4.1 with the BCGs in Figure 4.2, there is an offset of the brightest X-ray peaks from the BCGs, indicating that the

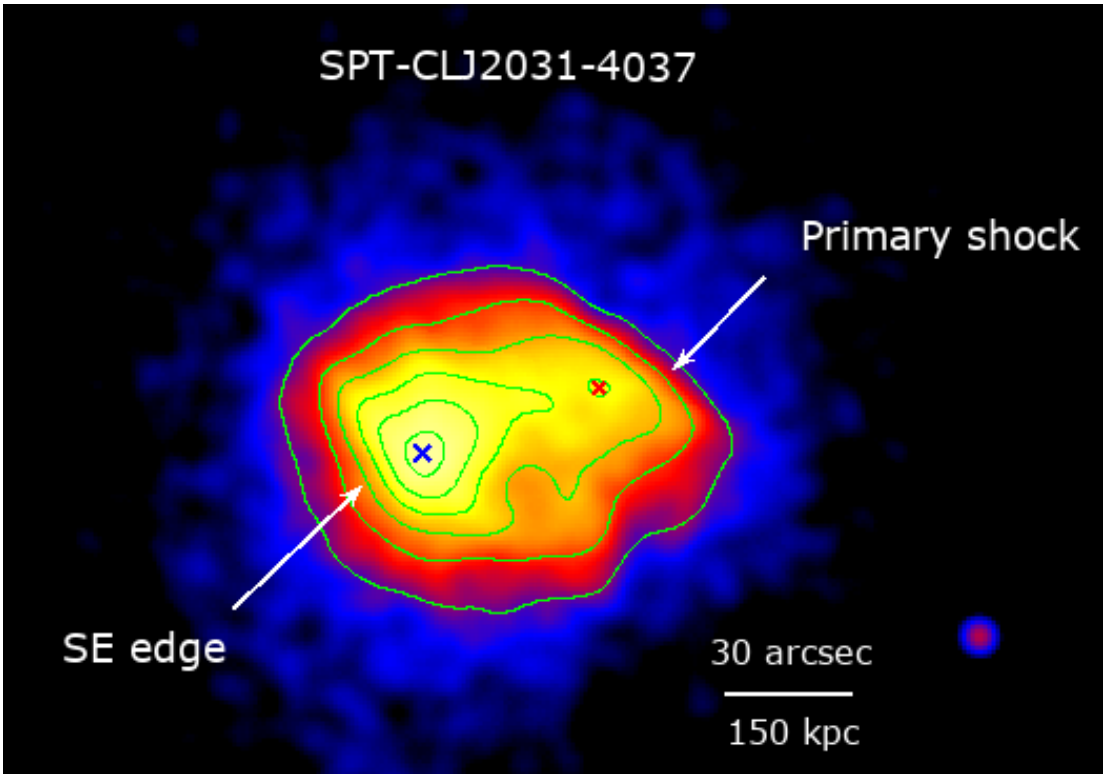

Figure 4.1: The exposure-corrected image of SPT-CLJ2031-4037 with the point sources removed in the $0.5 - 7.0$ keV energy range, smoothed with Gaussian $\sigma = 3$. North is up, and East is to the left. Two sharp surface brightness edges are seen here, the Primary Shock in the Northwest and the SE edge in the southeast of the image. The brightest X-ray peak lies behind the SE edge, marked by the blue cross. An additional X-ray peak lies behind the primary shock, marked by a red cross. The green lines represent *Chandra* contours.

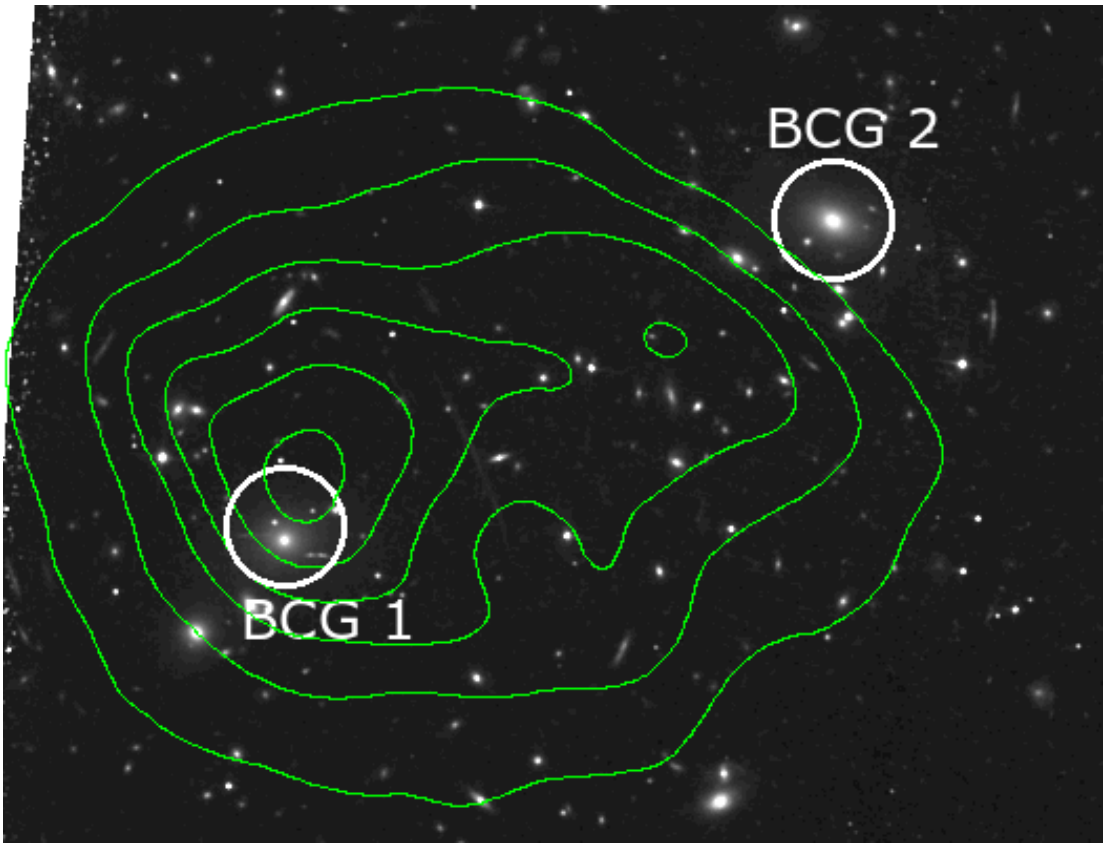

Figure 4.2: HST (Hubble Space Telescope) image of SPT-CLJ2031-4037 (in grayscale) obtained using the F 814W filter overlaid with *Chandra* contours (in green). The white dashed circles show the two sub-clusters with their Brightest Cluster Galaxy (BCG). BCG 1 is close to the primary X-ray peak, and BCG 2 is approximately at the location of the primary shock front. The coordinates are shown to be accurate by a number of well-matched point sources.

system recently underwent a merger. In Figure 4.2, the brightest X-ray peak is offset from BCG 1 by ∼0.12 arcmin (∼ 36 kpc), and the secondary X-ray peak is offset from BCG 2 by ∼ 0.39 arcmin (∼ 117 kpc).

I obtained a Gaussian Gradient Magnitude (GGM) filtered image of the merger, as shown in the bottom right of Figure 4.3, in the $0.5 - 7.0$ keV energy range. GGM filtering is a robust edge-detection technique which is very useful in resolving the substructures in a cluster core, as well as at cluster outskirts (Sanders et al., 2016; Walker et al., 2016). The GGM filter detects gradients in the surface brightness, and the steeper the gradient, the brighter these edges appear in the image. For the GGM image shown here, I filtered it at a scale of 3 pixels, where I have binned the *Chandra* image by a factor of 2 so that each pixel is 0.949" wide. In this GGM image, two surfaces with steep brightness were observed, the Primary shock and SE edge, as shown with the dashed red lines in the bottom right of fig 4.3.

4.4 Spatially Resolved Spectroscopy

Spatially resolved spectroscopy techniques were used to produce maps of projected gas properties of the cluster (see Figure 4.3). The central $\sim 3 \times 3$ arcmin region was divided into bins using the Contour Binning algorithm (Sanders, 2006), which creates bins based on the variations in surface brightness. The signal-to-noise ratio was chosen to be 32 (∼ 1000 counts) for obtaining the bins, as was used in Russell et al. (2012). For all the regions obtained this way, spectra were extracted for each observation, and appropriate RMFs and ARFs were generated.

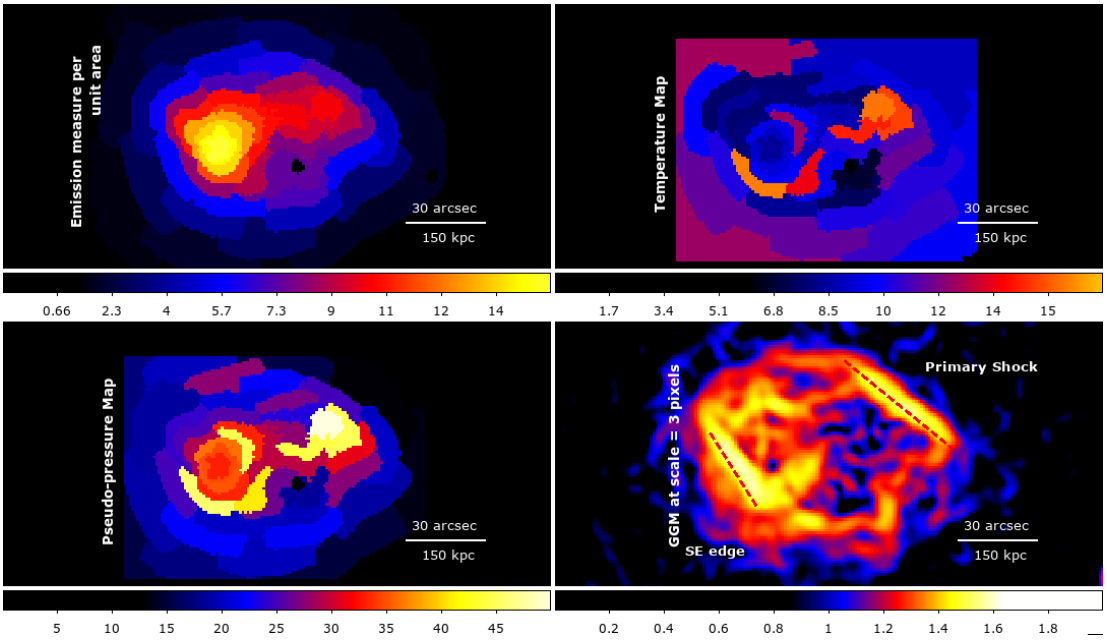

Figure 4.3: *Top left:* Projected emission per unit area (cm^{-5} $arcsec^{-2}$. *Top Right:* Projected Temperature Map (keV) with S/N = 32. *Bottom Left:* Projected pseudo-pressure map (keV cm^{-5} $arcsec^{-2}$), obtained by multiplying the emission measure and temperature maps. The small black circles in the emission and temperature map and the white ones in the pseudo-pressure map are the excluded point sources. *Bottom Right:* GGM image of SPT-CLJ2031-4037 in the $0.5 - 7.0$ keV energy range at scale = 3 pixels.

The background for each of these spectra was subtracted using the normalized blank-sky backgrounds, as discussed in section 4.2.1.

These spectra were restricted to the energy range of 0.5 - 7.0 keV. The spectra for each region were then simultaneously fitted for all observations using Sherpa with the PHABS (APEC) model, where the hydrogen column density is fixed at $n_H = 3.0 \times 10^{20}$ cm^{-2} (Kalberla et al., 2005), the solar abundance is 0.3 $Z_\odot$, and the redshift is 0.34 and C statistics were applied.

Going clockwise, the panels in the top row of Figure 4.3 show the projected emission per unit area map (cm^{-5} $arcsec^{-2}$) and the projected temperature map (keV), the GGM image and the projected pseudo-pressure map respectively. The pseudo-pressure map is produced by multiplying the square root of the emission measure and temperature maps.

Each edge in this GGM image corresponds to a jump in temperature in the temperature map and a jump in pressure in the pseudo-pressure map. This makes them consistent with being shock fronts.

4.5 Shock Fronts

4.5.1 Surface Brightness Profiles

In Figure 4.1 and Figure 4.3, I observe sharp discontinuities in the surface brightness. In order to investigate these discontinuities, I extracted surface brightness profiles in the northwestern region covering the primary shock front and in the southeastern region covering the SE edge.

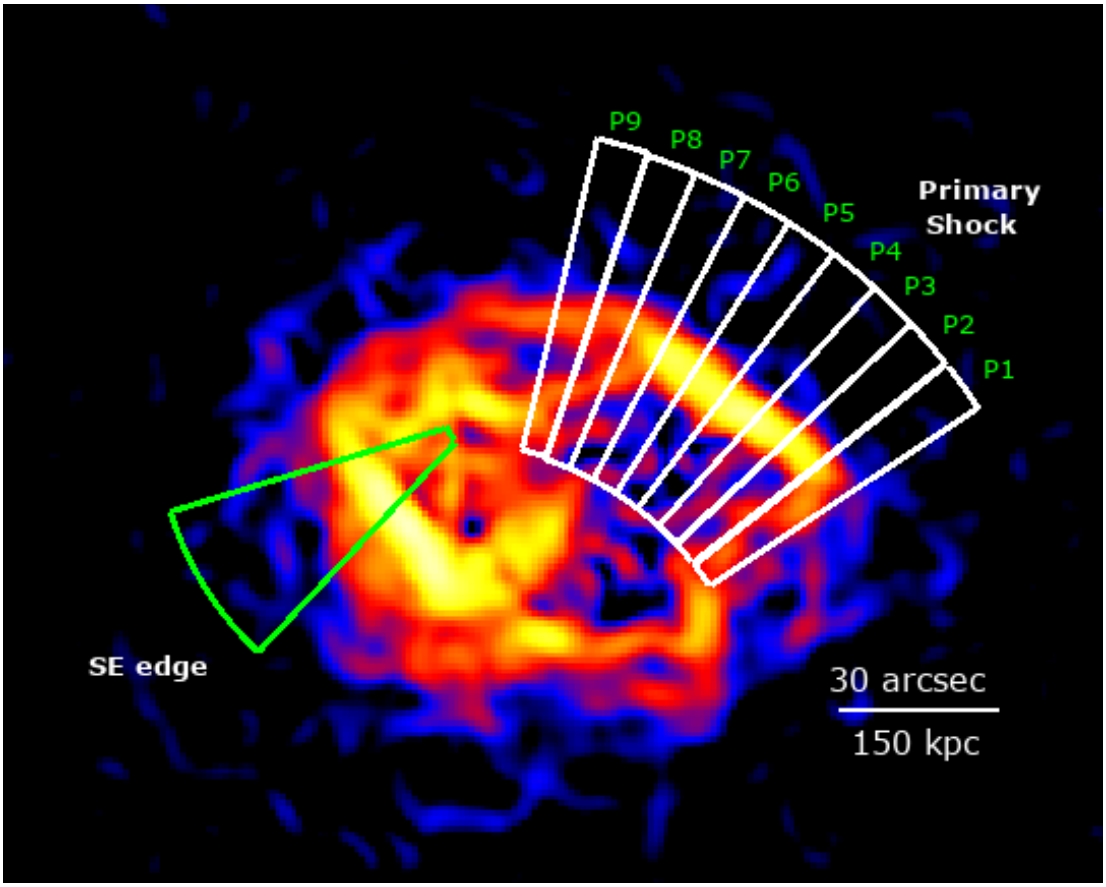

Figure 4.4: GGM image at scale = 3 pixels showing the sectors used to extract surface brightness profiles. The sectors in white are used to measure the density jump across the primary shock, and the one in green for the SE edge.

Surface brightness profiles were derived from multiple sectors covering the primary shock and from one sector covering the SE edge. Figure 4.4 shows the sectors selected for extracting these profiles. The sectors are chosen to cover the region where the shock fronts are well-defined based on the GGM image. Sectors $P1 - P9$ (where P refers to the primary shock) extend over the primary shock front. These sectors are centered so as to fully analyze the jump in surface

brightness. The outer radius for each sector was taken to be 5 arcmin (although the sectors in the image extend only up to $\sim$ 1.5 arcmin). Point sources were excluded from these sectors.

Once extracted, the surface brightness profiles were fitted with a broken power-law model projected along the line of sight (Markevitch and Vikhlinin, 2007) with the aim of identifying density discontinuities in the chosen sectors. Assuming spherical symmetry (following (Russell et al., 2012)), the density distribution can be given by:

$$n(r) = \begin{cases} n_0 \left(\frac{r}{r_{sh}}\right)^{\alpha_1}, & \text{if r} \leq \text{r}_{sh} \\ \frac{1}{C} n_0 \left(\frac{r}{r_{sh}}\right)^{\alpha_2}, & \text{if r} > \text{r}_{sh}, \end{cases} \tag{4.1}$$

where n_0 is the density normalization, α_1, and α_2 are the power-law indices, r_{sh} is the assumed shock location where the discontinuity in the surface brightness occurs. Also, $C = \rho_2/\rho_1$, where ρ_2 is the post-shock density and ρ_1 is the pre-shock density. At the location of the shock, ρ_2 is greater than ρ_1, (Mirakhor et al., 2023).

Using Rankine-Hugoniot jump conditions for the density jump, the Mach number for each sector can be calculated as follows:

$$M = \left[\frac{2\frac{\rho_2}{\rho_1}}{\gamma + 1 - (\frac{\rho_2}{\rho_1})(\gamma - 1)} \right]^{\frac{1}{2}}, \tag{4.2}$$

where ρ_2/ρ_1 is the density jump, and $\gamma = 5/3$ for a monoatomic gas (Russell et al., 2010).

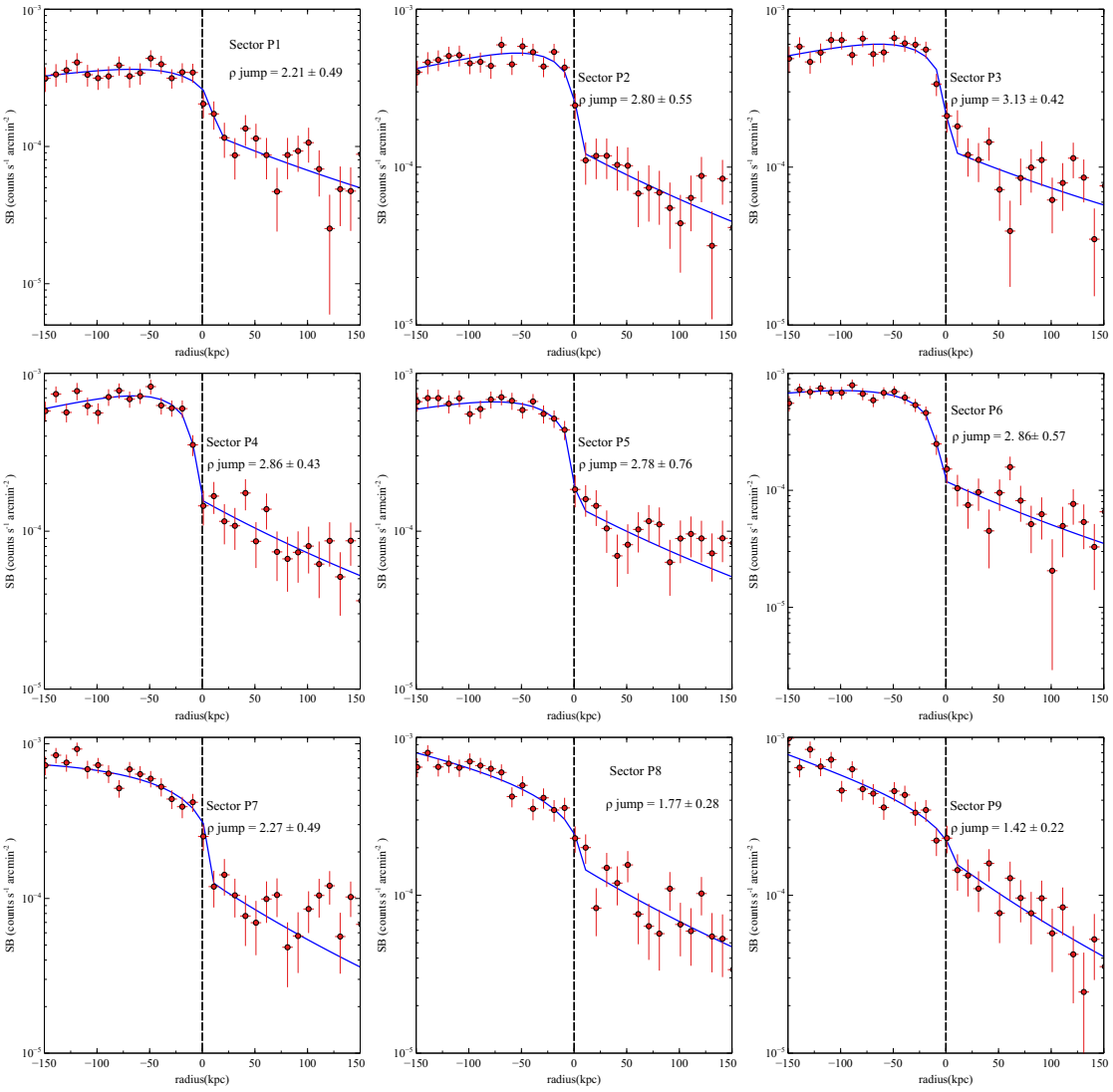

Figure 4.5: Surface brightness profiles in the $0.5 - 2.5keV$ energy band across sectors P1-9, each background subtracted and fitted with the broken power law density model (in blue).

In Figure 4.5, the red crosses in each panel show the surface brightness profile across sectors P1-P9. For each of these sectors, there is a sharp discontinuity in the surface brightness. The regions to the right of this jump are the

pre-shock regions, and the ones to the left, with the higher surface brightness, are the post-shock regions.

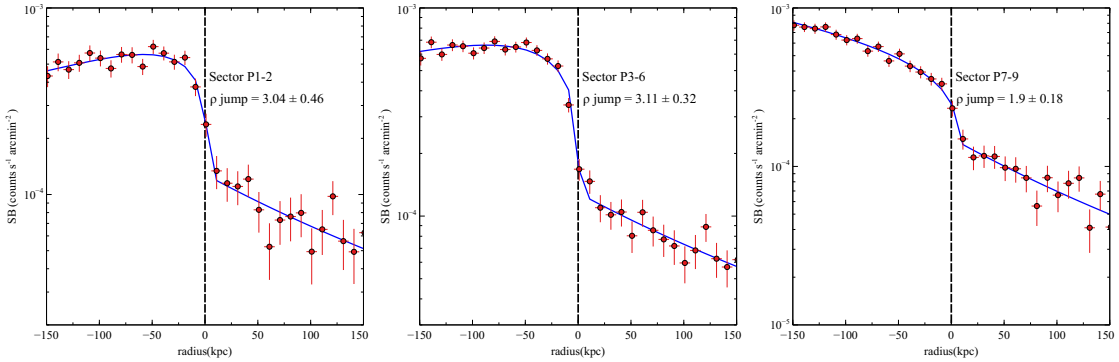

Figure 4.6: Surface brightness profiles across sectors P1-2 (left panel), P3-6 (center panel) and P7-9 (right panel) in the $0.5 - 2.5$ keV energy band. Each profile has been background-subtracted and fitted with the broken power law density model (in blue).

I have binned the sectors P1-2, P3-6, and P7-9 so that the sectors containing the part of the edge with the highest density jump (P3-6) are binned together. This binning allows us to better constrain the values of the density jumps and how the density jump varies along the shock front. Sector P3-6 is designed to cover the steepest part of the jump based on the GGM image, while regions P1-2 and P7-9 cover the regions to either side of the steepest jump. All three plots in Figure 4.6 show the surface brightness profiles over sectors P1-2, P3-6, and P7-9 fitted with the broken power law model in indicated by the solid blue line.

Table 4.2 shows the power law indices and density jump obtained from this fitting. The table shows these values for all the individual sectors P1-9, the binned sectors P1-2, P3-6, P7-9, and the SE edge.

Table 4.2: Details of the surface brightness fitting across the sectors along the primary shock front. The columns are, from left to right: sector label, density jump across that sector obtained by fitting with the broken power law density model, Mach number obtained from the density jump, the inner and outer slopes (power law indices in the broken power law model) and the reduced chi-squared of the fit.

Sector	Density Jump	M	Inner Slope	Outer slope	χ^2/ν
$P1$	2.21 ± 0.49	$1.92^{+0.53}_{-0.38}$	-1.80 ± 0.6	2.17 ± 0.61	19.62/25
$P2$	2.8 ± 0.55	$2.65^{+1.39}_{-0.83}$	-2.67 ± 0.65	2.35 ± 0.59	13.94/25
$P3$	3.13 ± 0.42	$3.28^{+1.38}_{-0.71}$	-2.33 ± 0.47	1.91 ± 0.25	39.14/40
$P4$	2.86 ± 0.43	$2.74^{+0.85}_{-0.55}$	-2.54 ± 0.55	2.38 ± 0.44	19.75/25
$P5$	2.78 ± 0.76	$2.61^{+1.39}_{-0.79}$	-1.89 ± 0.29	2.30 ± 1.01	14.28/25
$P6$	2.86 ± 0.57	$2.74^{+1.50}_{-0.73}$	-1.51 ± 0.44	2.60 ± 0.71	19.87/25
$P7$	2.27 ± 0.49	$1.98^{+0.54}_{-0.4}$	-3.32 ± 0.17	2.82 ± 1.04	24.82/25
$P8$	1.77 ± 0.28	$1.54^{+0.21}_{-0.19}$	0.52 ± 0.38	2.60 ± 0.52	23.32/25
$P9$	1.42 ± 0.22	$1.28^{+0.14}_{-0.14}$	0.93 ± 0.41	3.01 ± 0.51	22.23/25
$P1-2$	3.04 ± 0.46	$3.08^{+1.28}_{-0.7}$	-2.54 ± 0.39	2.07 ± 0.42	20.44/25
$P3-6$	3.11 ± 0.32	$3.23^{+0.89}_{-0.56}$	-1.62 ± 0.19	1.90 ± 0.26	22.60/25
$P7-9$	1.90 ± 0.18	$1.64^{+0.15}_{-0.13}$	0.52 ± 0.23	2.40 ± 0.30	16.86/25
SE edge	1.53 ± 0.14	$1.36^{+0.09}_{-0.08}$	-1.17 ± 0.43	1.45 ± 0.39	67.13/64

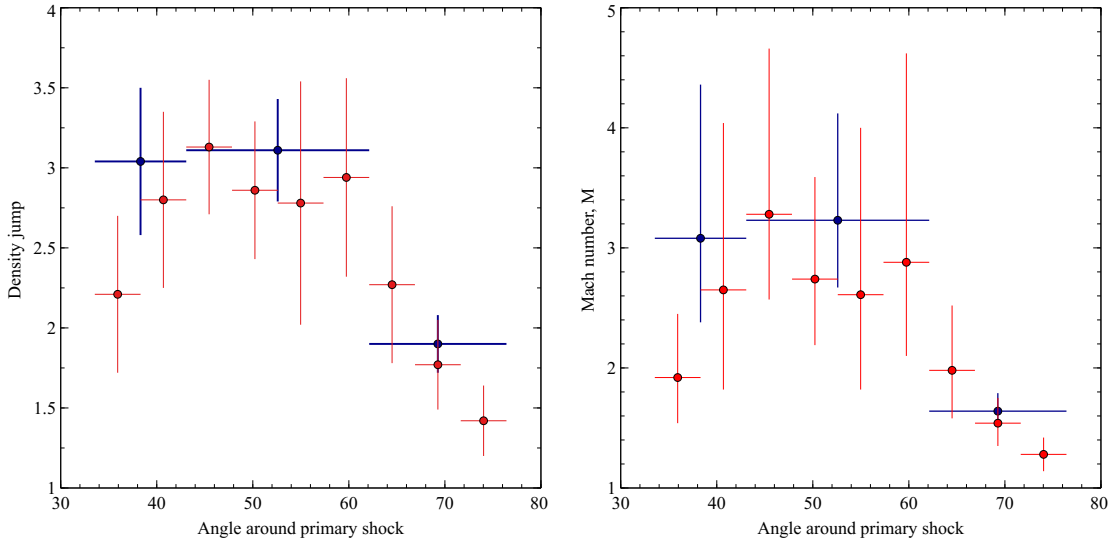

Figure 4.7: *Left:* The cross-bars in red depict the density jump across each of the sectors P1 - P9, and the ones in blue represent the density jumps in sectors P1-2, P3-6, and P7-9 from left to right. The x-axis represents the angle of the sectors around the primary shock front, going from 33° to 77°. *Right:* The Mach number, determined from the density jump, is shown here in red for the sectors P1-9 and for sectors P1-2, P3-6, and P7-9, shown in blue, across the angles of the sectors around the primary shock front.

The density jumps and Mach numbers along the Primary shock are plotted in Figure 4.7. The panel on the left shows the density jumps across the sectors plotted against the angle around the primary shock front, going from 33° to 77°. The red crosses indicate the density jump across each individual sector P1-9. The blue crosses represent the sectors binned as P1-2, P3-6, and P7-9. The panel on the right shows the Mach numbers derived from the corresponding density jumps using equation 1.37, also plotted against the angle around the primary shock front. The red crosses represent the Mach number derived for each of the sectors P1-9, and the blue crosses represent the binned sectors P1-2, P3-6, and P7-9.

In both plots, the observed trend is that the density jump and Mach number are highest at the center of the shock front, where the GGM image shows the highest gradient. On both sides of this center point, as the brightness of the GGM image decreases, the values of density jump and Mach number taper off, as expected from a similar analysis performed in Russell et al. (2022). The peak values of the density jump and Mach number are 3.11 ± 0.32 and $3.23^{+0.89}_{-0.56}$, respectively, for the binned sector P3-6, the brightest region in the GGM image. This makes the primary shock in SPT J2031 one of the strongest shocks when compared with the Bullet Cluster with $M = 3.0 \pm 0.4$ (Markevitch, 2006b), A2146 with $M = 2.3 \pm 0.2$ (Russell et al., 2010, 2012, 2022), A665 with $M = 3.0 \pm 0.6$ (Dasadia et al., 2016), A520 with $M = 2.4^{+0.4}_{-0.3}$ (Wang et al., 2018), and A98 with $M = 2.3 \pm 0.3$ (Sarkar et al., 2022).

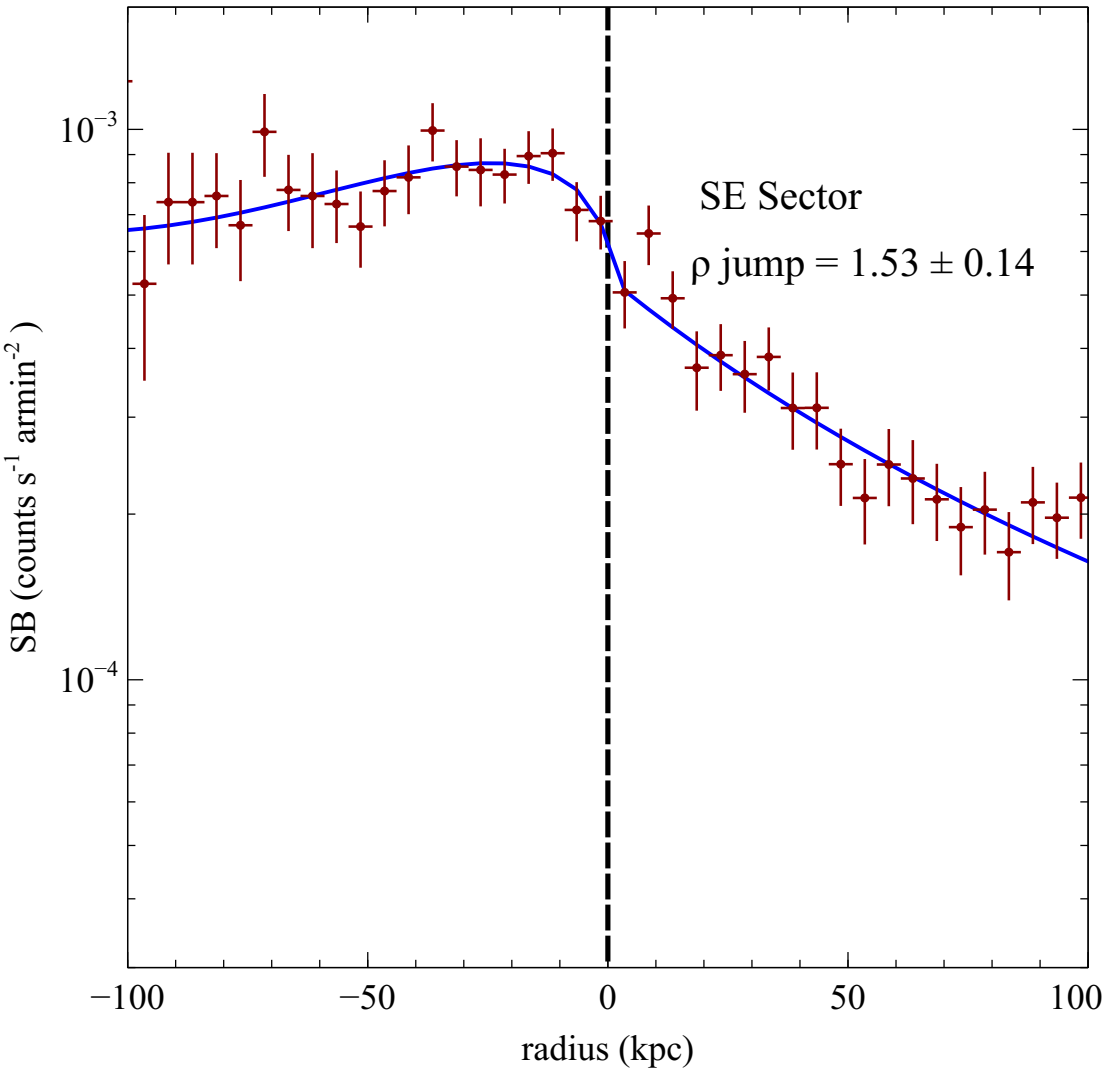

Figure 4.8: Surface brightness profile extracted in the $0.5 - 2.5keV$ energy band over the SE edge. The profiles were background subtracted and fitted with the broken power-law density model (solid blue line) to obtain a density jump of 1.53 ± 0.14, which corresponds to a Mach number of $1.36^{+0.09}_{-0.08}$. The dashed vertical line shows the shock location.

Figure 4.8 shows the surface brightness profile across the SE edge. The density jump across this edge is 1.53 ± 0.14, which corresponds to a Mach number

of $1.36^{+0.09}_{-0.08}$. The analysis of the trend in the density jump and Mach number was not possible for the SE edge, as that edge is not spatially extended enough, and it does not have a high enough density jump or corresponding Mach number.

4.5.2 Spectral Analysis of the Shock Fronts

The changes in temperature and density across the surface brightness edges can be observed more accurately by extracting radial profiles over the sectors shown in Figure 4.9.

The regions were selected so as to obtain the gas properties on both sides of each shock front. For the primary shock front, which has the higher density jump of the two, I extracted the temperature profile from the section of the shock with the highest density jump as determined in section 4.5.1 corresponding to sector P3-6. Using *specextract* in Sherpa, spectra were extracted from each of the regions for each of the ten observations.

These spectra were then analyzed in the energy range of $0.5-7.0$ keV. The background spectra used here were from the blank-sky backgrounds. The spectra for each region were then simultaneously fitted for all observations using Sherpa with the multiplicative PHABS(APEC) model, where the hydrogen column density is fixed at $n_H = 3.0 \times 10^{20}$ cm^{-2} (Kalberla et al., 2005), the solar abundance is 0.3 $Z_\odot$, and the redshift is 0.34 and chi-squared statistics were applied.

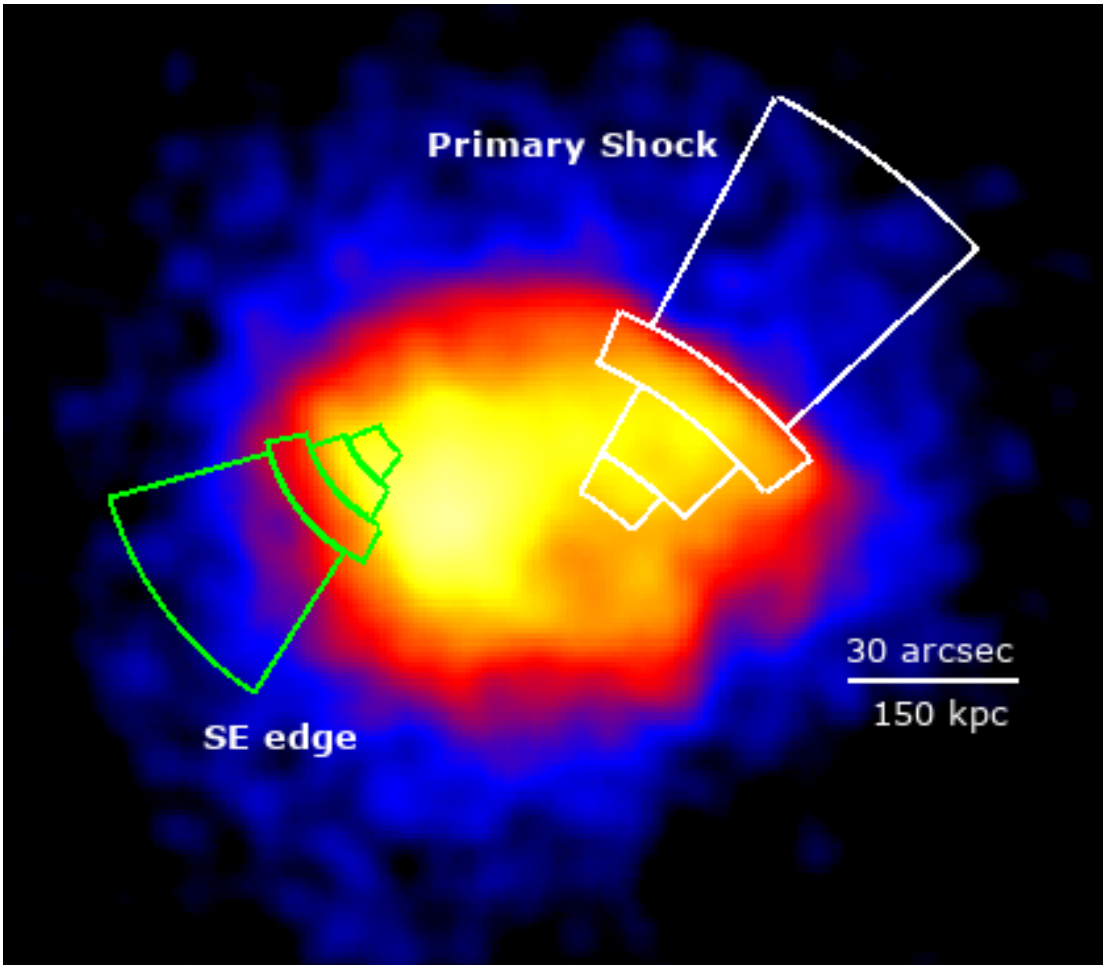

Figure 4.9: Exposure-corrected *Chandra* image of SPT-CLJ2031-4037 in the 0.5-2.5 keV energy range with the regions that were used to extract the temperature profiles across both the surface brightness edges.

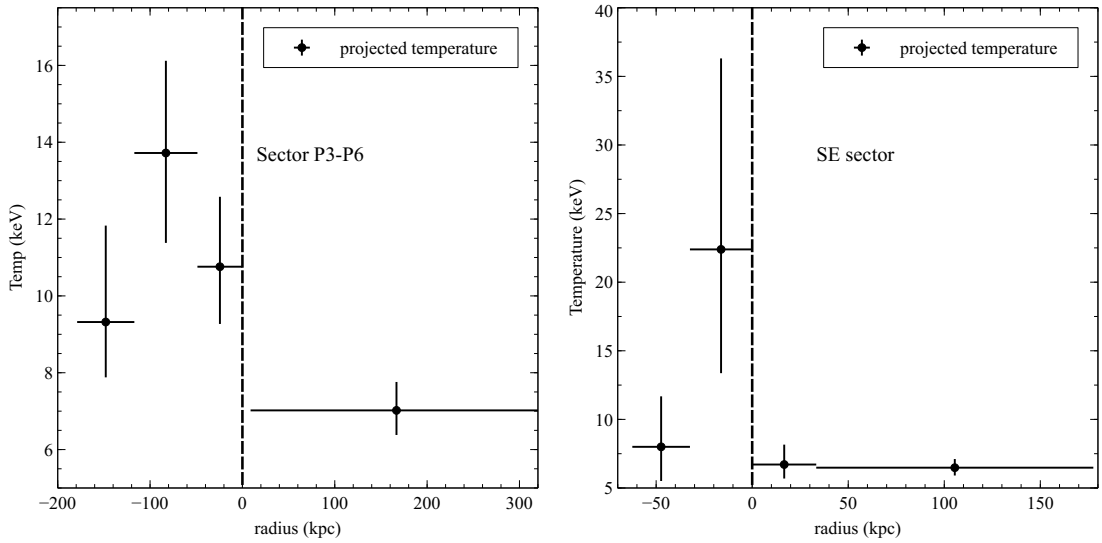

Figure 4.10: *Left:* The observed projected electron temperature profile over the primary shock front. I define the shock location to be at $r = 0$ kpc. *Right:* The figure shows the observed projected electron temperature profile across the SE edge. Again, I define the shock location to be at $r = 0$ kpc.

The resulting projected temperature profile for Primary shock is shown in the left panel of Figure 4.10. I see a significant temperature jump from about $7.0^{+0.7}_{-0.6}$ keV to $13.8^{+2.3}_{-1.8}$ keV. The projected temperature profile for the SE edge is shown in the right panel of Figure 4.10. I see a temperature jump from $6.48^{+0.63}_{-0.57}$ keV to $22.39^{+13.92}_{-9.02}$ keV. The gas in the pre-shock region of the primary shock has a temperature of $7.0^{+0.7}_{-0.6} keV$.

Along with the sharp increase in the surface brightness, there is an observed increase in the temperature in the post-shock region. The gas in this region has a temperature of $13.8^{+2.3}_{-1.8}$ keV. For the purpose of the fitting, the abundance is fixed at 0.3 $Z_{\odot}$.

Following Russell et al. (2012), I also obtained the values of the deprojected electron temperature using PROJCT in XSPEC. PROJCT is a deprojection routine that assumes spherical geometry for the cluster. This seems to be a reasonable assumption because the shocks in SPT J2031 appear to be approximately circular in the plane of the sky. The pre-shock electron temperature is $7.0^{+0.7}_{-0.6}$ keV, and the post-shock deprojected electron temperature is $17.3^{+5.41}_{-3.48}$ keV. This allows us to calculate the Mach number using the deprojected temperature jump.

I use the following Rankine-Hugoniot equation for obtaining the Mach number using the temperature jump:

$$M = \left[\frac{(\gamma+1)^2((\frac{T_2}{T_1})-1)}{2\gamma(\gamma-1)} \right]^{\frac{1}{2}}, \tag{4.3}$$

where T_2/T_1 is the temperature jump. The Mach number from the temperature jump using the values obtained from the deprojected electron temperature after using this equation is $2.13^{+0.4}_{-0.38}$. The Mach number obtained using the temperature jump is lower than that obtained from the density jump, which is similar to what is observed in Russell et al. (2012).

4.5.3 Electron-ion Equilibration

At present, major X-ray observatories like *Chandra*, *XMM-Newton*, and *NuSTAR* can directly measure the temperature of only the electrons in the ICM and not that of the ions. These electron temperature measurements are made using the continuum spectrum of the Bremsstrahlung produced from high-energy electrons. Cluster merger shock fronts affect electrons and ions differently and

thus provide a unique opportunity to determine the electron-ion equilibration timescale in the magnetized ICM. As the shock front passes through the ICM, it heats up the ions in the ICM gas immediately owing to their lesser thermal velocity and greater mass compared to the electrons (ZuHone and Su, 2022). This initially causes a significant increase in the ion temperature, which is not immediately observed in the electron temperature. Eventually, the electron temperature, which can be measured from the X-ray spectra, equilibrates with the ion temperature, but the method through which the heating occurs remains a matter of great debate (Wang et al., 2018). Presently, the two models that can possibly explain how the ICM gas is shock-heated are the instant shock-heating model and the adiabatic-collisional model.

According to the adiabatic-collisional heating model, protons and heavier ions are heated dissipatively, while electrons are compressed adiabatically to a temperature much lower than the ion temperature. This is explained by the fact that ions move at a velocity lower than the shock, whereas the electrons do not feel this shock (Markevitch and Vikhlinin, 2007), owing to them moving at a velocity higher than the shock. The higher velocity of the electrons is due to their mass, which is much lower compared to the mass of the ions. The temperature of these adiabatically compressed electrons is given by

$$T_{e,2} = T_{e,1}(\frac{\rho_2}{\rho_1})^{\gamma-1}, \tag{4.4}$$

where T_{e2} is the adiabatically compressed electron temperature; T_{e1} is the pre-shock electron temperature, $(\frac{\rho_2}{\rho_1})$ is the density jump, where ρ_1 and ρ_2 are the pre-

shock and post-shock densities, respectively, and γ is the ratio of specific heats for a monoatomic gas. The electrons eventually undergo Coulomb collisions and attain thermal equilibrium with the ions over a timescale (Sarazin, 1986) given by:

$$\tau_{eq}(e,p) = 6.2 \times 10^8 yr (\frac{n_e}{10^{-3}})^{-1} (\frac{T_e}{10^8 K})^{3/2}, \tag{4.5}$$

where n_e is the electron density, and T_e is the electron temperature.

The electron temperature gradually increases over this timescale, and the ion temperature decreases to reach the equilibrium temperature at a rate of:

$$\frac{dT_e}{dt} = \frac{T_i - T_e}{t_{eq}}, \tag{4.6}$$

where T_i is the ion temperature.

As the total kinetic energy density is conserved, the local mean gas temperature is given by:

$$T_{gas} = \frac{n_e T_e + n_i T_i}{n_e + n_i} = \frac{1.1 T_e + T_i}{2.1}, \tag{4.7}$$

where T_{gas} is constant with time.

The distance behind the shock where the equilibration is reached is obtained by multiplying Equation 4.5 for the time over which the equilibration is achieved with the post-shock velocity v_{ps}.

The pre-shock sound speed, derived from the equations $c_s = \sqrt{\gamma k_B T / m_H \mu}$ is $(1.3 \pm 0.06) \times 10^3$ km s^{-1}. The shock speed is obtained by multiplying the

Mach number (from the density jump, $M = 3.23^{+0.89}_{-0.56}$), and the sound speed is $v_{shock} \sim (4.4^{+0.27}_{-0.16}) \times 10^3$ km s^{-1}. The post-shock velocity v_{ps} for the primary shock front is 1414 km/s, obtained by dividing the shock speed by the density jump.

According to the instant heating model, the electrons are strongly heated at the shock front so that the electron temperature almost instantly reaches the post-shock temperature, equivalent to the ion temperature. This results in a timescale that is shorter than the Coulomb-collisional timescale, as the ICM is magnetized, making the plasma "collisionless." This phenomenon has been observed in studies of in-situ solar wind, which showed that the electron and proton temperature jump occurs on a linear scale of order several proton gyroradii, many orders of magnitude smaller than their collisional mean free path (Montgomery et al., 1970).

Although it is not possible to measure the temperature of the ions, it is possible to measure the jump in the gas density across the shock front (which I have done in section 4.5.1), which can be used to calculate the post-shock equilibrium temperature for the electrons and ions using the Rankine-Hugoniot jump conditions from the pre-shock temperature (Landau and Lifshitz, 1987). The temperature jump can be obtained using equation 4.8 (Markevitch and Vikhlinin, 2007):

$$\frac{T_2}{T_1} = \frac{\zeta - \rho_1/\rho_2}{\zeta - \rho_2/\rho_1}, \tag{4.8}$$

where I have assumed that $\gamma = 5/3$, the adiabatic index for monoatomic gas, and $\zeta \equiv (\gamma+1)/(\gamma-1)$, and the indices 1 and 2 denote the pre-shock and post-shock quantities, respectively.

Following Wang et al. (2018) and using the best-fit density model, I projected the 3D temperature model profile onto the sky using the spectroscopic-like temperature weighting $w = n^2 T^{-3/4}$, which allows us to compare the projected temperature model with the observed projected temperature profile. I did this for both the instant heating model and the collisional equilibration model as can be seen in Figure 4.11.

The right-hand panel of Figure 4.11 shows how the electron temperatures observed across the primary shock front compare with the collisional and instant heating models projected along the line of sight. The observed post-shock temperature for the primary shock front seems to favor the Collisional model over the instant heating model.

In the case of the Bullet Cluster, Markevitch (2006b) found that the observed temperature profile supports the instant equilibration model, suggesting that electrons at the shock front were heated on a timescale faster than the Coulomb collisional timescale. However, the post-shock temperature in the Bullet cluster is $\sim 20-40$ keV, which is much higher than the energy pass band of *Chandra*, thus making it difficult to constrain. The post-shock electron temperature in SPT J2031 is lower than that of the Bullet Cluster, making the measurements of the post-shock temperature more accurate. In contrast, an analysis of the shock in the Bullet Cluster by ALMA and ACA (Di Mascolo et al., 2019) found that

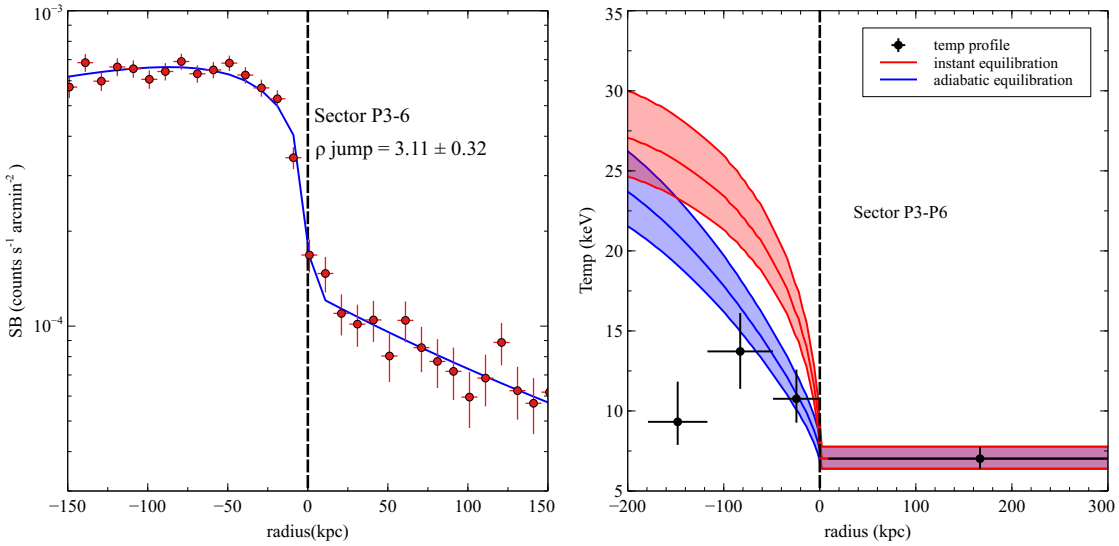

Figure 4.11: *Left:* Surface brightness profiles extracted over sectors $P\ 3-6$ in the $0.5-2.5keV$ energy band. The profiles are background-subtracted and have been fitted with the broken power-law gas density model (in solid blue). The density jump observed over this sector is 3.31 ± 0.32, and the Mach number resulting from this density jump is $3.23^{+0.89}_{-0.56}$. *Right:* Projected electron temperatures (in black) observed across the sectors $P\ 3-6$ of the primary shock front compared with the overlaid adiabatic-collisional (in blue) and instant heating models (in red) projected (up to 1σ error bands) along the line of sight for electron-ion equilibration. The post-shock temperature for the primary shock front seemingly favors the Adiabatic-collisional model over the instant heating model.

the assumption of an adiabatic temperature jump in the electron temperature results in the best agreement between results of Sunyaev-Zeldovich and X-ray measurements.

For the merger shock front in A2146, Russell et al. (2012) found that the temperature profile across the bow shock is consistent with the collisional equilibration model, whereas the upstream shock favors the instant equilibrational model. However, the uncertainty in the measurement for the upstream shock was higher because of its lower Mach number and hence was not determined to be

the definite conclusion. Subsequently, with deeper 2 Ms *Chandra* observations of A2146, Russell et al. (2022) found that both the shock fronts support the collisional equilibration model. Our results for the primary shock in SPT J2031 agree with Russell et al. (2012, 2022) in that the observed post-shock electron temperature favors the Collisional equilibration model.

Analysis of the merger shock front in A520 (Wang et al., 2018) found that the post-shock electron temperature was higher than expected in a situation where the electrons undergo adiabatic compression followed by Coulomb collisions. Hence, like the Bullet Cluster, the electron temperature profile in A520 also supports the instant equilibration model with a confidence level of 95%.

A similar comparison of the post-shock electron temperature in the merger shock of A98 (Sarkar et al., 2022) with the Collisional and instant equilibrational model showed that the observed post-shock electron temperature favors the instant equilibration model; however, the large uncertainties in the temperature indicate that the Collisional model cannot be ruled out.

4.6 Conclusions

I conducted a comprehensive analysis of our newly acquired deep (256 ks) *Chandra* observations of the merging system SPT-CLJ2031-4037 and obtained the following results:

- SPT J2031 exhibits merger geometry, as suggested by an offset between the brightest X-ray peaks in the exposure-corrected image from the *Chandra*

observations and the two Brightest Cluster Galaxies in the HST optical image.

- I have utilized the GGM filtering technique to identify two sharp surface brightness edges in SPT J2031, the primary shock front and the southeastern edge.

- I extracted surface brightness profiles across both the edges identified in the GGM image and fitted them with the broken power-law model to find the density jump across the shock front. The sharp edge in the northwest direction is the primary shock with a density jump $\rho = 3.11 \pm 0.32$ corresponding to a Mach number of $3.23^{+0.89}_{-0.56}$.

- Due to the high Mach number obtained from the density jump in the primary shock front, I were able to compare the observed electron temperature profile of the primary shock with the collisional equilibration model and the instant shock heating model. I found that the post-shock electron temperature is lower than the temperature predicted for the instant shock heating model and favors the collisional equilibrational model. These findings are similar to the result in (Russell et al., 2012, 2022). However, I cannot completely rule out the instant heating model.

- The other surface brightness edge, the SE edge, is observed in the southeastern direction and also appears to be a shock front. It has a density jump $\rho = 1.47 \pm 0.26$ corresponding to a Mach number $M = 1.31^{+0.17}_{-0.16}$. Since the Mach number $M < 2$, I were not able to achieve enough separation between

the two projected models of heating to compare with the observed electron temperature profile.

- I plotted the density jump and Mach number of the primary shock as a function of the angle around the shock front and found that the density jump, and subsequently the Mach number peak at the center of the shock front, where the gradient in the GGM image is maximum. Both the density jump and the Mach number taper off with a change in angle on both sides of this center point.

Chapter 5. Possible Non-Thermal Origin of the Hard X-ray Emission in the Merging Galaxy Cluster SPT-CLJ2031-4037

This chapter consists of a brief discussion on synchrotron radiation and its occurrence in merging galaxy clusters, followed by the discussion about the source of such radiation - relativistic electrons, their acceleration mechanism, and how they cause inverse Compton scattering. The final section of this chapter details the attempt to search SPT J2031 for possible non-thermal emission using NuSTAR data.

5.1 Synchrotron Radiation

Synchrotron radiation refers to the electromagnetic radiation emitted by charged particles, typically electrons, as they are accelerated in a curved path or orbit by a magnetic field (as shown in Fig. 5.1). Synchrotron radiation plays a crucial role in understanding the physical processes occurring in galaxy clusters. Observations of galaxy clusters have revealed the presence of synchrotron radiation, such as the detection of extended radio emissions in the form of radio halos and relics. These extended radio sources indicate the existence of relativistic particles and magnetic fields within the ICM (Brunetti and Jones, 2014).

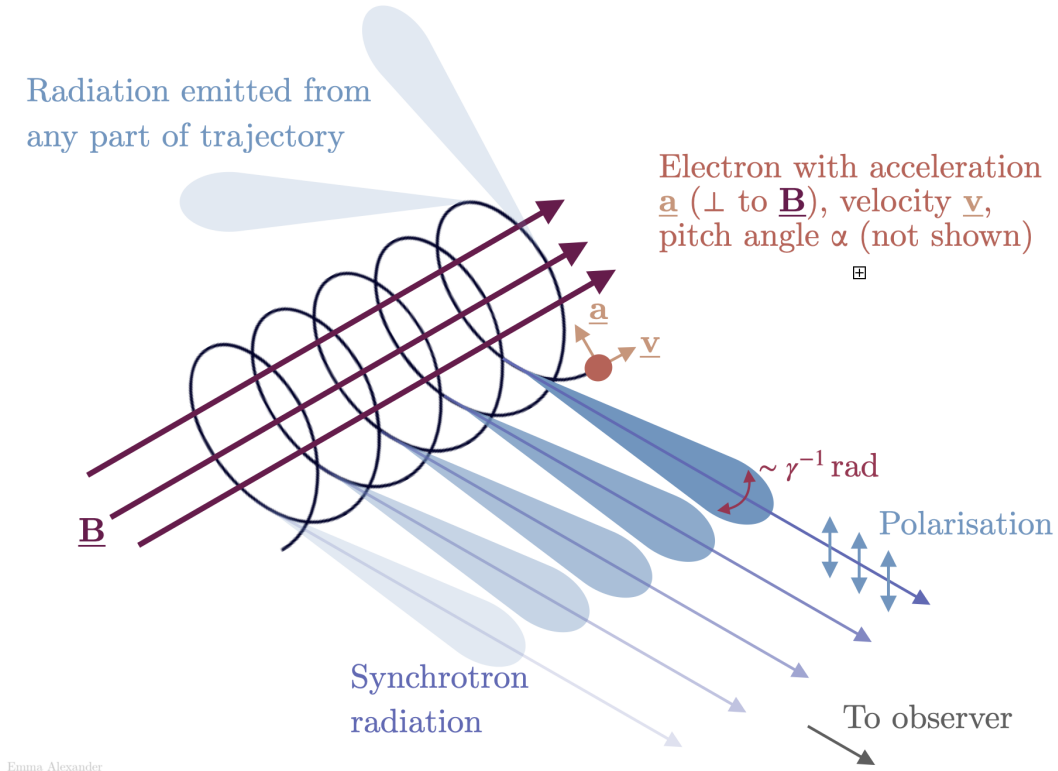

Figure 5.1: Synchrotron radiation is emitted due to an electron moving in a helical path around a magnetic field. The acceleration of the electron is perpendicular to the magnetic field, B, and perpendicular to $v_\perp$, the component of velocity v perpendicular to the magnetic field. This image was sourced from Creative Commons. The creator is Emma L. Alexander, and the image can be found here.

Studying these non-thermal components provides important information about the dynamics and evolution of galaxy clusters.

In a uniform magnetic field, a high-energy electron moves in a spiral path at a constant pitch angle α. The pitch angle is the angle between the direction of the magnetic field B and velocity, v. The velocity has a component along the field line, $v_{||}$, and a component perpendicular to the field line,$v_{\perp}$. Here, $v_{||}$ is constant. The acceleration of the electron perpendicular to the magnetic field direction, B, and to $v_{\perp}$ is (Longair, 2011) :

$$a_{\perp} = \frac{evBsin\alpha}{\gamma m_e}. \tag{5.1}$$

The total radiation loss rate of the electron is (Longair, 2011):

$$-\left(\frac{dE}{dt}\right) = \frac{\gamma^4 e^2}{6\pi\epsilon_0 c^3}\left|a_{\perp}\right|^2, \tag{5.2}$$

$$= \frac{\gamma^4 e^2}{6\pi\epsilon_0 c^3}\frac{e^2 v^2 B^2 sin^2\alpha}{\gamma^2 m_e^2} \text{ and} \tag{5.3}$$

$$= \frac{e^4 B^2}{6\pi\epsilon_0 c m_e^2}\frac{v^2}{c^2}\gamma^2 sin^2\alpha, \tag{5.4}$$

where γ is the Lorentz factor, defined as:

$$\gamma = \frac{1}{\sqrt{1-\frac{v^2}{c^2}}}. \tag{5.5}$$

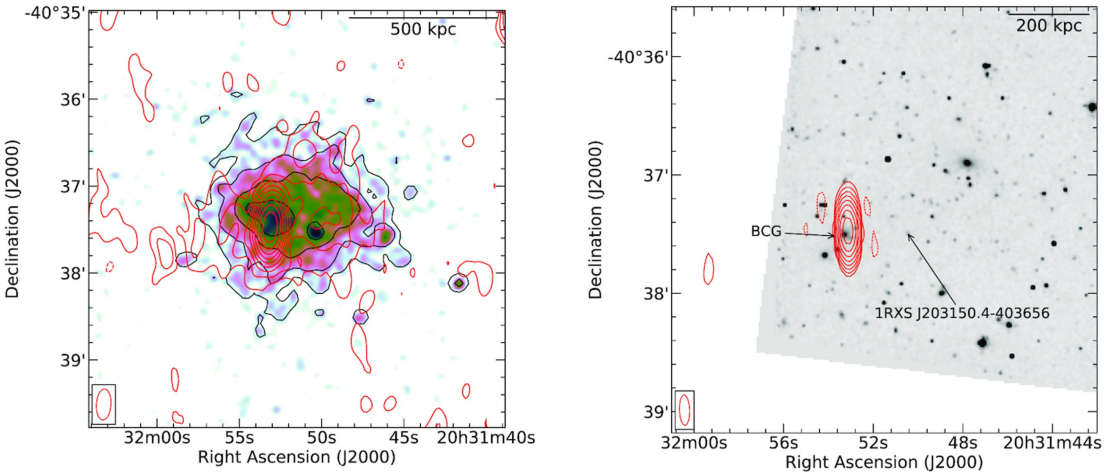

Figure 5.2: *Left:* Contours (in red) are from the observation of the radio halo using the *GMRT* (Giant Metrewave Radio Telescope) at 325 MHz overlaid onto the *Chandra* image of SPT J2031. The black lines are X-ray contours spaced by a factor of 2. *Right:* HST optical image of SPT J2031 overlaid with the radio contours at 325 MHz in red.

Thus, equation 5.4 implies that the total radiation output is proportional to the square of the magnetic field. Hence, the stronger the magnetic field, the more synchrotron radiation is observed. The total radiation output is also proportional to γ squared, which is the Lorentz factor of the electron (see Equation 5.5). Based on this equation, it is evident that the electrons need to be moving very close to the speed of light. Hence, the electrons must be highly relativistic for synchrotron radiation.

5.2 Radio Halos in Merging Galaxy Clusters

Radio halos are typically observed in galaxy clusters undergoing mergers or interactions, where energetic processes can accelerate electrons to high energies. These high-energy electrons emit synchrotron radiation as they spiral around

magnetic field lines, producing the radio emission (Feretti et al., 2012). The term halo refers to the fact that the emission is spread out around the central region of the cluster. In the cluster SPT J2031, Raja et al. (2020) finds a radio halo shown in Fig. 5.2. The panel on the left shows the contours (in red) obtained from the *GMRT* (Giant Metrewave Radio Telescope) at 325 MHz overlaid on the *Chandra* image of SPT J2031. The panel on the right shows the HST optical image of SPT J2031 overlaid with the radio data in red contours at 325 MHz.

5.3 Relativistic Electrons and Their Acceleration Mechanisms

So far, I have discussed electron temperatures obtained via Bremsstrahlung radiation. In the case of the SPT J2031 cluster discussed in Chapter 4, the post-shock electron temperature is measured to be 13.8 keV. This post-shock temperature can be used to calculate the speed of the electrons with the following equation for an ideal gas:

$$v = \sqrt{\frac{3kT}{m}}, \tag{5.6}$$

where k = Boltzmann's constant, T = temperature of the electron, and m is the mass of the electron. Converting this kinetic energy into speed, I obtain the speed of the electrons to be $\approx 85,000$ km s^{-1}, which is much smaller than the speed of light (300,000 km s^{-1}). Hence, these electrons are not the source of the observed synchrotron radiation. This implies that some other source of these highly accelerated electrons is responsible for the synchrotron radiation.

Particle acceleration is a process through which a relatively small number of particles in the higher-energy tail of the thermal distribution gain a large

Figure 5.3: (a) A parallel shock front in a stationary frame of reference. (b) A schematic diagram showing the motion of particles in the vicinity of the shock. The plasma flow speeds are u_1 (upstream) and u_2 (downstream). (Bell, 1978)

amount of energy and thus result in an overall non-thermal distribution. The final energies of the tail particles are far in excess of the thermal energy. Particle acceleration in astrophysical environments encompasses a wide range of mechanisms and processes. Based on a review of Jokipii (1979), particle accelerations are categorized as deterministic and stochastic. Deterministic acceleration mechanisms, such as diffusive shock acceleration (DSA) and first-order Fermi acceleration, involve systematic and predictable processes where particles gain energy through interactions with shocks or magnetic fields. Stochastic acceleration mechanisms, conversely, involve random interactions with turbulent or fluctuating fields, leading to the random and diffusive energization of particles (Bian et al., 2012).

In galaxy clusters, the mechanism through which electrons are accelerated to relativistic speeds to produce synchrotron radiation is primarily driven by shocks in the ICM (Feretti et al., 2012). Galaxy clusters form through the merger of smaller clusters and groups, resulting in the generation of shocks during the

merging process. These shocks can accelerate particles, including electrons, to relativistic energies through a process known as diffusive shock acceleration (DSA) (Weeren et al., 2010).

5.3.1 Diffusive Shock Acceleration Mechanism:

Diffusive shock acceleration (DSA) is a subset of the first-order Fermi acceleration. First-order Fermi acceleration is a general concept that encompasses various acceleration mechanisms. It can occur in different kinds of astrophysical environments, which include shock regions, magnetic reconnection regions, and turbulence (Drury, 2012; Petrosian, 2012). DSA is a specific type of first-order Fermi acceleration mainly associated with shock fronts (Botteon et al., 2020). It is primarily observed in environments like the sites of cosmic ray production and at several sites in the heliosphere (Baring, 1997).

In the DSA process, particles are accelerated diffusively at the shock. The particles cross back and forth across the shock front in the downstream and upstream regions of the shock due to magnetic inhomogeneities in these regions (van Weeren et al., 2019). Every time the particle crosses the shock, it gains additional energy, resulting in a non-thermal distribution.

This mechanism is observed in parallel shocks (fig. 5.3a), with its direction of propagation along the magnetic field lines, and considers only those particles (electrons or protons) that have energies high enough for their gyroradii to be much larger than the width of the shock front (Bell, 1978), where the shock front

width is considered to be less than, or of the order of the gyroradius of a thermal proton (Boyd and Sanderson, 1969).

Consider a flow of particles defined by speeds u_1 and $u_2(< u_1)$ on different sides of the shock (see Fig 5.3b). Particles on the upstream side of the shock (u_1) diffuse around via collisions with magnetic turbulence until they eventually cross over the shock to the downstream side (u_2) of the plasma. This causes an increase in the average particle speed in the rest frame of the shock. Some of these particles return to the upstream side of the shock, and the process repeats, leading to average particle speeds that are higher than the speeds reached in the downstream plasma. This sequential process of back-and-forth diffusion across the shock continues to increase the particle speed, thereby accelerating the particles (Baring, 1997). When a similar process happens in the opposite direction, where the particle travels from downstream to upstream and is reflected from the upstream back into downstream, it increases the average energy of the particles. The subsequent reflections of multiple particles give a resultant energy spectrum, which turns out to be the power law given by the equation (5.7):

$$\frac{dN(\epsilon)}{d\epsilon} \propto \epsilon^{-p}, \tag{5.7}$$

where the spectral index $p \geq 2$ depends on the compression ratio of the shocks for non-relativistic shocks.

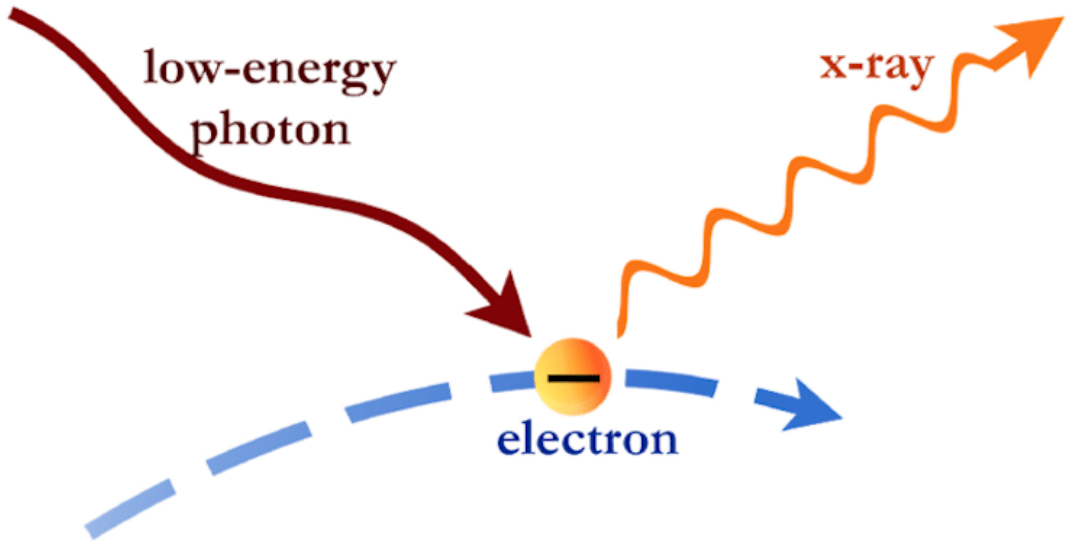

Figure 5.4: Inverse Compton scattering for a single electron due to a low-energy photon. A high-energy, relativistic electron interacts with a low-energy photon. In this interaction, the electron transfers some of its energy to the photon, making it an X-ray photon and scattering it from its path.

5.4 Inverse Compton Emission from Hard X-rays

In principle, the relativistic electrons responsible for synchrotron radiation can also cause inverse Compton scattering. Inverse Compton (IC) scattering is a process in which a charged particle, typically an electron, transfers part of its energy to a photon, resulting in an increase in the energy of the photon, as well as causing it to scatter. When an electron with exceptionally high energy (as depicted in Fig. 5.4) encounters a photon with very low energy, it can undergo IC scattering. These low-energy photons originate from the Cosmic Microwave Background (CMB) and are present everywhere throughout the universe. Since these are microwave photons, their energy is exceedingly low. However, it is possible that some of the electron's energy could be transferred to the photon through inverse scattering, causing it to transform from a microwave photon into an X-ray photon. Consequently, the presence of these high-energy electrons can also be inferred by observing X-ray emissions, which result from inverse Compton scattering rather than Bremsstrahlung.

Fig. 5.5 shows the plot of the photon flux against the photon energy in keV of the expected spectrum for a galaxy cluster which has bremsstrahlung component from the ICM and IC emission from the ICM. The overall spectrum consists of two components: a thermal component originating from Bremsstrahlung and a non-thermal component resulting from IC scattering.

Since the sensitivity range of Chandra is 0.7 – 7.0 keV, it is not possible to measure anything beyond this energy using Chandra. The NuSTAR telescope is

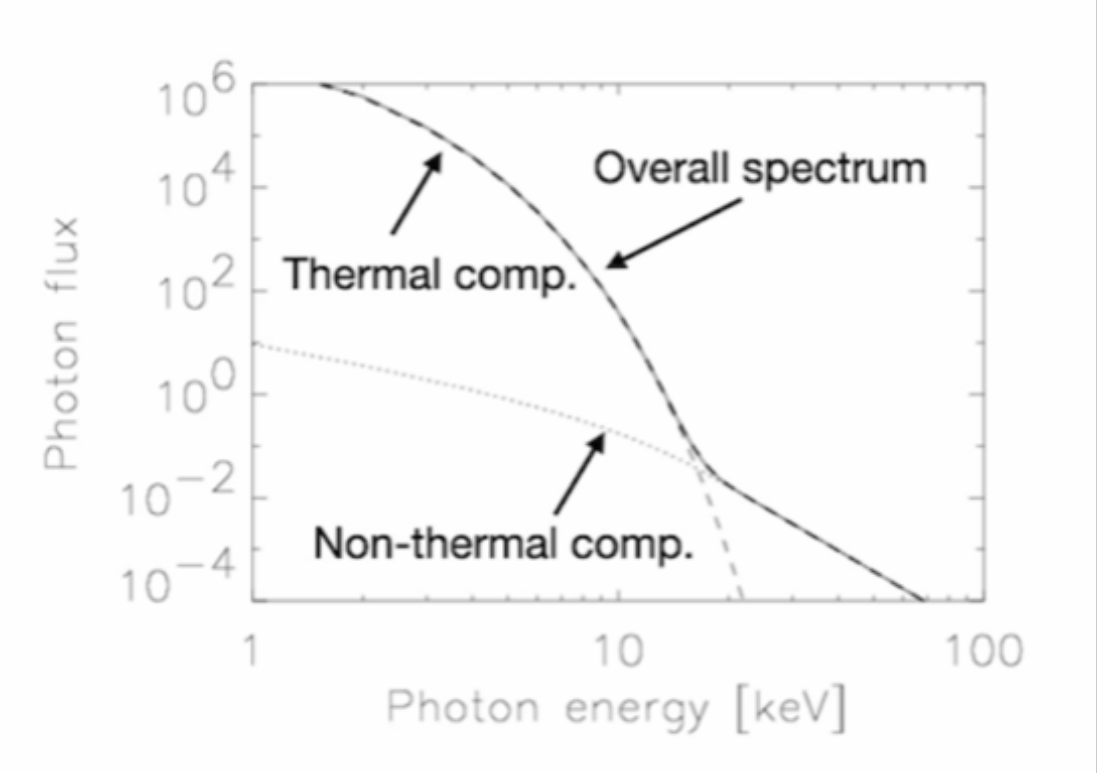

Figure 5.5: The plot of the photon flux against the photon energy in keV of the expected spectrum for a galaxy cluster that has a bremsstrahlung (thermal) component from the ICM and IC emission (non-thermal) from the ICM. The non-thermal component only dominates over the thermal component at high energies.

employed to measure the emission at high X-ray energies (hard X-ray emission). The sensitivity of NuSTAR lies between 3 keV and 80 keV, making it the ideal telescope to observe the non-thermal component. Consequently, Chandra data is used to constrain and accurately model the thermal component, while NuSTAR allows for the measurement of the high-energy tail of this spectrum.

5.5 Discovery of Radio Halo in SPT-CL J2031-4037

Raja et al. (2020) discuss their discovery of a radio halo surrounding the central brightest cluster galaxy in the galaxy cluster SPT J2031. The paper finds that SPT J2031 is a morphologically disturbed cluster yet has a weak cool core, an example of a cool-core/non-cool-core transition system, which harbors a radio halo ~ 0.7 Mpc in size (see Fig. 5.2).

Analysis of deep *Chandra* data of SPT J2031 shown in Chapter 4 indicates that it is indeed a cluster that has undergone a merging event. However, the band-pass of *Chandra* is $0.7 - 7$ keV. To study SPT J2031 for the presence of non-thermal emission, I helped write a NuSTAR and successfully obtained the data, which has been analyzed in the following sections.

5.6 *NuSTAR* Observation of SPT J2031

SPT J2031 was observed by *NuSTAR* using both of its telescopes, FPMA (Focal Plane Module A) and FPMB (Focal Plane Module B), for a total of 238 ks spread over two observations (PI: Walker). The first observation was performed on December 4, 2020, for a total unfiltered exposure time of 145.4 ks, and the second observation was performed on May 27, 2021, for a total unfiltered exposure time of 92.8 ks. Table 5.1 gives the details of the observations used for the analysis in this work.

Table 5.1: Details of the *NuSTAR* observations of SPT J2031

Obs. ID	RA	Dec	Obs. date	Unfiltered / Filtered exp (ks)	
				FPMA	FPMB
70601001001	20 31 30.6	-40 39 32.0	2020-12-04	145.4 / 123.5	145.4 / 123.8
70601001003	20 32 01.4	-40 34 36.0	2021-05-27	92.8 / 75.9	92.8 / 71.7

Data reduction processes were performed on these observations using standard pipeline processing. The data reduction, pre-processing, and analysis process was done using HEASoft (High Energy Astrophysics SOFTware) v6.29 and Nustardas (NuSTAR Data Analysis Software) v2.1.1. The *nupipeline* script was used to produce clean event files, which were further used to extract images, light curves, and spectra using the *nuproducts* script. Fig. 5.6 shows the light curves for the observation 70601001001. The top and bottom panels show the light curves for the FPMA and FPMB telescopes, respectively. A visual assessment of these light curves did not show any significant fluctuations.

Fig. 5.7 shows the background-subtracted global spectra of the observation 700601001001. The two upper curves in black and red represent the spectra

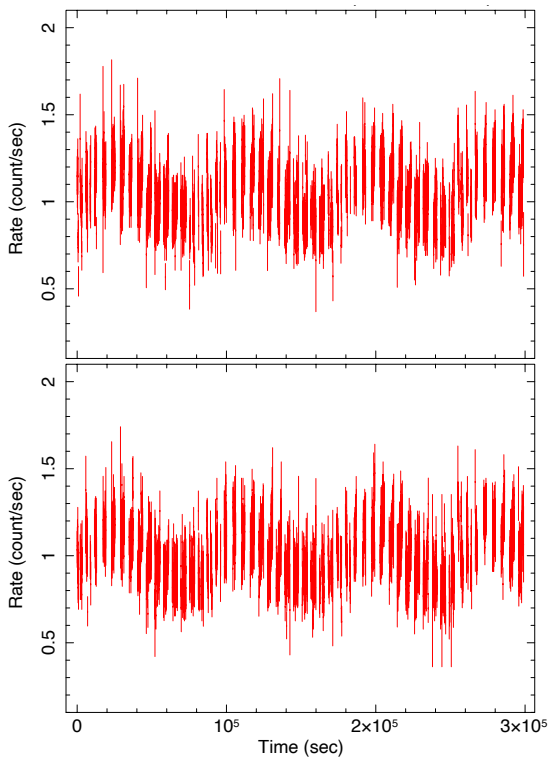

Figure 5.6: Light curves for the observation 70601001001. The top and bottom panels show the light curves for the FPMA and FPMB telescopes, respectively. The light curves do not show significant fluctuations.

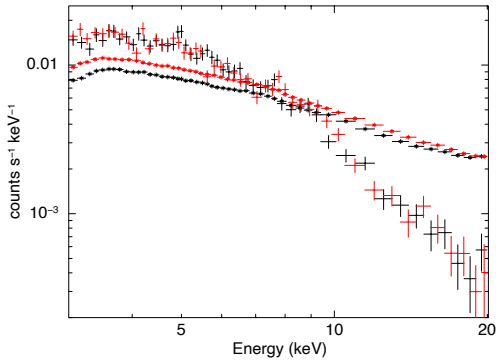

Figure 5.7: Background-subtracted global spectra of the observation 700601001001. The two upper curves in black and red represent the spectra from the FPMA and FPMB telescopes, respectively. The lower curves represent the background spectra. As seen in the figure, beyond 10 keV, the spectra are background-dominated.

from the FPMA and FPMB telescopes, respectively. The lower curves represent the background spectra. As seen in the figure, beyond 10 keV, the spectra are background-dominated.

5.7 Image Analysis

Figure 5.8 shows the mosaic of the exposure-corrected, background-subtracted images of the cluster in three energy bands. From left to right, the energy bands in the panels are $3-10$ keV, $10-20$ keV, and $20-50$ keV, respectively. The circle in solid white with a 5 arcmin radius marks the region from which the source spectra were extracted. The dashed circles mark the regions from which the background spectra were extracted. The $3-10$ keV and the $10-20$ keV images show the distribution of hot gas from the cluster. However, the $20-50$ keV image appears to be completely background-dominated as it does

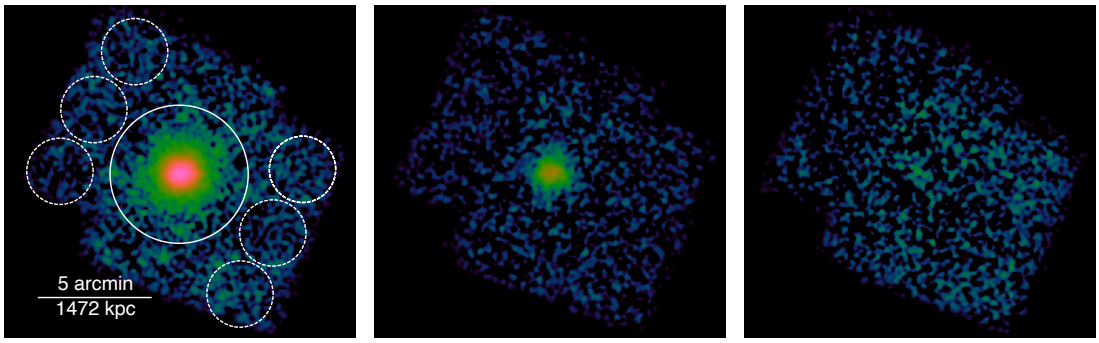

Figure 5.8: Background-subtracted and exposure-corrected images of the galaxy cluster SPT J2031, obtained by combining both observations from both telescopes. *Left:* The energy band is 3–10 keV. The circle in solid white with a 5 arcmin radius marks the region from which the source spectra were extracted. The dashed circles mark the regions from which the background spectra were extracted. *Middle:* The exposure-corrected image obtained in the 10–20 keV energy band. *Right:* The exposure-corrected image obtained in the 20–50 keV energy band.

not exhibit any evidence of cluster emission. Point sources found in the $3-10$ keV image have been excluded from further analysis; no point sources were found in the other two images.

5.8 Spectral Analysis

The global spectrum of SPT J2031 was extracted from the solid white circle of radius 5 arcmin, shown in the left panel of Fig. 5.8. The spectral data obtained from both the observations and both the telescopes were simultaneously fitted to three different models to find a model that provides a good fit to the data from the entire spectrum. These models are the single-temperature (1T) model, a two-temperature (2T) model, and a single-temperature plus power-law (1T+IC) model.

5.8.1 Fitting with a 1T Model

The 1T model consists of an APEC thermal component (Smith et al., 2001) with Galactic absorption fixed at $N_H = 3.21 \times 10^{20}\text{cm}^{-2}$ and redshift $z = 0.3416$. The spectral fitting was performed in the $3 - 20$ keV energy band using XSPEC (Arnaud, 1996). The best-fit values were obtained by using C-statistic (C-stat), as shown in Table 5.2. The best-fit yields a temperature value of $T = 9.2^{+0.4}_{-0.3}$ keV and a metal abundance of $Z = 0.03^{+0.02}_{-0.02} Z_{\odot}$. The C-stat value associated with the 1T model fit is 1903.1 with 1693 degrees of freedom. Fig. 5.9 shows a 1T model fit to the global spectra data. As seen in the figure, a notable amount of excess is seen in the energy range of $10 - 20$ keV.

The 1T (one temperature) model will likely be an unrealistic description of the spectral data for morphologically disturbed galaxy clusters such as SPT J2031. A more plausible explanation of the spectral data may be obtained by fitting the spectral data with a two-temperature (2T) model.

5.8.2 Fitting with a 2T Model

The 2T model consists of two thermal APEC components with their metal abundances tied together. The best-fit values of the temperatures obtained by fitting the spectra in the $3 - 20$ keV to the 2T model are $T_1 = 2.4^{+1.7}_{-0.5}$keV and $T_2 = 18.3^{13,7}_{-2.2}$keV. The metal abundance is $Z = 0.10^{+0.05}_{-0.05} Z_{\odot}$. The C-stat value associated with the 2T model is 1774.8 with 1691 degrees of freedom. Thus, the 2T model is a better fit for the spectral data than the 1T model.

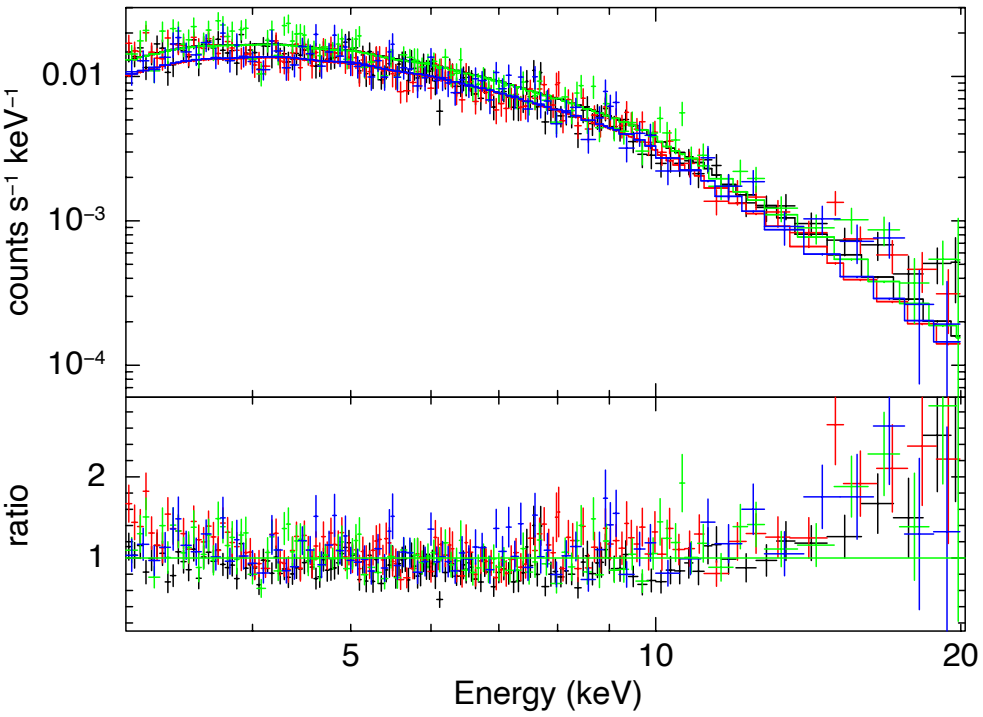

Figure 5.9: Background subtracted spectra in the $3 - 20$ keV energy range for both the observations of the cluster SPT J2031 from both the telescopes. The figure shows the spectral data fitted to the 1T model. While the model fits the data well in 3-10 keV, a significant excess is seen in the 10-20 keV energy range.

The best-fit temperature values obtained in the 2T temperature model are an order of magnitude apart and are poorly constrained. These temperature values are also lower than the temperature measured by *Chandra*. Moreover, they lie outside the band-pass of the $3 - 20$ keV energy band. This led to a different approach to fit the spectral data in the $3 - 20$ keV range - fitting the data with a single-temperature plus power-law (1T + IC) model.

5.8.3 Fitting with a 1T + IC Model

The 1T + IC model consists of a single-temperature plus a power-law model. For the power law model, the spectral index of SPT J2031 found by Raja et al. (2020) has been used. The spectral index of the radio halo was found to be 1.4 between the frequencies of 325 MHz and 1.7 GHz, and based on this, the photon spectral index parameter of the power-law component was fixed at $\Gamma = 2.4$. The best-fit values of the temperature and metal abundance obtained by fitting the 1T + IC model to the spectral data are $T = 11.5^{++7.1}_{-4.4}$ keV and $Z = 0.48^{+0.31}_{-0.25} Z_{\odot}$. Over the energy range of $20 - 80$ keV, the best-fit of the 1T + IC model yielded a flux of $1.68^{+0.22}_{-0.18} \times 10^{-12} \mathrm{ergs}^{-1}\mathrm{cm}^{-2}$ over the non-thermal component. The C-stat value for this model is 1780.4 with 1692 degrees of freedom.

This process was repeated by fitting the 1T + IC model to the spectral data in the $3 - 20$ keV energy band by allowing the photon spectral index to be free. The best-fit value for the temperature is $T = 2.1^{+2.6}_{-0.7}$ keV, and that for metal abundance is $Z = 0.44^{+0.24}_{-0.22} Z_{\odot}$. Although this model shows a better fit compared

to the 2T model and the (1T + IC) model with a fixed photon spectral index, the thermal component measured here does not agree with the corresponding *Chandra* data. From my deep *Chandra* observations of SPT J2031, the temperature was measured to be $13.8^{+2.3}_{-1.8}$ keV. Hence, the temperature value measured here is much lower than the temperature measured using *Chandra* data. Additionally, the emission measure of the thermal component is lesser than that of the IC component, indicating that the non-thermal emission is the dominant over all energies. Thus, this model is an unrealistic one.

5.8.4 Fitting in the 4 - 20 keV Energy Band

Madsen et al. (2020) found that the effective area of the FPMA detector could be slightly off below ~ 5 keV. In this case, the best-fit values for the 2T and 1T + IC models are bound to be different if carried out in the $4 - 20$ keV energy band. Hence, the fits were repeated from the global spectra in this energy band. The results from this fit are shown in table 5.3. The lower temperature out of the two values obtained for the 2T model is $5.3^{+1.6}_{-0.9}$ keV, which is lower than the temperature of $13.8^{+2.3}_{-1.8}$ keV measured using deep *Chandra* data. Additionally, the thermal component of the 1T + IC model with a free photon spectral index Γ is measured to be $5.9^{++2.1}_{-1.0}$ keV, which is also lower than the measured *Chandra* value. Hence, the 2T model and the 1T + IC model with free Γ can be ruled out in favor of the 1T + IC model with a fixed Γ.

Figure 5.10 shows the spectra obtained for both observations from both telescopes in the $4 - 20$ keV energy band. The left panel shows the spectra fit

Table 5.2: Results of the global spectral analysis in the 3–20 keV energy band. The statistical uncertainties are at the 90 percent confidence level, followed by the 90 percent systematic uncertainties.

Model	T_1 (keV)	Z ($Z_\odot$)	Norm$_1$[1] (10^{-3} cm^{-5})	T_2 (keV)	Γ	Norm$_2$ [1] (10^{-3} cm^{-5})	IC flux[2] (10^{-12} erg s^{-1} cm^{-2})	C-stat/dof[3]
1T	$9.2^{+0.4+0.3}_{-0.3-0.3}$	$0.03^{+0.02+0.01}_{-0.02-0.01}$	$7.47^{+0.25+0.13}_{-0.25-0.14}$	—	—	—	—	1903.1^{+202}_{-182}/1693
2T	$2.4^{+1.7+1.1}_{-0.5-1.0}$	$0.10^{+0.05+0.01}_{-0.05-0.02}$	$11.59^{+0.81+0.28}_{-0.78-0.40}$	$18.3^{+13.7+9.1}_{-2.2-2.5}$	—	$4.03^{+0.45+0.30}_{-0.66-0.35}$	—	1774.8^{+199}_{-172}/1691
1T + IC	$11.5^{+7.1+3.6}_{-4.4-2.6}$	$0.48^{+0.31+0.02}_{-0.25-0.02}$	$0.56^{+0.10+0.08}_{-0.09-0.08}$	—	2.4 (fixed)	$3.14^{+0.23+0.20}_{-0.32-0.20}$	$1.68^{+0.22+0.30}_{-0.18-0.28}$	1780.4^{+198}_{-175}/1692
1T + IC	$2.1^{+2.6+1.0}_{-0.7-0.9}$	$0.44^{+0.24-0.03}_{-0.22-0.03}$	$1.88^{+0.37+0.21}_{-0.31-0.18}$	—	$2.3^{+0.1+0.1}_{-0.2-0.1}$ (free)	$2.66^{+0.35+0.19}_{-0.36-0.20}$	$2.31^{+0.26+0.48}_{-0.22-0.43}$	1769.3^{+191}_{-170}/1691

[1] Normalization of the APEC thermal component. In models with an IC component, Norm$_2$ is the normalization of the power-law component, which is given in units of photons keV^{-1} cm^{-2} s^{-1} at 1 keV (10^{-3}).

[2] Non-thermal flux in the 20–80 keV band.

[3] Associated uncertainties are the distribution of C-stat values using 1000 realizations of the background.

Table 5.3: Same as Table 5.2, except the global spectral fitting is carried out in the 4–20 keV energy band.

Model	T_1 (keV)	Z ($Z_\odot$)	Norm$_1$ (10^{-3} cm^{-5})	T_2 (keV)	Γ	Norm$_2$ (10^{-3} cm^{-5})	IC flux (10^{-12} erg s^{-1} cm^{-2})	C-stat/dof
1T	$10.6^{+0.6+0.7}_{-0.6-0.6}$	$0.17^{+0.08+0.02}_{-0.07-0.04}$	$6.03^{+0.32+0.19}_{-0.29-0.20}$	—	—	—	—	1670.9^{+186}_{-166}/1593
2T	$5.3^{+1.6+1.4}_{-0.9-1.1}$	$0.11^{+0.05+0.01}_{-0.04-0.01}$	$6.76^{+0.77+0.86}_{-0.76-0.88}$	$18.1^{+14.4+10.8}_{-5.3-1.4}$	—	$1.95^{+0.62+0.88}_{-0.29-0.30}$	—	1618.5^{+177}_{-164}/1591
1T + IC	$12.6^{+8.8+5.2}_{-1.4-3.7}$	$0.46^{+0.11+0.03}_{-0.21-0.04}$	$1.17^{+0.44+0.64}_{-0.41-0.65}$	—	2.4 (fixed)	$2.68^{+0.38+0.77}_{-0.67-0.87}$	$1.36^{+0.16+0.27}_{-0.15-0.24}$	1633.5^{+183}_{-171}/1592
1T + IC	$5.9^{+2.1+0.3}_{-1.0-0.6}$	$0.11^{+0.04-0.02}_{-0.05-0.02}$	$6.39^{+0.11+0.67}_{-0.11-0.82}$	—	$1.6^{+0.7+0.3}_{-0.6-0.3}$ (free)	$0.26^{+0.05+0.09}_{-0.03-0.09}$	$3.93^{+0.76+0.48}_{-0.65-0.45}$	1618.4^{+179}_{-165}/1591

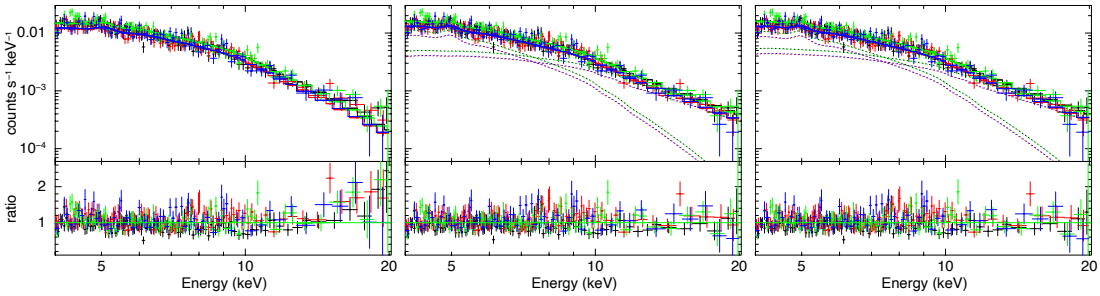

Figure 5.10: 4–20 keV global spectra of both observations and telescopes of SPT J2031. The left panel shows the spectra fit to the 1T model. The model provides a good fit below 10 keV, but a significant excess is observed at energies of $10-20$ keV. The middle panel shows the spectral data fit with the 2T model. This model seems to provide a good fit over the entire spectrum. The panel on the right shows the spectra fitted to the 1T + IC model with a free photon index.

to the 1T model. The model provides a good fit below 10 keV, but a significant excess is observed at energies of $10-20$ keV. The middle panel shows the spectral data fit with the 2T model. This model seems to provide a good fit over the entire spectrum. The panel on the right shows the spectra fitted to the 1T + IC model with a free photon index. Overall, the 2T model and the 1T + IC model with a free spectral index seem to fit the data equally well.

5.9 Discussion

5.9.1 Non-thermal Component

The results of the spectral fitting in the $3-20$ keV and the $4-20$ keV bands suggest that the 1T + IC model with a fixed photon spectral index offers the best-fit to the spectrum out of all the other models when compared with the results from the deep *Chandra* data.

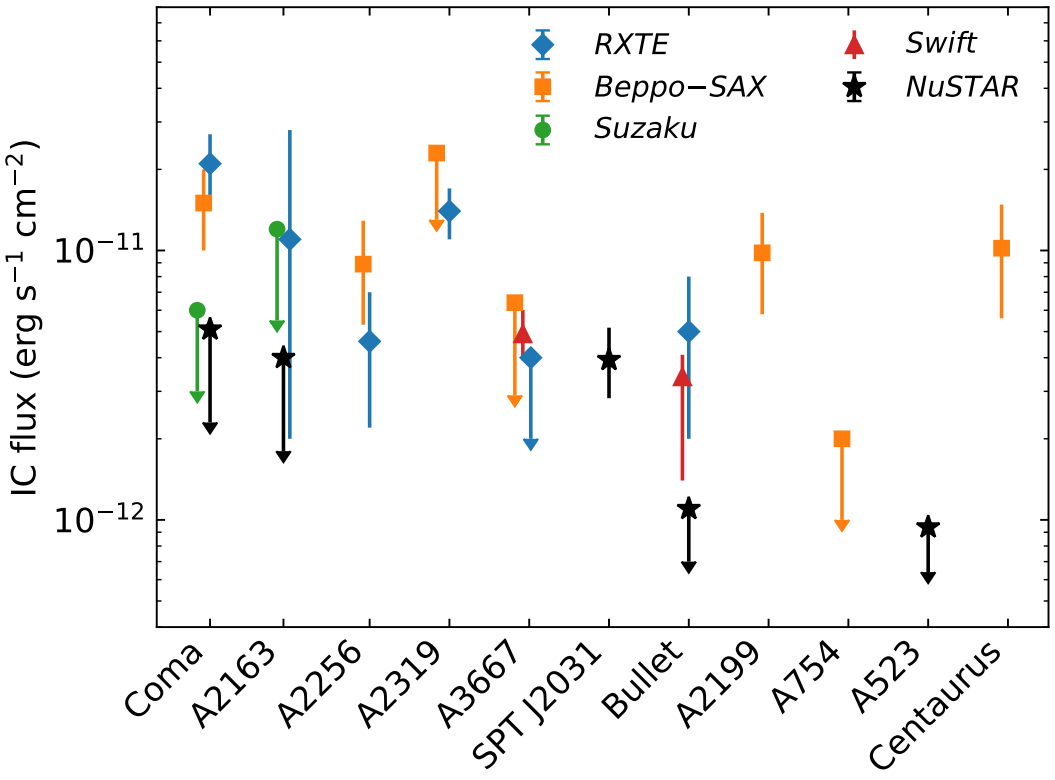

Figure 5.11: Comparing the non-thermal flux of the SPT J2031 cluster to those reported for other galaxy clusters by various X-ray observatories.

Figure 5.11 compares the estimated IC flux obtained for SPT J2031 in the 20-80 keV energy band with those of other galaxy clusters using various observatories. The 1T + IC model gives the best fit $20-80$ keV flux of $3.93^{+1.24}_{-1.10} \times 10^{-12}$ erg s^{-1} cm^{-2} on the non-thermal IC component. Our results are well in agreement with the non-thermal flux observed in most other merging galaxy clusters.

5.9.2 Magnetic Field

The average magnetic field strength in the ICM can be estimated from the flux of the IC emission. The synchrotron flux at the radio frequency ν_r and the IC flux at the X-ray frequency ν_x, respectively, are given as follows: (Govoni and Feretti, 2004):

$$S_{R(\nu_R)} = 1.7 \times 10^{-21} \frac{VN_0}{4\pi D^2} a(\delta) B^{1+\alpha} \left(\frac{4.3 \times 10^6}{\nu_r} \right)^{\alpha} \text{ and} \tag{5.8}$$

$$S_{IC(\nu_x)} = 4.2 \times 10^{-40} \frac{VN_0}{4\pi D^2} b(\delta) T^{1+\alpha} (1+z)^{3+\alpha} \left(\frac{2.1 \times 10^{10}}{\nu_x} \right)^{\alpha}, \tag{5.9}$$

where $a(\delta)$ and $b(\delta)$ are constants tabulated in Govoni and Feretti (2004); V is the emission volume, N_0 is the number density of the electrons, D is the source distance, and α is the spectral index.

Assuming that the IC flux is produced by the same relativistic electrons that produced the synchrotron radiation, Equations 5.8 and 5.9 can be used to determine the average magnetic field strength as shown in Equation 5.10:

$$B[\mu G]^{1+\alpha} = h(\alpha) \frac{S_R[Jy]}{S_{IC}[erg\ s^{-1}\ cm^{-2}]} (1+z)^{3+\alpha} \times (0.0545 \nu_R[MHz])^{\alpha} \times (E_2[keV]^{1-\alpha} - E_1[keV]^{1-\alpha}), \tag{5.10}$$

where $h(\alpha)$ is a constant tabulated in Govoni and Feretti (2004), S_R is the radio flux at frequency ν_R, S_{IC} is the X-ray flux, and E_1 and E_2 represent the energy interval over which the flux is measured.

Using the X-ray flux obtained in Section 5.9.1 and a radio flux of 16.9 ± 1.8 mJy at 325 MHz from Raja et al. (2020), the average magnetic field strength obtained is $0.06^{+0.05}_{-0.04}$ μG with the best 1T + IC model fit. Using the radio flux of 232.6 ± 24.3 mJy at 1.5 GHz from Intema et al. (2017), the average magnetic field strength obtained is $0.11^{+0.06}_{-0.05}$ μG. Both these values are in agreement with magnetic field strength values found in other galaxy clusters (Wik et al., 2014; Cova et al., 2019).

5.10 Conclusion

The primary findings of the detailed analysis of the deep *NuSTAR* observations of the merging cluster SPT J2031 are as follows:

- The global spectral data was first fit with the single-temperature (1T) model. The best-fit for this model shows a significant excess between energies of $10-20$ keV. Hence, this model does not provide a realistic description of the data.

- Subsequently, the global spectral data was fit with four other models - the two-temperature (2T) model, the single temperature plus power-law (1T + IC) model with a fixed photon spectral index Γ, and the 1T + IC model with a free photon spectral index. The temperature values obtained for the 2T

and 1T + IC model with free Γ are significantly lower than those obtained using corresponding *Chandra* data. Hence, the 1T + IC model with fixed Γ is the best-fitting, physically motivated model for the NuSTAR data.

- A possibility indicated by these findings is that a non-thermal component can explain the hard X-ray emission in the merging cluster SPT J2031, although a purely thermal origin cannot be ruled out.

- The 1T + IC model gives the best fit $20-80$ keV flux of $3.93^{+1.24}_{-1.10} \times 10^{-12}$ erg s^{-1} cm^{-2} on the non-thermal IC component. The estimated non-thermal flux is comparable to other galaxy clusters studied using NuSTAR and other X-ray instruments.

- The volume-averaged magnetic field strength over the entire region of radio emission is around $0.1-0.2$ μG based on the non-thermal flux and existing radio data of the cluster.

Chapter 6. A Detailed Analysis of the Large-scale Cold Fronts in the Perseus Cluster

6.1 Introduction

Cold Fronts are sharp contact discontinuities in the density and temperature of the ICM (for a review, see Markevitch and Vikhlinin (2007)). Unlike shock fronts, the brighter and denser side of this discontinuity is the colder one, and there is no significant change in pressure across the cold front. Cold fronts were first discovered owing to *Chandra's* sub-arcsecond angular resolution. The high-resolution capabilities of Chandra, combined with the high surface brightness of these cold fronts, have facilitated their clear identification and analysis. Abell 2142 and Abell 3667 were the first cold fronts discovered by *Chandra* (Markevitch et al., 2000b; Vikhlinin et al., 2001b).

Cold fronts in cooling cores are believed to occur when the merger of two sub-clusters takes place off-axis, resulting in the displacement of the dense core gas from its equilibrium position within the cluster's gravitational potential in a sloshing motion. Numerical simulations using hydrodynamics in Tittley and Henriksen (2005b); Ascasibar and Markevitch (2006) show that sloshing can be induced from minor mergers occurring due to infalling subclusters at a non-zero impact parameter.

As the ICM at the core of the cluster is displaced due to the infalling gas, it results in concentric cold fronts, thereby causing the cooler and denser parcels of gas from the core to come in contact with the hotter outskirts (Simionescu et al., 2012). Keshet (2012) suggests that the presence of such a spiral pattern exhibited by cold fronts in the innermost regions of cool core clusters indicates the existence of significant large-scale bulk spiral flows.

The Perseus cluster of galaxies has been extensively observed by *ROSAT, Chandra, XMM-Newton, Suzaku*, and *Hitomi*. It is the brightest, extended extra-galactic X-ray source. Simionescu et al. (2012) found, by combining observations from *ROSAT, XMM-Newton*, and *Suzaku*, the presence of a giant cold front at a distance of 700 kpc, which is almost half the virial radius. Walker et al. (2018) calculated the age of this large cold front to be 5 Gyr, based on the numerical simulations of the evolution of cold fronts.

Only two other clusters, Abell 2142 (Rossetti et al., 2013) and RXJ2014.8-2430 (Walker et al., 2014), have been identified with similar large-scale cold fronts that extend to approximately 0.5 times their respective r_{200} values. These clusters were discovered at higher redshifts. Within each of these systems, a distinct spiral pattern of concentric cold fronts can be observed on opposite sides of the cluster. These cold fronts extend outward at progressively larger distances, indicating an ongoing motion akin to a sloshing movement within the structure.

These large-scale cold fronts differ significantly from the cold fronts typically observed in the central regions of clusters. These larger cold fronts have expanded outward and developed over time. Given this extended time span, dif-

fusion processes have had a significantly longer duration to broaden the cold front edge, while instabilities such as Kelvin-Helmholtz instabilities have had more time to develop.

As cold fronts within clusters of galaxies move from the central core towards the outer regions, they encounter different layers of the intracluster medium (ICM) with distinct dominant physical processes. In the outskirts of clusters, the physics of the ICM is subject to increasing influence by the accretion of gas from large-scale structure filaments and infalling subgroups.

An analysis of the Perseus cluster by Simionescu et al. (2012) identified further indications of the sloshing spiral in the Perseus cluster based on mosaic data obtained from the *ROSAT PSPC*. These findings suggested that the spiral phenomenon extended even farther to the west, reaching nearly the virial radius (r_{200} = 1800 kpc = 80 arcmin for Perseus, (Urban et al., 2014)). Nevertheless, the limitations of ROSAT, such as its low effective area and the significant off-axis point spread function, prevented a definitive determination of whether the observed X-ray surface brightness excess to the west was associated with a cold front.

To tackle this issue, in AO17, we extended the XMM mosaic to cover the area stretching towards the virial radius. This expansion focused on a narrow strip to the west of the Perseus cluster, aimed at checking if there might be a cold front in that region.

We assume a flat cosmology with $H_0 = 70$ km s^{-1} Mpc^{-1}, $\Omega_m = 0.3$, $\Omega_\Lambda = 0.7$. The redshift is $z = 0.018$, where 1" corresponds to 4.892 kpc. All the error bars are at a 68% confidence level unless stated otherwise.

6.2 Data

Simionescu et al. (2012) used archival *ROSAT PSPC, XMM Newton*, and *Suzaku* observations to create a combined mosaic that showed evidence for large-scale motion in the ICM, which appeared as a spiraling pattern in the X-ray surface brightness profiles. The observations from *XMM-Newton* are tabulated in Table 6.1. The Obs IDs with an asterisk ($*$) symbol next to them are our new observations, which extend the mosaic out to the virial radius to the west (PI: Walker).

Table 6.1: Details of the new and archived XMM observations used to create the mosaic image of Perseus.

Obs. ID	**RA**	**Dec**	**Date**	**Exp (ks)**	**Distance (arcmin)**
0820720401*	03 13 29.22	+41 53 08.7	2019-03-04	28.8	74.01
Continued on next page					

Table 6.1 – continued from previous page

Obs. ID	RA	Dec	Date	Exp (ks)	Dist (arcmin)
0820720301*	03 13 16.44	+41 35 51.8	2019-02-26	25.0	73.28
0820720201*	03 15 26.68	+41 45 05.4	2019-02-24	25.3	50.74
0820720101*	03 15 16.88	+41 24 17.2	2019-02-20	25.4	51.06
0673020401	03 21 14.16	+41 10 52.3	2012-03-01	31.9	25.75
0673020201	03 23 07.63	+41 12 35.6	2011-09-10	39.0	41.78
0673020301	03 22 10.00	+41 23 00.0	2011-08-19	35.9	27.87
0672770101	03 28 00.10	+41 29 56.5	2011-08-04	16.9	92.28
0554500801	03 25 25.20	+40 46 23.6	2008-08-19	34.1	77.59

Continued on next page

Table 6.1 – continued from previous page

Obs. ID	RA	Dec	Date	Exp (ks)	Dist (arcmin)
0405410101	03 21 04.26	+41 56 05.0	2006-08-03	30.9	28.72
0405410201	03 18 39.93	+41 06 31.4	2006-08-03	34.0	27.35
0305690301	03 19 50.59	+41 53 34.3	2006-02-11	27.2	22.8
0305690401	03 21 53.70	+41 49 30.1	2006-02-11	27.9	30.14
0305690101	03 18 02.69	+41 16 60.0	2006-02-10	27.9	23.96
0305780101	03 19 48.00	+41 30 40.7	2006-01-29	125	0.18
0306680301	03 13 01.97	+41 20 01.2	2005-09-04	63.4	76.72
0305720101	03 17 57.99	+41 45 57.0	2005-09-01	21.8	25.42

Continued on next page

Table 6.1 – continued from previous page

Obs. ID	**RA**	**Dec**	**Date**	**Exp (ks)**	**Dist (arcmin)**
0305720301	03 22 15.99	+41 11 28.0	2005-08-03	28.3	33.95
0204720201	03 23 23.60	+41 31 41.0	2004-02-04	24.9	40.52
0204720101	03 21 38.59	+41 31 43.0	2004-02-04	17.9	20.87
0151560101	03 16 42.99	+41 19 29.0	2003-02-26	29.4	36.33
0002942401	03 15 01.40	+42 02 09.0	2002-01-28	7.9	61.83
0085590201	03 19 49.69	+41 05 47.0	2001-02-10	43.3	25
0085110101	03 19 48.16	+41 30 42.1	2001-01-30	60.8	0.2

Obtaining reliable temperature measurements outside of the virial radius r_{500} using *ROSAT, Chandra,* and *XMM Newton* is difficult compared to *Suzaku* due to several reasons. The low surface brightness and gas density of the X-ray

emitting gas in the outskirts pose difficulties in observing the ICM. Also, *ROSAT, Chandra, and XMM* have higher instrumental background levels compared to *Suzaku* (Walker and Lau, 2022). Suzaku has been able to obtain measurements of cluster temperatures out to the virial radius and beyond, thanks to its low instrumental background and large field-of-view. Because of this, archival Suzaku observations taken from the west of the cluster core were used to obtain temperature measurements for our analysis. The *Suzaku* observations are tabulated in Table 6.2.

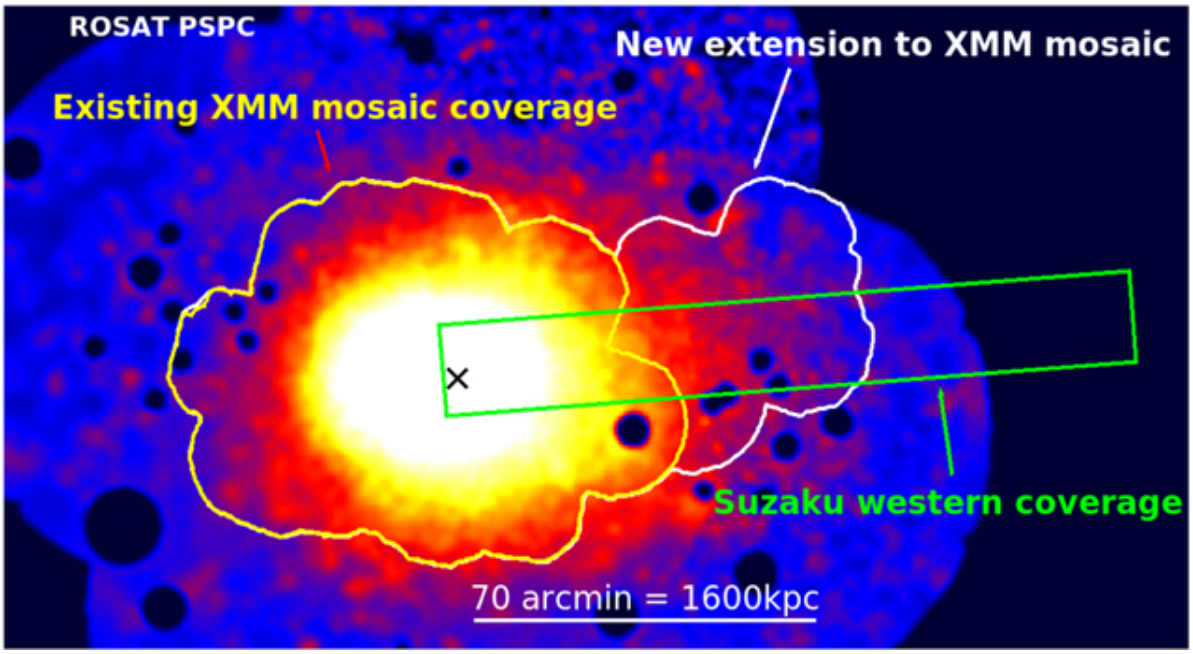

Figure 6.1: Shallow observations from the ROSAT PSPC covering a large area of the Perseus cluster. The ROSAT data is overlaid with old XMM observations (yellow contour), which have been extended to the virial radius in the west (white contour). The green rectangle shows the *Suzaku* observations in the western region of the cluster. The black cross represents the cluster core. Image credit: Walker et al. (2022)

Table 6.2: Suzaku data used for the analysis shown in this paper.

R.A.	**Obs**	**Dec.**
47.1647	805117010	41.6449
47.3511	805109010	41.6379
47.5391	805116010	41.63
47.7251	805108010	41.6255
47.9127	805115010	41.6204
48.1001	805107010	41.6131
48.2846	805114010	41.6054
48.4696	805106010	41.6016
48.8462	805105010	41.5856
49.2188	805104010	41.5721
49.5928	805103010	41.5523

Figure 6.1 shows the ROSAT PSPC mosaic of the Perseus cluster. The yellow contours overlaid on the ROSAT PSPC observation represent the existing XMM observations. The new XMM observations that extend over the surface brightness excess found in (Simionescu et al., 2012) are shown by the white contour. These new observations extend out to the virial radius in the west. The mosaic is also overlaid with *Suzaku* coverage of the cluster in the western direction (green rectangular contour). Out of the eight strips of existing *Suzaku* observations, only the one that overlaps with the new XMM data is shown here.

6.3 Image Analysis

The XMM data were reduced using the XMM extended source analysis software (Snowden et al., 2008). All the exposure maps and images were extracted in the $0.7-1.2$ keV energy band using MOS-SPECTRA and PN-SPECTRA, while particle background images were produced using MOS-BACK and PN-BACK. The CHEESE and WAVDETECT tools were used to identify and remove the point sources.

The background-subtracted, exposure-corrected image in the $0.7-1.2$ keV energy range is shown in the top panel of Figure 6.2. There are two edges visible in this image, at a distance of 1.2 Mpc and 1.7 Mpc from the core. The top panel of Figure 6.2 shows the XMM mosaic, where we see 2 surface brightness edges, Edge 1 and Edge 2. The bottom panel of Figure6.2 shows the GGM-filtered image (in orange) overlaid on the XMM mosaic (in blue). The two edges seen in the GGM image serve to emphasize where they lie with respect to the core.

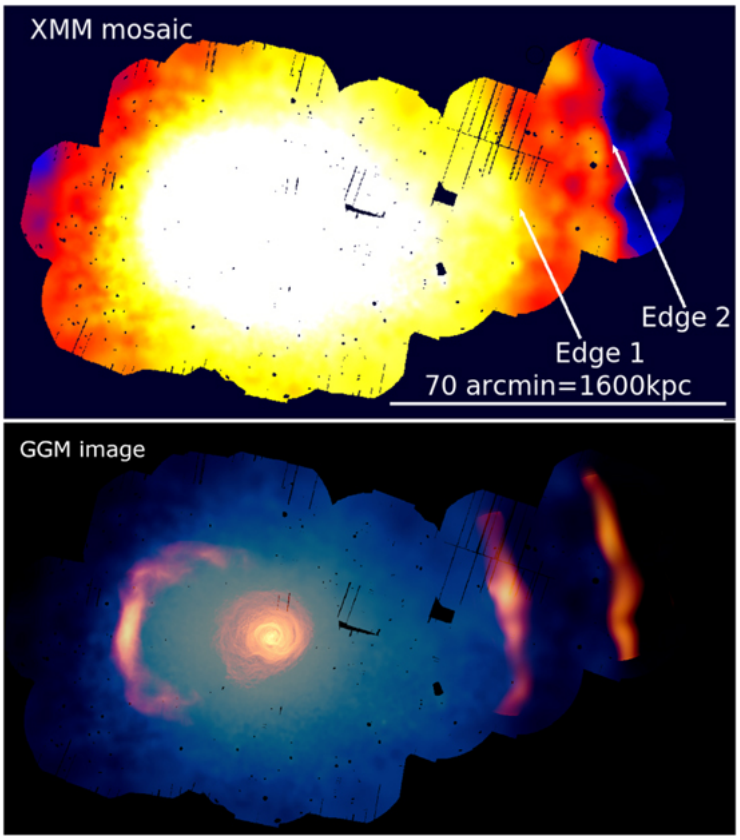

Figure 6.2: *Top:* The background-subtracted, exposure-corrected XMM mosaic of the cluster in the $0.7 - 1.2$ keV energy band. *Bottom:* The GGM map (orange) overlaid on the XMM mosaic (blue) to show where the two edges lie with respect to the cluster core. Image credit: **Walker et al. (2022)**

Figure 6.3 shows a portion of the background-subtracted, exposure-corrected image to the west of the core obtained from ROSAT PSPC observations. The white region indicates the sector over which the surface brightness profiles in the middle panel of Figure6.4 are extracted. Figure 6.4 shows, going from top to bottom, the *XMM* surface brightness profile, the *ROSAT* surface brightness profile, and the *Suzaku* temperature profile. Two edges, Edge 1 (green dashed line) and Edge 2 (blue dashed line), are seen at 1.2 Mpc and 1.7 Mpc, respectively, in the XMM data. The *ROSAT* surface brightness profile has been renormalized to compare with the XMM data. In this profile, Edge 1 can be seen, but the data quality is not sufficient to confirm the presence of Edge 2. The corresponding *Suzaku* temperature profile shows that at Edge 1, the density increases, and the temperature decreases. Similarly, at Edge 2, the density increases and the temperature decreases. Therefore, both the edges are consistent with being cold fronts.

6.4 Comparison with Simulations

Figure 6.5 shows the results of the numerical simulation of a galaxy cluster merger of two cool-core clusters from (Brzycki and ZuHone, 2019). This simulation incorporates dark matter, gas, and magnetic fields and a merger mass ratio of M = 3. The mass of the larger cluster is $M_{200} = 6 \times 10^{14} M_{\odot}$, which is similar to the mass of the Perseus cluster ($M = 6.6^{+0.43}_{-0.46} \times 10^{14} M_{\odot}$; Simionescu et al. 2011). The initial ratio of thermal pressure to magnetic pressure is $\beta = 200$. The initial impact parameter with which the two clusters approach each other is b

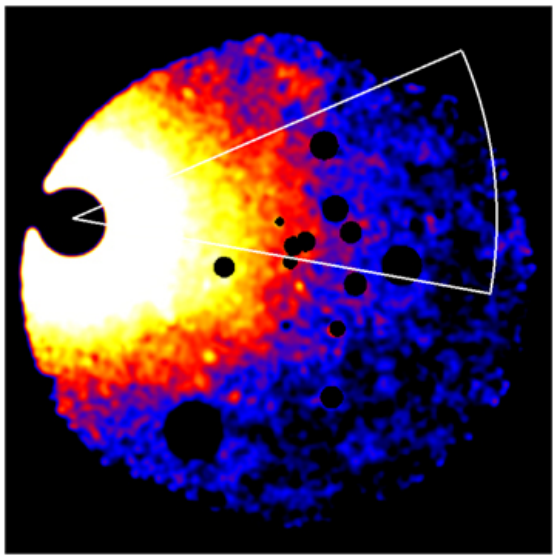

Figure 6.3: A portion of the background-subtracted, exposure-corrected image of the Perseus cluster to the west of the core obtained from *ROSAT PSPC* observations. The white region is the sector that has been used for the XMM analysis. Image credit: Walker et al. (2022)

= 1 Mpc, which triggers large-scale gas motions, leading to the formation of cold fronts. The top panel of the figure showcases the GGM-filtered image of the X-ray emission projected from the cluster 8.7 Gyr since the first core passage. There are two parallel cold fronts at a large radius, reaching up to approximately 1.6 Mpc. These cold fronts emerged shortly after the core passage near the central region and have since expanded outward. The magnetic field has stabilized the cold fronts in spite of the presence of turbulence and shock fronts.

From comparison to simulations from previous works, it appears that the relatively small mass ratio of the merger (or relatively large mass of the subcluster) is crucial for generating significant cold fronts because larger mergers induce faster gas movements, thereby lifting cold fronts to greater radii. Additionally, a

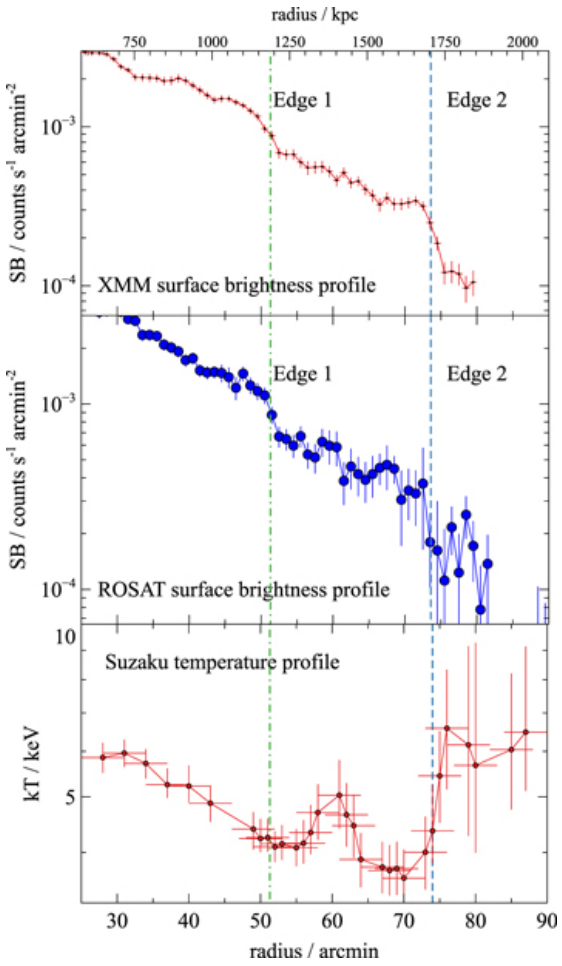

Figure 6.4: *Top:* The background-subtracted, projected surface brightness profile obtained using the *XMM* data. Two edges, Edge 1 (at 1.2Mpc) and Edge 2 (at 1.7Mpc), are detected in this profile. *Middle:* The surface brightness profile extracted from the same region using *ROSAT PSPC* data. Edge 1 is also seen here, but the data quality is not sufficient enough to confirm the presence of Edge 2. The ROSAT profile has been renormalized to compare with the XMM data. *Bottom:* The temperature profile was obtained using *Suzaku* data in the same direction as the XMM observations. There are two temperature drops observed corresponding to the location of both edges. The temperature decreases with the increase in density for Edge 1 and Edge 2, consistent with both being cold fronts. Image credit: Walker et al. (2022)

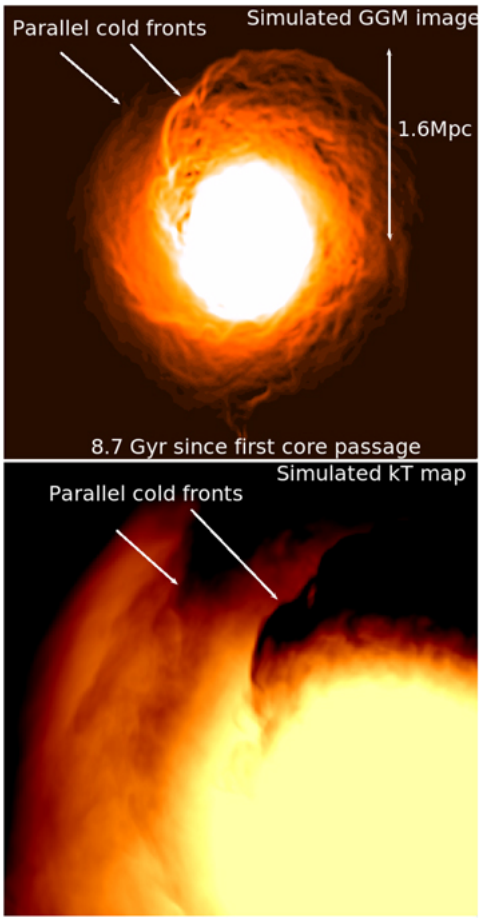

Figure 6.5: *Top:* Simulated GGM image of the sloshing 8.7 Gyr since the first core passage. The outer cold front reached a distance of 1.6 Mpc for this simulation. White arrows in the top left of this panel show the parallel cold fronts formed in the outskirts of the cluster. *Bottom:* Simulated temperature map of the sloshing zoomed on the parallel cold fronts. Image credit: Walker et al. (2022)

substantial impact parameter is also necessary, as a merger with a smaller impact parameter would disrupt the core. This hints at the possibility that the Perseus cluster might have experienced such an event in the distant past.

6.5 Analyzing Cold Fronts Using New Chandra Data

In this section, we look at the *Chandra* data of the 700 kpc cold front to the east of the cluster core. Previous *Chandra* observations analyzed by Walker et al. (2018) only cover the northernmost part of this giant cold front at 700 kpc, indicated by the dashed yellow box in Figure6.6. The new deep observations discussed in this paper cover the southern parts of the cold front (indicated by white dashed boxes in Figure 6.6), which have never been analyzed before.

All observations of the 700 kpc cold front have been taken by the *Chandra* X-ray telescope due to its unparalleled sub-arcsecond angular resolution. Even though the Field-of-View (FOV) of *Chandra* is much smaller than *XMM Newton*, it is the superior spatial resolution that allows us to study the substructure of the cold front, such as Kelvin-Helmholtz instabilities (KHIs), which cannot be resolved by *XMM-Newton.*

KHIs occur at the interface between two fluids with velocity shear. They manifest through features such as ripples or irregular structures in the ICM. With these new deep *Chandra* observations, the aim is to study such deviations from a smooth curve along the cold front caused by the KHIs.

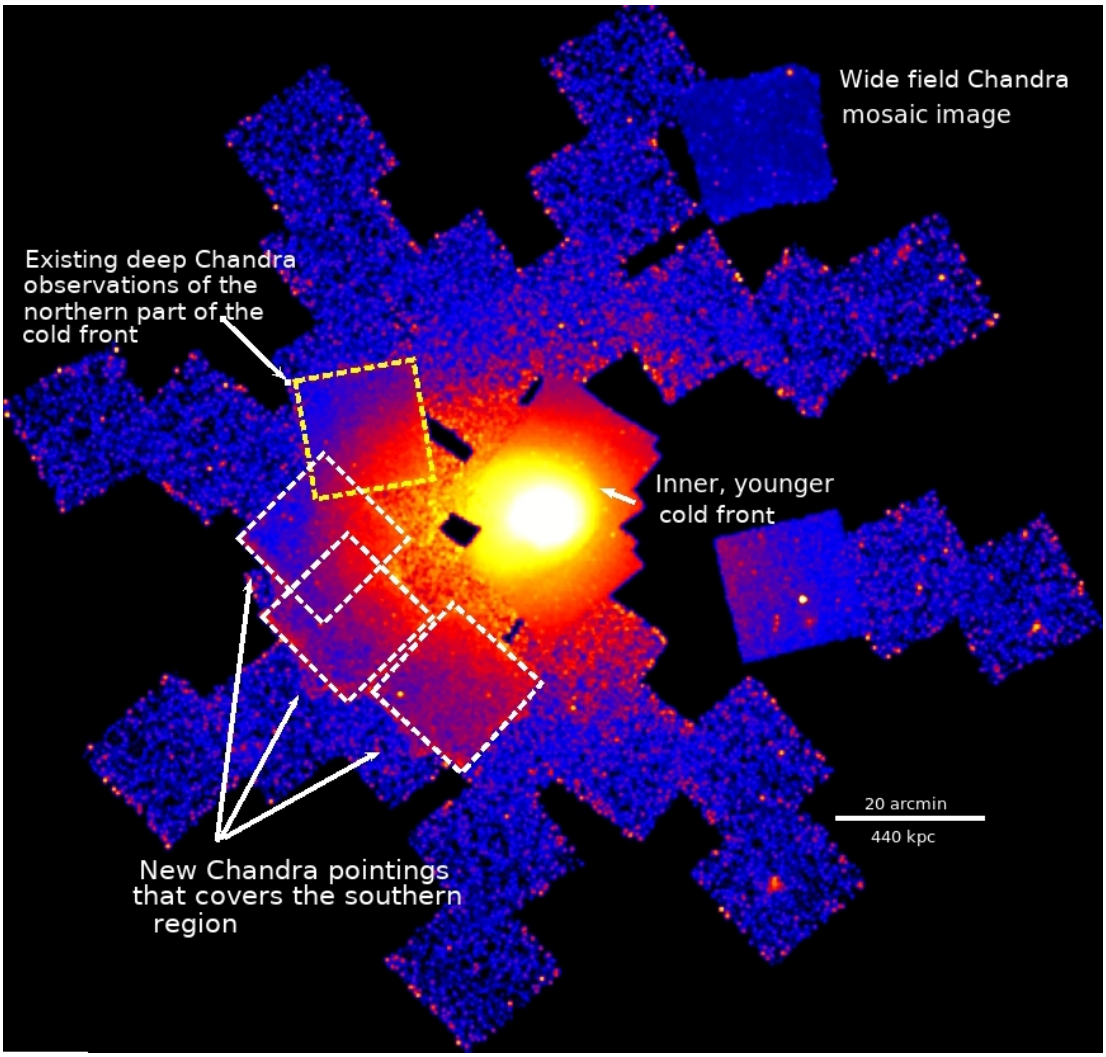

Figure 6.6: A mosaic of *Chandra* observations of the Perseus cluster. The wide field *Chandra* mosaic was constructed by stitching together deeper, proprietary observations over the regions in white dashed boxes with archived observations of Perseus. The yellow dashed box represents the northern region of the cold front which has been explored with *Chandra* by Walker et al. (2018). The focus of this project is the unexplored southern region of the cold front, shown by the white boxes in the figure.

6.5.1 Data

The Perseus cluster was observed by the *Chandra* Advanced CCD Imaging Spectrometer (ACIS) detector in the Very Faint (VFAINT) mode for a total of 220 ks spread over 8 observations (PI: S. A. Walker). Table 6.3 shows the Obs. ID, dates of observations, approximate exposure time, and cleaned exposure time of our proprietary *Chandra* observations. We used the new observations listed in Table 6.3 and archived *Chandra* observations listed in Table 6.4 to create the exposure-corrected mosaic image of the Perseus cluster shown in Figure 6.6. The targets of all of these observations lie within a 70 arcmin radius from the core of the Perseus cluster and were observed by ACIS-I.

Table 6.4: Details of the new and archived *Chandra* observations used to create the mosaic image of Perseus.

No.	**Obs. ID**	**Exp. time**	**RA**	**Dec**
1	5596	5	03 16 43.00	+41 19 29.40
2	5597	25	03 16 55.58	+41 21 31.62
Continued on next page				

Table 6.4 – continued from previous page

No.	Obs. ID.	Exp. time	RA	Dec
3	502	5	03 19 48.50	+41 30 27.00
4	11713	114	03 19 31.80	+41 37 49.00
5	12025	19	03 19 31.80	+41 37 49.00
6	12033	19	03 19 31.80	+41 37 49.00
7	12036	48	03 19 31.80	+41 37 49.00
8	11715	79	03 19 44.20	+41 25 18.00
9	11716	40	03 19 44.20	+41 25 18.00
10	12037	81	03 19 44.20	+41 25 18.00

Continued on next page

Table 6.4 – continued from previous page

No.	Obs. ID.	Exp. time	RA	Dec
11	11714	100	03 19 42.60	+41 34 07.00
12	13989	37.5	03 17 14.70	+42 19 42.60
13	13990	37.5	03 17 14.70	+42 20 03.50
14	13991	37.5	03 17 16.90	+42 20 03.80
15	13992	37.5	03 17 17.00	+42 19 43.00
16	17258	5	03 17 05.40	+40 42 22.52
17	17259	5	03 17 28.89	+40 57 24.70
18	17260	5	03 18 51.13	+40 58 39.85

Continued on next page

Table 6.4 – continued from previous page

No.	Obs. ID.	Exp. time	RA	Dec
19	17261	5	03 20 14.04	+41 01 33.44
20	17262	5	03 20 26.28	+40 46 19.46
21	17263	5	03 20 39.59	+40 30 47.42
22	17264	5	03 21 33.25	+41 03 00.60
23	17265	5	03 22 54.67	+41 03 39.13
24	17266	5	03 24 13.69	+40 58 02.22
25	17267	5	03 22 22.58	+41 19 13.99
26	17268	5	03 22 44.30	+41 34 37.28

Continued on next page

Table 6.4 – continued from previous page

No.	Obs. ID.	Exp. time	RA	Dec
27	17269	5	03 23 54.65	+41 40 39.21
28	17270	5	03 25 16.74	+41 42 03.43
29	17271	5	03 22 04.99	+41 49 16.30
30	17272	5	03 22 12.66	+42 05 10.06
31	17273	5	03 22 38.70	+42 19 32.12
32	17274	5	03 20 50.73	+41 59 58.49
33	17275	5	03 19 29.36	+41 58 00.08
34	17276	5	03 19 01.86	+42 13 44.91

Continued on next page

Table 6.4 – continued from previous page

No.	Obs. ID.	Exp. time	RA	Dec
35	17277	5	03 18 48.83	+42 29 02.79
36	17278	5	03 18 07.03	+41 57 16.65
37	17279	5	03 16 44.61	+41 54 59.53
38	17280	5	03 15 25.24	+41 59 39.87
39	17281	5	03 15 32.79	+41 22 35.28
40	17282	5	03 14 14.49	+41 19 08.88
41	17283	5	03 19 21.25	+41 11 23.33
42	17284	5	03 20 58.66	+41 16 53.44

Continued on next page

Table 6.4 – continued from previous page

No.	Obs. ID.	Exp. time	RA	Dec
43	17285	5	03 21 37.74	+41 33 28.72
44	17286	5	03 20 42.30	+41 50 05.79
45	19564	21.5	03 22 25.90	+41 27 30.30
46	20880	30	03 22 25.90	+41 27 30.30
47	20881	43.5	03 22 25.90	+41 27 30.30
48	19565	44.5	03 21 59.00	+41 41 31.10
49	19938	50.5	03 21 59.00	+41 41 31.10
50	22643	34	03 22 09.18	+41 17 11.42

Continued on next page

Table 6.4 – continued from previous page

No.	Obs. ID.	Exp. time	RA	Dec
51	22894	29.6	03 22 09.18	+41 17 11.42
52	23086	30.4	03 22 09.18	+41 17 11.42
53	23103	16	03 22 09.18	+41 17 11.42
54	22644	25	03 20 55.88	+41 08 19.54
55	22888	30	03 20 55.88	+41 08 19.54
56	23064	25	03 20 55.88	+41 08 19.54
57	23084	30	03 20 55.88	+41 08 19.54

Data reduction was carried out using CIAO, the data analysis system of *Chandra* (Fruscione et al., 2006) (version 4.14), along with CALDB, the calibration database (version 4.10.2) provided by the *Chandra* X-ray Center (CXC).

Table 6.3: Details of the new deep ($\sim$ 220 ks) *Chandra* observation of the Perseus Cluster using the ACIS-I instrument.

Obs ID	RA	Dec	Date	Exp time	Cleaned time
22643	03 22 09.18	+41 17 11.42	2019 Dec 19	31.48	31.48
22894	03 22 09.18	+41 17 11.42	2019 Dec 06	28.69	28.69
23086	03 22 09.18	+41 17 11.42	2019 Dec 03	30.03	30.03
23103	03 22 09.18	+41 17 11.42	2019 Dec 23	16.36	16.36
22644	03 20 55.88	+41 08 19.54	2019 Nov 06	24.75	24.75
22888	03 20 55.88	+41 08 19.54	2019 Nov 29	30.67	30.67
23064	03 20 55.88	+41 08 19.54	2019 Nov 07	24.0	24.0
23084	03 20 55.88	+41 08 19.54	2019 Nov 30	30.67	30.67

Initially, the primary data set consisted of event 1 files, which are lists of photons detected by the X-ray sensor. These files contain various measurements, such as the spatial position, arrival time, and energy of each photon. To process these event 1 files, the *chandra_repro* script was used, incorporating the most up-to-date calibrations for the detector. This involved applying corrections for charge transfer inefficiency (CTI), time-dependent gain adjustment, and the gain map. The processed output included response files, new bad pixel files, and level 2 event files.

To identify and remove flares and periods of unusually low count rates from the input light curves, the *deflare* routine was employed. This routine utilized the *lc_clean* script developed by M. Markevitch. As indicated in Table 6.3, the data were predominantly free from artifacts, resulting in a final cleaned exposure time of ~ 217 ks.

In order to create the exposure-corrected image, the cleaned files from the multiple observations were reprojected onto a common tangent point using the *reproject_obs* script. The *flux_obs* script was used to create an exposure-corrected image in the broad energy band ($0.5 - 7.0$ keV).

6.5.2 Image Analysis

Figure 6.6 shows the wide-field exposure-corrected mosaic of 57 ACIS-I *Chandra* observations of the Perseus cluster within a radius of 70 arcmin from the core of the cluster. The yellow dashed box represents the northern part of the colossal cold front, which was analyzed previously by Walker et al. (2018). The

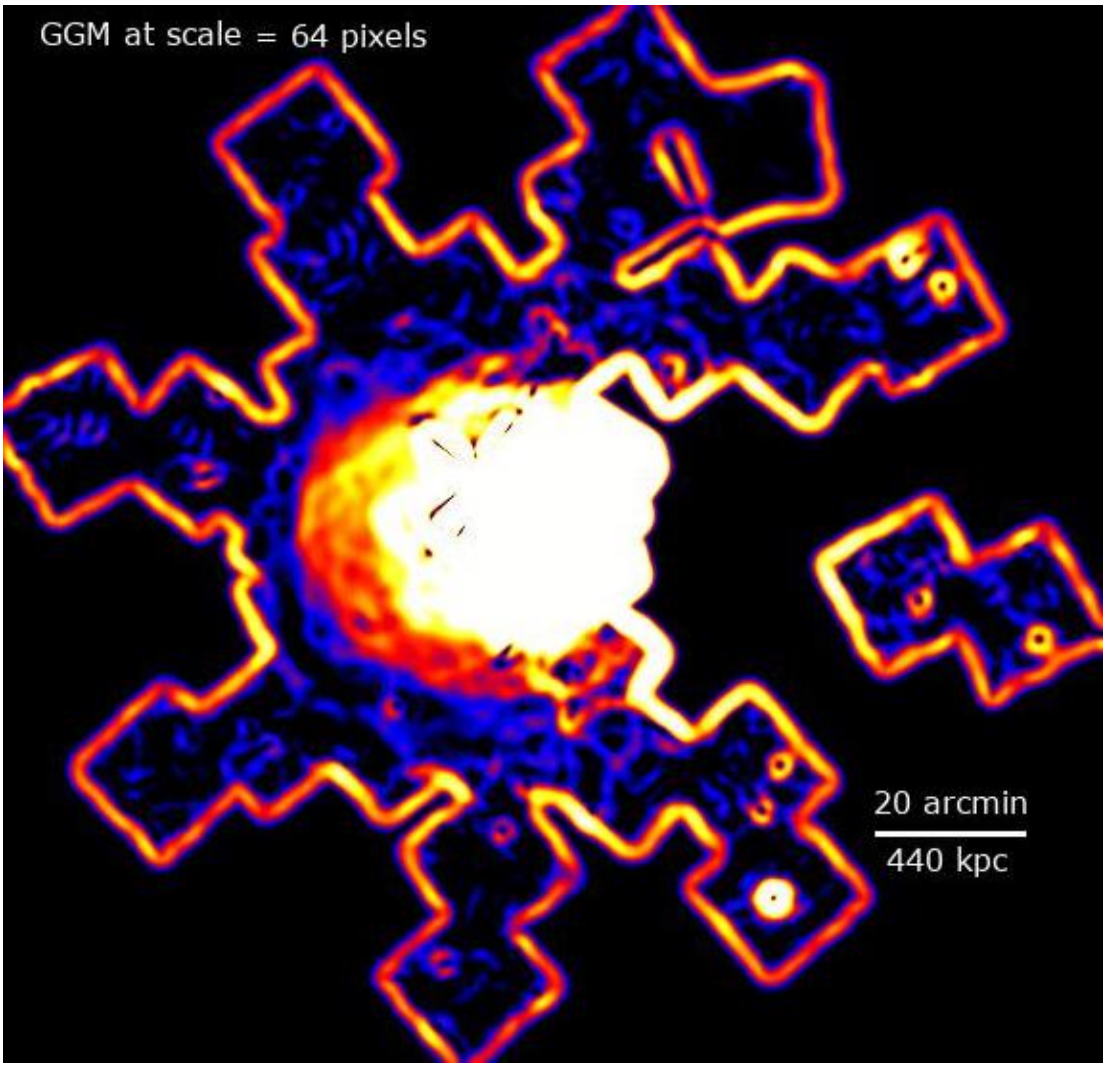

Figure 6.7: GGM image at scale = 64 pixels of the new deep *Chandra observations of the Perseus Cluster.*

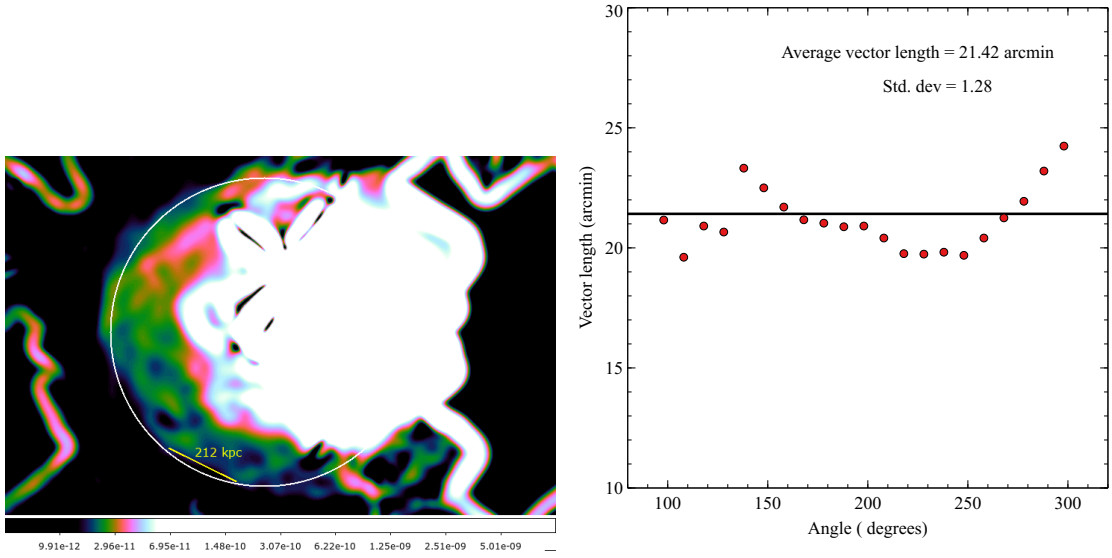

Figure 6.8: *Left:* This figure shows the GGM image of the cluster, zoomed in on the new deep *Chandra* observations. The white circle serves to emphasize the variation in the structure of the cold front. *Right:* This plot quantifies the variation in the structure of the cold front. Moving azimuthally along the cold front (shown by the change in angle on the X-axis, it should be noted wherever there is a sharp gradient in the surface brightness. The vector length (in arcmin) is the distance between this sharp gradient in the surface brightness and the center of the white circle shown in the left panel.

three white dashed boxes represent our new $\sim$ 220 ks observations, which are the subject of our present analysis.

GGM (Gaussian Gradient Magnitude) filtering is a technique for edge detection of substructures in cluster cores as well as outskirts (Sanders et al., 2016; Walker et al., 2016). The GGM filter identifies gradients in the surface brightness, with more pronounced gradients resulting in brighter edges within the image. Figure 6.7 shows the GGM filtered image of the entire cluster going to a radius of 70 arcmin in the energy range of $0.5 - 7.0$ keV at scale=64 pixels.

The left panel of Figure 6.8 shows a zoomed-in GGM image of the cluster showing the northern and southern parts of the cold front being analyzed. The white circle in this image highlights the curve that is expected to be followed by the cold front in the absence of KHI's, which can cause ripples or irregular features in the ICM. We examined how the smoothness of this curve changes for the Perseus cluster. This was done by determining where the steep change in surface brightness occurred along the curve and finding the distance of this gradient from a fixed reference point. The right side panel of Figure 6.8 shows a plot of vector length against angle. The vector length represents the radius from the fixed central point where the sharp change in the surface brightness is seen. The angle refers to the azimuthal angle along the smooth white curve. The vectors were equidistant at a spacing of 10 degrees along the curve. As seen in the plot, the curve of the ICM is not a smooth one. In fact, it is possible to quantify this variation of the curve by calculating the standard deviation of the curve, which in this case was calculated to be 1.28. Thus, there are regions in the cold front that are spread out, away from the curve. This non-smooth appearance of the cold front indicates the presence of Kelvin-Helmholtz instabilities caused due to the absence of magnetic field lines. We measured the length of this bay-like feature to be $\sim$ 212 kpc indicated by a solid yellow line in the left panel of Figure 6.8.

6.6 Conclusion

We have conducted an analysis of our new observations of the western outskirts of the Perseus cluster obtained from XMM-Newton. This investigation was prompted by previous findings from the ROSAT satellite, which indicated an excess in X-ray surface brightness in that direction. This excess appears to stem from the continuing gas sloshing phenomenon observed in the core, extending to around 700 kpc from the core towards the east. Our key findings are as follows:

- We have ascertained two distinct edges of surface brightness – one situated at 1.2 Mpc and the other at 1.7 Mpc.

- A spectral analysis carried out using Suzaku data for the same regions reveals temperature discontinuities at both of these edges seen in the XMM-Newton mosaic, consistent with both edges being cold fronts.

- We have also used a numerical simulation of the merger of binary galaxy clusters to demonstrate that cold fronts similar to the observed ones can indeed be produced as a result of sloshing motions within the core. These fronts extend outward to large radii and are stabilized against turbulence through the influence of magnetic fields. The formation of these large fronts seems to require a large impact parameter and mergers characterized by a low-mass ratio. Such mergers can induce rapid gas movements without completely disrupting the core.

- Using the existing archival observations within a $\sim$ 70 arcmin radius of the core of the Perseus cluster with the new, deep (220 ks) observations enabled the creation of an exposure-corrected mosaic. This image enhances a deviation from the curved feature of the 700 kpc cold front to the east.

- The curved feature seen in the 700 kpc cold front to the east in the mosaic appears to be consistent with the presence of KHIs. The length of the bay-like feature was measured to be $\sim$ 212 kpc.

Chapter 7. Conclusions and Future Work

In this chapter, I bring together the key findings from my comprehensive analysis of the merging galaxy clusters - SPT J2031 and the Perseus cluster, using data from *Chandra*, *NuSTAR*, and *XMM-Newton* observatories.

7.1 Conclusions for SPT-CL J2031-4037

7.1.1 Results from *Chandra* Data

I performed a detailed analysis of SPT J2031 using proprietary 250 ks *Chandra* observations. The results of the analysis are mentioned below:

- SPT J2031 exhibits merger geometry, as suggested by an offset between the brightest X-ray peaks in the exposure-corrected image from the *Chandra* observations and the two Brightest Cluster Galaxies in the HST optical image.
- I have utilized the GGM filtering technique to identify two sharp surface brightness edges in SPT J2031, the primary shock front, and the southeastern edge.
- I extracted surface brightness profiles across both the edges identified in the GGM image and fitted them with the broken power-law model to find the

density jump across the shock front. The sharp edge in the northwest direction is the primary shock with a density jump $\rho = 3.11 \pm 0.32$ corresponding to a Mach number of $3.23^{+0.89}_{-0.56}$.

- Due to the high Mach number obtained from the density jump in the primary shock front, I was able to compare the observed electron temperature profile of the primary shock with the collisional equilibration model and the instant shock heating model. I found that the post-shock electron temperature is lower than the temperature predicted for the instant shock heating model and favors the collisional equilibrational model. These findings are similar to the results in Russell et al. (2012, 2022). However, the instant heating model cannot be completely ruled out.

- The other surface brightness edge, the SE edge, is observed in the southeastern direction and also appears to be a shock front. It has a density jump $\rho = 1.47 \pm 0.26$ corresponding to a Mach number $M = 1.31^{+0.17}_{-0.16}$. Since the Mach number $M < 2$, I was not able to achieve enough separation between the two projected models of heating to be able to compare with the observed electron temperature profile.

- I plotted the density jump and Mach number of the primary shock as a function of the angle around the shock front and found that the density jump, and subsequently the Mach number peak at the center of the shock front, where the gradient in the GGM image is maximum. Both the density

jump and the Mach number taper off with a change in angle on both sides of this center point.

- I compared the temperature map obtained from the analysis with the simulations from Galaxy Cluster Merger Catalog (ZuHone, 2011) and found that these results are consistent with the simulation for a merger between two systems with mass ratio 1:3 and impact parameter, $b = 500$ kpc.

7.1.2 Results from *NuSTAR* Data

The primary findings of the detailed analysis of the deep (238 ks) *NuSTAR* observations of the merging cluster SPT J2031 are as follows:

- The global spectral data was fit with the single-temperature (1T) model. The best-fit for this model shows a significant excess between energies of $10 - 20$ keV. Hence, this model does not provide a realistic description of the data.

- Subsequently, the global spectral data was fit with four other models - the two-temperature (2T) model, the single temperature plus power-law (1T + IC) model with a fixed photon spectral index Γ, and the 1T + IC model with a free photon spectral index. The temperature values obtained for the 2T and 1T + IC model with free Γ are significantly lower than those obtained using corresponding *Chandra* data. Hence, the 1T + IC model with fixed Γ is the best-fitting, physically motivated model for the *NuSTAR* data.

- A possibility indicated by the findings is that a non-thermal component can explain the hard X-ray emission in the merging cluster SPT J2031, although a purely thermal origin cannot be ruled out.

- The $1T+IC$ model gives the best fit $20-80$ keV flux of $3.93^{+1.24}_{-1.10} \times 10^{-12}$ erg s^{-1} cm^{-2} on the non-thermal IC component. The estimated non-thermal flux is comparable to other galaxy clusters studied using *NuSTAR* and other X-ray instruments.

- The volume-averaged magnetic field strength over the entire region of radio emission is around $0.1-0.2$ μG based on the non-thermal flux and existing radio data of the cluster.

7.2 Conclusions for the Perseus Cluster

We have conducted an analysis of the newer observations of the western outskirts of the Perseus cluster obtained from *XMM-Newton*. This investigation was prompted by previous findings from the *ROSAT* satellite, which indicated an excess in X-ray surface brightness in that direction. This excess appears to stem from the continuing gas sloshing phenomenon observed in the core, extending to around 700 kpc from the core towards the east. Our key findings are as follows:

- It has been ascertained that there are two distinct edges of surface brightness – one situated at 1.2 Mpc and the other at 1.7 Mpc.

- A spectral analysis carried out using *Suzaku* data for the same regions reveals temperature discontinuities at both of these edges seen in the *XMM-Newton* mosaic, consistent with both edges being cold fronts.

- Comparisons with numerical simulation of the merger of binary galaxy clusters demonstrate that cold fronts similar to the observed ones can indeed be produced as a result of sloshing motions within the core. These fronts extend outward to large radii and are stabilized against turbulence through the influence of magnetic fields. The formation of these large fronts seems to require a large impact parameter and mergers characterized by a low-mass ratio. Such mergers can induce rapid gas movements without completely disrupting the core.

- Using the existing archival observations within a $\sim$ 70 arcmin radius of the core of the Perseus cluster with the new, deep (220 ks) observations, I created an exposure-corrected mosaic. This image enhances a deviation from the curved feature of the cold front.

- The curved feature seen in the mosaic appears to be consistent with the presence of KHIs. The length of the bay-like feature was measured to be $\sim$ 212 kpc.

7.3 Future Work

To improve the outcomes of my analysis of SPT J2031, I refer to the existing literature that highlights the enhancements achieved in the results for

comparable clusters. A great example of this is Abell 2146, where significant improvements in its temperature map were realized through deeper *Chandra* observations.

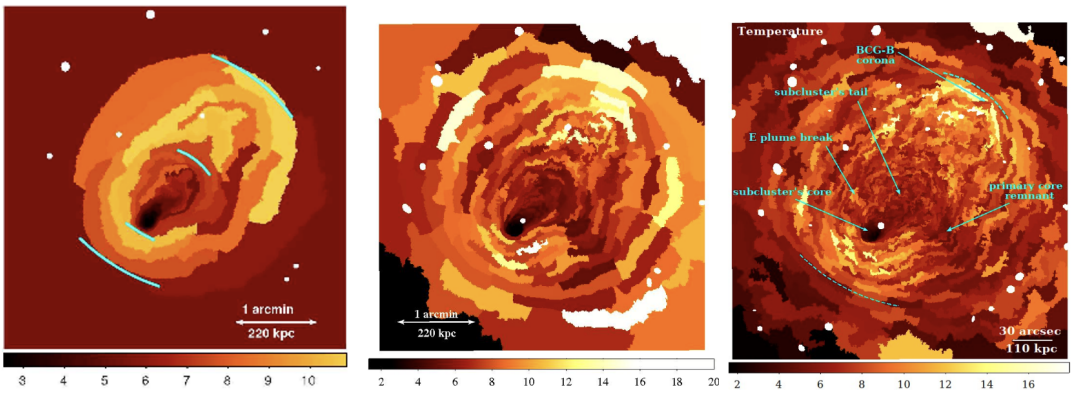

Figure 7.1: All the panels here show the projected temperature map (in keV) with S/N = 32, obtained from the *Chandra* observations of the merging galaxy cluster Abell 2146, with point sources removed. *Left:* Temperature map obtained from 43 ks of data. The blue lines correspond to the approximate locations of the jumps in the surface brightness edges (Russell et al., 2010). *Middle:* Temperature map obtained from 400 ks of data by Russell et al. 2012. *Right:* Temperature map obtained from 2Ms of Chandra data (Russell et al., 2022). This figure shows that increasing the exposure time dramatically increases the spatial resolution of the temperature map.

Fig. 7.1 shows the projected temperature maps of Abell 2146 (Russell et al., 2010, 2012, 2022), obtained from *Chandra* observations for $\sim$ 40 ks, $\sim$ 400 ks, and $\sim$ 2 Ms, respectively. The S/N = 32 ($\sim$ 1000 counts) for each of the temperature maps. The first panel shows the temperature map obtained from 43 ks of Chandra data. The blue lines correspond to the approximate locations of the jumps in the surface brightness edges. The errors in the temperature were approximately $\sim$ 15 %, but the bins with temperatures greater than 10 keV were poorly constrained, with errors greater than $\sim$ 30 % (Russell et al., 2010). The

middle panel in Fig. 7.1 shows the temperature map obtained from $\sim$ 400 ks of data. The errors in the temperature are approximately $\sim$ 15%. However, the error in temperature drops to less than 10% in the sub-cluster core, where the temperature falls below 2 keV. Similar to the first panel, the temperatures over 10 keV are poorly constrained by the energy range of Chandra, and the errors increase to $\sim$ 30% in these bins (Russell et al., 2012). The last panel in Fig. 7.1 shows the temperature map obtained using $\sim$ 2 Ms of *Chandra* data. The uncertainty in the temperatures is $\sim$ 15 %, but for regions at lower temperatures, the uncertainties in temperature vary from $\sim$ 5 % to $\sim$ 10 %(Russell et al., 2022).

As seen in Fig. 7.1, with deeper data, Russell et al. (2012) and Russell et al. (2022) obtained a temperature map with a higher spatial resolution, allowing the authors to distinguish the changes in temperatures for much smaller scales. For the same signal-to-noise ratio S/N = 32, there is a significant improvement in the ability to resolve the spatial structure of the merging system. Hence, the deeper data allowed for better mapping of the complex structures and for reducing the uncertainties at temperatures lower than 2 keV.

The original image of SPT J2031 obtained by *Chandra* was only 10 ks long. This archived observation of SPT J2031, which first indicated the likelihood of the system being a major merger, was so shallow that only two surface brightness peaks could be observed, and no edges could be identified.

In order to investigate SPT J2031, I co-proposed and obtained 250 ks of *Chandra* data. The top-right and bottom-right panels in Fig 4.3 show the temperature map and GGM image, respectively, obtained as a result of my analysis

of the deep *Chandra* data. Using this deep data, I was able to resolve the surface brightness peaks, obtain a temperature map with signal-to-noise S/N = 32, identify the shocks in the system, and extract temperature values on the northwest region of the cluster.

Deeper *Chandra* data ($\sim$ 1 Ms) of the system would significantly improve my results and would provide a clearer picture of the cluster in the following ways:

- Since X-ray data have a low number of photons, they are governed by Poisson statistics, where the uncertainty in the temperature measurements is inversely proportional to the square root of the photon count. Hence, going from 250 ks of data to 1 Ms of data would quadruple the photon count and bring down the uncertainty in temperature measurements by a factor of 2, making these measurements more precise and reliable.

- The deeper data would result in a more accurate temperature map by better defining the temperatures in the regions that were previously poorly constrained.

- If the S/N ratio is kept the same, the size of the regions would be reduced by a factor of 4. It would enable the exploration of the finer structures of the shocks in the system.

- More data would make it possible to constrain the temperature at the SE edge and even test the shock front for electron-ion equilibration.

- Over the primary shock front, I would be able to make the regions over which the spectra are extracted even narrower, which would help us understand the shock even better.

The proposed future mission *AXIS* (Advanced X-ray Imaging Satellite) would have a similar PSF to *Chandra*, a FOV for sub-arcsecond imaging that is 70 times larger than *Chandra* by area, and an effective area that is 10 times larger than *Chandra* at 1 keV (Mushotzky et al., 2019). Observations made with *AXIS* would allow for a temperature map with a much higher resolution. *AXIS* would also be transformative in detecting cold fronts in the Perseus Cluster.

Another proposed future mission, *HEX-P* (High Energy X-ray Probe), which would have better spatial resolution and a larger effective area compared to *NuSTAR*, would help improve the study of the IC emission from SPT J2031 and make more accurate measurements of the magnetic field.

References

Andernach, H. and Zwicky, F. (2017). English and Spanish Translation of Zwicky's (1933) The Redshift of Extragalactic Nebulae. *arXiv e-prints*, page arXiv:1711.01693.

Arnaud, K. A. (1996). XSPEC: The First Ten Years. In Jacoby, G. H. and Barnes, J., editors, *Astronomical Data Analysis Software and Systems V*, volume 101 of *Astronomical Society of the Pacific Conference Series*, page 17.

Ascasibar, Y. and Markevitch, M. (2006). The Origin of Cold Fronts in the Cores of Relaxed Galaxy Clusters. *apj*, 650(1):102–127.

Baring, M. G. (1997). Diffusive Shock Acceleration : the Fermi Mechanism. In Giraud-Heraud, Y. and Tran Thanh van, J., editors, *Very High Energy Phenomena in the Universe; Moriond Workshop*, page 97.

Bell, A. R. (1978). The acceleration of cosmic rays in shock fronts - I. *mnras*, 182:147–156.

Bian, N., Emslie, A. G., and Kontar, E. P. (2012). A classification scheme for turbulent acceleration processes in solar flares. *ApJ*, 754:103.

Blandford, R. and Eichler, D. (1987). Particle acceleration at astrophysical shocks: A theory of cosmic ray origin. *physrep*, 154(1):1–75.

Blundell, S. and Blundell, K. (2010). *Concepts in thermal physics*.

Böhringer, H., Schuecker, P., Guzzo, L., Collins, C. A., Voges, W., Cruddace, R. G., Ortiz-Gil, A., Chincarini, G., De Grandi, S., Edge, A. C., MacGillivray, H. T., Neumann, D. M., Schindler, S., and Shaver, P. (2004). The ROSAT-ESO Flux Limited X-ray (REFLEX) Galaxy cluster survey. V. The cluster catalogue. *aap*, 425:367–383.

Botteon, A., Brunetti, G., Ryu, D., and Roh, S. (2020). Shock acceleration efficiency in radio relics. *aap*, 634:A64.

Botteon, A., Gastaldello, F., Brunetti, G., and Kale, R. (2016). A M 3 shock in 'El Gordo' cluster and the origin of the radio relic. *mnras*, 463(2):1534–1542.

Bourdin, H., Mazzotta, P., Markevitch, M., Giacintucci, S., and Brunetti, G. (2013). Shock Heating of the Merging Galaxy Cluster A521. *apj*, 764(1):82.

Boyd, T. J. M. and Sanderson, J. J. (1969). *Plasma dynamics*.

Bradač, M., Clowe, D., Gonzalez, A. H., Marshall, P., Forman, W., Jones, C., Markevitch, M., Randall, S., Schrabback, T., and Zaritsky, D. (2006). Strong and Weak Lensing United. III. Measuring the Mass Distribution of the Merging Galaxy Cluster 1ES 0657-558. *apj*, 652(2):937–947.

Brunetti, G. (2003). Modelling the Non-Thermal Emission from Galaxy Clusters. In Bowyer, S. and Hwang, C.-Y., editors, *Matter and Energy in Clusters of Galaxies*, volume 301 of *Astronomical Society of the Pacific Conference Series*, page 349.

Brunetti, G. and Jones, T. K. (2014). Cosmic rays in galaxy clusters and their nonthermal emission. *Int. J. Mod. Phys. D*, 23:1430007.

Brzycki, B. and ZuHone, J. (2019). A parameter space exploration of galaxy cluster mergers. ii. effects of magnetic fields. *The Astrophysical Journal*, 883:118.

Canning, R. E. A., Russell, H. R., Fabian, A. C., Crawford, C. S., and Hatch, N. A. (2011). Abell 2146: riding the wake of a merging galaxy cluster. *memsai*, 82:662.

Cassano, R. (2009). Large-scale Diffuse Radio Emission from Clusters of Galaxies and the Importance of Low Frequency Radio Observations. In Saikia, D. J., Green, D. A., Gupta, Y., and Venturi, T., editors, *The Low-Frequency Radio Universe*, volume 407 of *Astronomical Society of the Pacific Conference Series*, page 223.

Chandrasekhar, S. (1961). *Hydrodynamic and hydromagnetic stability*.

Chiu, I., Mohr, J. J., McDonald, M., Bocquet, S., Desai, S., Klein, M., Israel, H., Ashby, M. L. N., Stanford, A., Benson, B. A., Brodwin, M., Abbott, T. M. C., Abdalla, F. B., Allam, S., Annis, J., Bayliss, M., Benoit-Lévy, A., Bertin, E., Bleem, L., Brooks, D., Buckley-Geer, E., Bulbul, E., Capasso, R., Carlstrom, J. E., Rosell, A. C., Carretero, J., Castander, F. J., Cunha, C. E., D'Andrea, C. B., da Costa, L. N., Davis, C., Diehl, H. T., Dietrich, J. P., Doel, P., Drlica-Wagner, A., Eifler, T. F., Evrard, A. E., Flaugher, B., García-Bellido,

J., Garmire, G., Gaztanaga, E., Gerdes, D. W., Gonzalez, A., Gruen, D., Gruendl, R. A., Gschwend, J., Gupta, N., Gutierrez, G., Hlavacek-L, J., Honscheid, K., James, D. J., Jeltema, T., Kraft, R., Krause, E., Kuehn, K., Kuhlmann, S., Kuropatkin, N., Lahav, O., Lima, M., Maia, M. A. G., Marshall, J. L., Melchior, P., Menanteau, F., Miquel, R., Murray, S., Nord, B., Ogando, R. L. C., Plazas, A. A., Rapetti, D., Reichardt, C. L., Romer, A. K., Roodman, A., Sanchez, E., Saro, A., Scarpine, V., Schindler, R., Schubnell, M., Sharon, K., Smith, R. C., Smith, M., Soares-Santos, M., Sobreira, F., Stalder, B., Stern, C., Strazzullo, V., Suchyta, E., Swanson, M. E. C., Tarle, G., Vikram, V., Walker, A. R., Weller, J., and Zhang, Y. (2018). Baryon content in a sample of 91 galaxy clusters selected by the South Pole Telescope at 0.2 ¡z ¡ 1.25. *mnras*, 478(3):3072–3099.

Clowe, D., Bradač, M., Gonzalez, A. H., Markevitch, M., Randall, S. W., Jones, C., and Zaritsky, D. (2006). A Direct Empirical Proof of the Existence of Dark Matter. *apjl*, 648(2):L109–L113.

Clowe, D., Gonzalez, A., and Markevitch, M. (2004). Weak-Lensing Mass Reconstruction of the Interacting Cluster 1E 0657-558: Direct Evidence for the Existence of Dark Matter. *apj*, 604(2):596–603.

Cova, F., Gastaldello, F., Wik, D. R., Boschin, W., Botteon, A., Brunetti, G., Buote, D. A., De Grandi, S., Eckert, D., Ettori, S., Feretti, L., Gaspari, M., Ghizzardi, S., Giovannini, G., Girardi, M., Govoni, F., Molendi, S., Murgia, M., Rossetti, M., and Vacca, V. (2019). A joint XMM-NuSTAR observation of the galaxy cluster Abell 523: Constraints on inverse Compton emission. *aap*, 628:A83.

Dasadia, S., Sun, M., Sarazin, C., Morandi, A., Markevitch, M., Wik, D., Feretti, L., Giovannini, G., Govoni, F., and Vacca, V. (2016). A Strong Merger Shock in Abell 665. *apjl*, 820(1):L20.

Di Mascolo, L., Mroczkowski, T., Churazov, E., Markevitch, M., Basu, K., Clarke, T. E., Devlin, M., Mason, B. S., Randall, S. W., Reese, E. D., Sunyaev, R., and Wik, D. R. (2019). An ALMA+ACA measurement of the shock in the Bullet Cluster. *aap*, 628:A100.

Drury, L. O. (2012). First-order Fermi acceleration driven by magnetic reconnection. *Monthly Notices of the Royal Astronomical Society*, 422(3):2474–2476.

Dursi, L. J. and Pfrommer, C. (2008). Draping of Cluster Magnetic Fields over Bullets and BubblestextemdashMorphology and Dynamic Effects. *apj*, 677(2):993–1018.

Ebeling, H., Edge, A. C., Bohringer, H., Allen, S. W., Crawford, C. S., Fabian, A. C., Voges, W., and Huchra, J. P. (1998). The rosat brightest cluster sample – i. the compilation of the sample and the cluster log n–log s distribution. *Monthly Notices of the Royal Astronomical Society*, 301:881–914.

Feretti, L., Gioia, I., and Giovannini, G., editors (2002). *Merging Processes in Galaxy Clusters*, volume 272 of *Astrophysics and Space Science Library*.

Feretti, L., Giovannini, G., and Govoni, F.and Murgia, M. (2012). Clusters of galaxies: Observational properties of the diffuse radio emission. *Astron Astrophys Rev*, 20.

Ferrari, C., Govoni, F., Schindler, S., Bykov, A. M., and Rephaeli, Y. (2008). Observations of Extended Radio Emission in Clusters. *ssr*, 134(1-4):93–118.

Forman, W., Jones, C., Churazov, E., Markevitch, M., Nulsen, P., Vikhlinin, A., Begelman, M., Böhringer, H., Eilek, J., Heinz, S., Kraft, R., Owen, F., and Pahre, M. (2007). Filaments, Bubbles, and Weak Shocks in the Gaseous Atmosphere of M87. *apj*, 665(2):1057–1066.

Forman, W. R., Simionescu, A., Churazov, E., Jones, C., Werner, N., Nulsen, P., Kraft, R., Randall, S., and Boehringer, H. (2010). Large and Small Scale Gas Motions in the Virgo/M87 System. In *AAS/High Energy Astrophysics Division #11*, volume 11 of *AAS/High Energy Astrophysics Division*, page 34.15.

Fruscione, A., McDowell, J. C., Allen, G. E., Brickhouse, N. S., Burke, D. J., Davis, J. E., Durham, N., Elvis, M., Galle, E. C., Harris, D. E., Huenemoerder, D. P., Houck, J. C., Ishibashi, B., Karovska, M., Nicastro, F., Noble, M. S., Nowak, M. A., Primini, F. A., Siemiginowska, A., Smith, R. K., and Wise, M. (2006). CIAO: Chandra's data analysis system. In Silva, D. R. and Doxsey, R. E., editors, *Society of Photo-Optical Instrumentation Engineers (SPIE) Conference Series*, volume 6270 of *Society of Photo-Optical Instrumentation Engineers (SPIE) Conference Series*, page 62701V.

Fusco-Femiano, R., Dal Fiume, D., Feretti, L., Giovannini, G., Grandi, P., Matt, G., Molendi, S., and Santangelo, A. (1999). Hard X-Ray Radiation in the Coma Cluster Spectrum. *apjl*, 513(1):L21–L24.

Fusco-Femiano, R., Landi, R., and Orlandini, M. (2005). Confirmation of the Presence of Nonthermal Hard X-Ray Excess in the Cluster A2256 from Two Epoch Observations. *apjl*, 624(2):L69–L72.

Govoni, F. and Feretti, L. (2004). Magnetic Fields in Clusters of Galaxies. *International Journal of Modern Physics D*, 13(8):1549–1594.

Hull, A. J., Scudder, J. D., Larson, D. E., and Lin, R. (2001). Electron heating and phase space signatures at supercritical, fast mode shocks. *jgr*, 106(A8):15711–15734.

Intema, H., Jagannathan, P., Mooley, K., and Frail, D. (2017). The gmrt 150 mhz all-sky radio survey-first alternative data release tgss adr1. *aap*, 598:A78.

Jokipii, J. R. (1979). Introductory lecture. In Arons, J., McKee, C., and Max, C., editors, *Particle Acceleration Mechanisms in Astrophysics*, volume 56 of *American Institute of Physics Conference Series*, pages 1–9.

Jones, C. (2002). Exploring the Cooling Flow Riddle: the Nature and Effect of Nuclear Outbursts in the Elliptical Galaxy NGC4636. Chandra Proposal.

Kalberla, P. M. W., Burton, W. B., Hartmann, D., Arnal, E. M., Bajaja, E., Morras, R., and Pöppel, W. G. L. (2005). The Leiden/Argentine/Bonn (LAB) Survey of Galactic HI. Final data release of the combined LDS and IAR surveys with improved stray-radiation corrections. *aap*, 440(2):775–782.

Keshet, U. (2012). Spiral Flows in Cool-core Galaxy Clusters. *apj*, 753(2):120.

Landau, L. D. and Lifshitz, E. M. (1987). *Fluid Mechanics, Second Edition: Volume 6 (Course of Theoretical Physics)*. Course of theoretical physics / by L. D. Landau and E. M. Lifshitz, Vol. 6. Butterworth-Heinemann, 2 edition.

Longair, M. S. (2011). *High Energy Astrophysics*. Cambridge University Press.

Macario, G., Markevitch, M., Giacintucci, S., Brunetti, G., Venturi, T., and Murray, S. S. (2011). A Shock Front in the Merging Galaxy Cluster A754: X-ray and Radio Observations. *apj*, 728(2):82.

Madsen, K. K., Grefenstette, B. W., Pike, S., Miyasaka, H., Brightman, M., Forster, K., and Harrison, F. A. (2020). NuSTAR low energy effective area correction due to thermal blanket tear. *arXiv e-prints*, page arXiv:2005.00569.

Mantz, A. B., Allen, S. W., Morris, R. G., Simionescu, A., Urban, O., Werner, N., and Zhuravleva, I. (2017). The metallicity of the intracluster medium over cosmic time: further evidence for early enrichment. *mnras*, 472(3):2877–2888.

Markevitch, M. (2003). The Most Interesting Cluster in the Universe. Chandra Proposal.

Markevitch, M. (2006a). Chandra Observation of the Most Interesting Cluster in the Universe. In Wilson, A., editor, *The X-ray Universe 2005*, volume 604 of *ESA Special Publication*, page 723.

Markevitch, M. (2006b). Chandra Observation of the Most Interesting Cluster in the Universe. In Wilson, A., editor, *The X-ray Universe 2005*, volume 604 of *ESA Special Publication*, page 723.

Markevitch, M. (2010). Intergalactic shock fronts. *arXiv e-prints*, page arXiv:1010.3660.

Markevitch, M., Gonzalez, A. H., Clowe, D., Vikhlinin, A., Forman, W., Jones, C., Murray, S., and Tucker, W. (2004). Direct Constraints on the Dark Matter Self-Interaction Cross Section from the Merging Galaxy Cluster 1E 0657-56. *apj*, 606(2):819–824.

Markevitch, M., Ponman, T. J., Nulsen, P. E. J., Bautz, M. W., Burke, D. J., David, L. P., Davis, D., Donnelly, R. H., Forman, W. R., Jones, C., Kaastra, J., Kellogg, E., Kim, D. W., Kolodziejczak, J., Mazzotta, P., Pagliaro, A., Patel, S., Van Speybroeck, L., Vikhlinin, A., Vrtilek, J., Wise, M., and Zhao, P. (2000a). Chandra Observation of Abell 2142: Survival of Dense Subcluster Cores in a Merger. *ApJ*, 541(2):542–549.

Markevitch, M., Ponman, T. J., Nulsen, P. E. J., Bautz, M. W., Burke, D. J., David, L. P., Davis, D., Donnelly, R. H., Forman, W. R., Jones, C., Kaastra,

J., Kellogg, E., Kim, D. W., Kolodziejczak, J., Mazzotta, P., Pagliaro, A., Patel, S., Van Speybroeck, L., Vikhlinin, A., Vrtilek, J., Wise, M., and Zhao, P. (2000b). Chandra Observation of Abell 2142: Survival of Dense Subcluster Cores in a Merger. *apj*, 541(2):542–549.

Markevitch, M., Sarazin, C. L., and Vikhlinin, A. (1999). Physics of the Merging Clusters Cygnus A, A3667, and A2065. *apj*, 521(2):526–530.

Markevitch, M. and Vikhlinin, A. (2007). Shocks and cold fronts in galaxy clusters. *physrep*, 443(1):1–53.

McNamara, B. R., Nulsen, P. E. J., Wise, M. W., Rafferty, D. A., Carilli, C., Sarazin, C. L., and Blanton, E. L. (2005). The heating of gas in a galaxy cluster by x-ray cavities and large-scale shock fronts. *Nature Astronomy*, 433:45–47.

Miniati, F., Ryu, D., Kang, H., Jones, T. W., Cen, R., and Ostriker, J. P. (2000). Properties of Cosmic Shock Waves in Large-Scale Structure Formation. *ApJ*, 542(2):608–621.

Mirakhor, M. S., Walker, S. A., and Runge, J. (2023). A deep dive: Chandra observations of the NGC 4839 group falling into the Coma cluster. *mnras*.

Mirakhor, M. S., Walker, S. A., Runge, J., and Diwanji, P. (2022). Possible non-thermal origin of the hard X-ray emission in the merging galaxy cluster SPT-CL J2031-4037. *mnras*, 516(2):1855–1864.

Montgomery, M. D., Asbridge, J. R., and Bame, S. J. (1970). Vela 4 plasma observations near the Earth's bow shock. *jgr*, 75(7):1217.

Mushotzky, R., Aird, J., Barger, A. J., Cappelluti, N., Chartas, G., Corrales, L., Eufrasio, R., Fabian, A. C., Falcone, A. D., Gallo, E., Gilli, R., Grant, C. E., Hardcastle, M., Hodges-Kluck, E., Kara, E., Koss, M., Li, H., Lisse, C. M., Loewenstein, M., Markevitch, M., Meyer, E. T., Miller, E. D., Mulchaey, J., Petre, R., Ptak, A. J., Reynolds, C. S., Russell, H. R., Safi-Harb, S., Smith, R. K., Snios, B., Tombesi, F., Valencic, L., Walker, S. A., Williams, B. J., Winter, L. M., Yamaguchi, H., Zhang, W. W., Arenberg, J., Brandt, N., Burrows, D. N., Georganopoulos, M., Miller, J. M., Norman, C. A., and Rosati, P. (2019). The Advanced X-ray Imaging Satellite. In *Bulletin of the American Astronomical Society*, volume 51, page 107.

Ness, N. F., Scearce, C. S., and Seek, J. B. (1964). Initial Results of the Imp 1 Magnetic Field Experiment. *jgr*, 69(17):3531–3569.

Nulsen, P. E. J., McNamara, B. R., Wise, M. W., and David, L. P. (2005). The Cluster-Scale AGN Outburst in Hydra A. *apj*, 628(2):629–636.

Nurgaliev, D., McDonald, M., Benson, B. A., Bleem, L., Bocquet, S., Forman, W. R., Garmire, G. P., Gupta, N., Hlavacek-Larrondo, J., Mohr, J. J., Nagai, D., Rapetti, D., Stark, A. A., Stubbs, C. W., and Vikhlinin, A. (2017). Testing for X-Ray-SZ Differences and Redshift Evolution in the X-Ray Morphology of Galaxy Clusters. *apj*, 841(1):5.

Owers, M. S., Nulsen, P. E. J., Couch, W. J., Ma, C.-J., David, L. P., Forman, W. R., Hopkins, A. M., Jones, C., and van Weeren, R. J. (2014). A Merger Shock in A2034. *apj*, 780(2):163.

Owers, M. S., Randall, S. W., Nulsen, P. E. J., Couch, W. J., David, L. P., and Kempner, J. C. (2011). The Dissection of Abell 2744: A Rich Cluster Growing Through Major and Minor Mergers. *apj*, 728(1):27.

Peterson, J. and Fabian, A. (2006). X-ray spectroscopy of cooling clusters. *Physics Reports*, 427(1):1–39.

Petrosian, V. (2012). Stochastic acceleration by turbulence. *Space Science Reviews*, 173(1):535–556.

Piffaretti, R., Arnaud, M., Pratt, G. W., Pointecouteau, E., and Melin, J. B. (2011). The MCXC: a meta-catalogue of x-ray detected clusters of galaxies. *aap*, 534:A109.

Plagge, T., Benson, B. A., Ade, P. A. R., Aird, K. A., Bleem, L. E., Carlstrom, J. E., Chang, C. L., Cho, H. M., Crawford, T. M., Crites, A. T., de Haan, T., Dobbs, M. A., George, E. M., Hall, N. R., Halverson, N. W., Holder, G. P., Holzapfel, W. L., Hrubes, J. D., Joy, M., Keisler, R., Knox, L., Lee, A. T., Leitch, E. M., Lueker, M., Marrone, D., McMahon, J. J., Mehl, J., Meyer, S. S., Mohr, J. J., Montroy, T. E., Padin, S., Pryke, C., Reichardt, C. L., Ruhl, J. E., Schaffer, K. K., Shaw, L., Shirokoff, E., Spieler, H. G., Stalder, B., Staniszewski, Z., Stark, A. A., Vanderlinde, K., Vieira, J. D., Williamson, R.,

and Zahn, O. (2010). Sunyaev-Zel'dovich Cluster Profiles Measured with the South Pole Telescope. *apj*, 716(2):1118–1135.

Planck Collaboration, Ade, P. A. R., Aghanim, N., Arnaud, M., Ashdown, M., Aumont, J., Baccigalupi, C., Banday, A. J., Barreiro, R. B., Bartlett, J. G., Bartolo, N., Battaner, E., Battye, R., Benabed, K., Benoît, A., Benoit-Lévy, A., Bernard, J. P., Bersanelli, M., Bielewicz, P., Bock, J. J., Bonaldi, A., Bonavera, L., Bond, J. R., Borrill, J., Bouchet, F. R., Boulanger, F., Bucher, M., Burigana, C., Butler, R. C., Calabrese, E., Cardoso, J. F., Catalano, A., Challinor, A., Chamballu, A., Chary, R. R., Chiang, H. C., Chluba, J., Christensen, P. R., Church, S., Clements, D. L., Colombi, S., Colombo, L. P. L., Combet, C., Coulais, A., Crill, B. P., Curto, A., Cuttaia, F., Danese, L., Davies, R. D., Davis, R. J., de Bernardis, P., de Rosa, A., de Zotti, G., Delabrouille, J., Désert, F. X., Di Valentino, E., Dickinson, C., Diego, J. M., Dolag, K., Dole, H., Donzelli, S., Doré, O., Douspis, M., Ducout, A., Dunkley, J., Dupac, X., Efstathiou, G., Elsner, F., Enßlin, T. A., Eriksen, H. K., Farhang, M., Fergusson, J., Finelli, F., Forni, O., Frailis, M., Fraisse, A. A., Franceschi, E., Frejsel, A., Galeotta, S., Galli, S., Ganga, K., Gauthier, C., Gerbino, M., Ghosh, T., Giard, M., Giraud-Héraud, Y., Giusarma, E., Gjerløw, E., González-Nuevo, J., Górski, K. M., Gratton, S., Gregorio, A., Gruppuso, A., Gudmundsson, J. E., Hamann, J., Hansen, F. K., Hanson, D., Harrison, D. L., Helou, G., Henrot-Versillé, S., Hernández-Monteagudo, C., Herranz, D., Hildebrandt, S. R., Hivon, E., Hobson, M., Holmes, W. A., Hornstrup, A., Hovest, W., Huang, Z., Huffenberger, K. M., Hurier, G., Jaffe, A. H., Jaffe, T. R., Jones, W. C., Juvela, M., Keihänen, E., Keskitalo, R., Kisner, T. S., Kneissl, R., Knoche, J., Knox, L., Kunz, M., Kurki-Suonio, H., Lagache, G., Lähteenmäki, A., Lamarre, J. M., Lasenby, A., Lattanzi, M., Lawrence, C. R., Leahy, J. P., Leonardi, R., Lesgourgues, J., Levrier, F., Lewis, A., Liguori, M., Lilje, P. B., Linden-Vørnle, M., López-Caniego, M., Lubin, P. M., Macías-Pérez, J. F., Maggio, G., Maino, D., Mandolesi, N., Mangilli, A., Marchini, A., Maris, M., Martin, P. G., Martinelli, M., Martínez-González, E., Masi, S., Matarrese, S., McGehee, P., Meinhold, P. R., Melchiorri, A., Melin, J. B., Mendes, L., Mennella, A., Migliaccio, M., Millea, M., Mitra, S., Miville-Deschênes, M. A., Moneti, A., Montier, L., Morgante, G., Mortlock, D., Moss, A., Munshi, D., Murphy, J. A., Naselsky, P., Nati, F., Natoli, P., Netterfield, C. B., Nørgaard-Nielsen, H. U., Noviello, F., Novikov, D., Novikov, I., Oxborrow, C. A., Paci, F., Pagano, L., Pajot, F., Paladini, R., Paoletti, D., Partridge, B., Pasian, F., Patanchon, G., Pearson, T. J., Perdereau, O., Perotto, L., Perrotta, F., Pettorino, V., Piacentini, F., Piat, M.,

Pierpaoli, E., Pietrobon, D., Plaszczynski, S., Pointecouteau, E., Polenta, G., Popa, L., Pratt, G. W., Prézeau, G., Prunet, S., Puget, J. L., Rachen, J. P., Reach, W. T., Rebolo, R., Reinecke, M., Remazeilles, M., Renault, C., Renzi, A., Ristorcelli, I., Rocha, G., Rosset, C., Rossetti, M., Roudier, G., Rouillé d'Orfeuil, B., Rowan-Robinson, M., Rubiño-Martín, J. A., Rusholme, B., Said, N., Salvatelli, V., Salvati, L., Sandri, M., Santos, D., Savelainen, M., Savini, G., Scott, D., Seiffert, M. D., Serra, P., Shellard, E. P. S., Spencer, L. D., Spinelli, M., Stolyarov, V., Stompor, R., Sudiwala, R., Sunyaev, R., Sutton, D., Suur-Uski, A. S., Sygnet, J. F., Tauber, J. A., Terenzi, L., Toffolatti, L., Tomasi, M., Tristram, M., Trombetti, T., Tucci, M., Tuovinen, J., Türler, M., Umana, G., Valenziano, L., Valiviita, J., Van Tent, F., Vielva, P., Villa, F., Wade, L. A., Wandelt, B. D., Wehus, I. K., White, M., White, S. D. M., Wilkinson, A., Yvon, D., Zacchei, A., and Zonca, A. (2016). Planck 2015 results. XIII. Cosmological parameters. *aap*, 594:A13.

Press, W. H. and Schechter, P. (1974). Formation of Galaxies and Clusters of Galaxies by Self-Similar Gravitational Condensation. *apj*, 187:425–438.

Raja, R., Rahaman, M., Datta, A., Burns, J. O., Intema, H. T., van Weeren, R. J., Hallman, E. J., Rapetti, D., and Paul, S. (2020). Diffuse radio emission in the galaxy cluster SPT-CL J2031-4037: a steep-spectrum intermediate radio halo? *mnras*, 493(1):L28–L32.

Randall, S. W., Markevitch, M., Clowe, D., Gonzalez, A. H., and Bradač, M. (2008). Constraints on the Self-Interaction Cross Section of Dark Matter from Numerical Simulations of the Merging Galaxy Cluster 1E 0657-56. *apj*, 679(2):1173–1180.

Rephaeli, Y. and Gruber, D. (2002). Results from a Second Rossi X-Ray Timing Explorer Observation of the Coma Cluster. *apj*, 579(2):587–591.

Richard, J., Patricio, V., Martinez, J., Bacon, R., Clement, B., Weilbacher, P., Soto, K., Wisotzki, L., Vernet, J., Pello, R., Schaye, J., Turner, M., and Martinsson, T. (2015). MUSE observations of the lensing cluster SMACSJ2031.8-4036: new constraints on the mass distribution in the cluster core. *mnras*, 446:L16–L20.

Rossetti, M., Eckert, D., De Grandi, S., Gastaldello, F., Ghizzardi, S., Roediger, E., and Molendi, S. (2013). Abell 2142 at large scales: An extreme case for sloshing? *aap*, 556:A44.

Russell, H. R., McNamara, B. R., Sanders, J. S., Fabian, A. C., Nulsen, P. E. J., Canning, R. E. A., Baum, S. A., Donahue, M., Edge, A. C., King, L. J., and O'Dea, C. P. (2012). Shock fronts, electron-ion equilibration and intracluster medium transport processes in the merging cluster Abell 2146. *mnras*, 423(1):236–255.

Russell, H. R., Nulsen, P. E. J., Caprioli, D., Chadayammuri, U., Fabian, A. C., Kunz, M. W., McNamara, B. R., Sanders, J. S., Richard-Laferrière, A., Beleznay, M., Canning, R. E. A., Hlavacek-Larrondo, J., and King, L. J. (2022). The structure of cluster merger shocks: turbulent width and the electron heating time-scale. *mnras*, 514(1):1477–1493.

Russell, H. R., Sanders, J. S., Fabian, A. C., Baum, S. A., Donahue, M., Edge, A. C., McNamara, B. R., and O'Dea, C. P. (2010). Chandra observation of two shock fronts in the merging galaxy cluster Abell 2146. *mnras*, 406(3):1721–1733.

Sanders, J. S. (2006). Contour binning: a new technique for spatially resolved X-ray spectroscopy applied to Cassiopeia A. *mnras*, 371(2):829–842.

Sanders, J. S., Fabian, A. C., Russell, H. R., Walker, S. A., and Blundell, K. M. (2016). Detecting edges in the X-ray surface brightness of galaxy clusters. *mnras*, 460(2):1898–1911.

Sarazin, C. L. (1986). X-ray emission from clusters of galaxies. *Reviews of Modern Physics*, 58(1):1–115.

Sarazin, C. L. (2008). Gas Dynamics in Clusters of Galaxies. In Plionis, M., López-Cruz, O., and Hughes, D., editors, *A Pan-Chromatic View of Clusters of Galaxies and the Large-Scale Structure*, volume 740, page 24. Springer, Dordrecht.

Sarkar, A., Randall, S., Su, Y., Alvarez, G. E., Sarazin, C., Nulsen, P., Blanton, E., Forman, W., Jones, C., Bulbul, E., Zuhone, J., Andrade-Santos, F., Johnson, R. E., and Chakraborty, P. (2022). Discovery of a Premerger Shock in an Intercluster Filament in Abell 98. *apjl*, 935(2):L23.

Simionescu, A., Allen, S. W., Mantz, A., Werner, N., Takei, Y., Morris, R. G., Fabian, A. C., Sanders, J. S., Nulsen, P. E. J., George, M. R., and Taylor, G. B. (2011). Baryons at the edge of the x-ray–brightest galaxy cluster. *Science*, 331:1576–1579.

Simionescu, A., Werner, N., Urban, O., Allen, S. W., Fabian, A. C., Sanders, J. S., Mantz, A., Nulsen, P. E. J., and Takei, Y. (2012). Large-scale Motions in the Perseus Galaxy Cluster. *ApJ*, 757(2):182.

Smith, R. K., Brickhouse, N. S., Liedahl, D. A., and Raymond, J. C. (2001). Collisional Plasma Models with APEC/APED: Emission-Line Diagnostics of Hydrogen-like and Helium-like Ions. *apjl*, 556:L91–L95.

Snowden, S. L., Mushotzky, R. F., Kuntz, K. D., and Davis, D. S. (2008). A catalog of galaxy clusters observed by xmm-newton. *Astronomy & Astrophysics*, 478:615–658.

Spergel, D. N. and Steinhardt, P. J. (2000). Observational Evidence for Self-Interacting Cold Dark Matter. *prl*, 84(17):3760–3763.

Takizawa, M. (1999). Two-Temperature Intracluster Medium in Merging Clusters of Galaxies. *apj*, 520(2):514–528.

Tittley, E. R. and Henriksen, M. (2005a). Cluster Mergers, Core Oscillations, and Cold Fronts. *apj*, 618(1):227–236.

Tittley, E. R. and Henriksen, M. (2005b). Cluster Mergers, Core Oscillations, and Cold Fronts. *apj*, 618(1):227–236.

Trümper, J. (1990). The rosat mission. *International Astronomical Union Colloquium*, 115:291–294.

Urban, O., Simionescu, A., Werner, N., Allen, S. W., Ehlert, S., Zhuravleva, I., Morris, R. G., Fabian, A. C., Mantz, A., Nulsen, P. E. J., Sanders, J. S., and Takei, Y. (2014). Azimuthally resolved X-ray spectroscopy to the edge of the Perseus Cluster. *mnras*, 437(4):3939–3961.

van Weeren, R. J., de Gasperin, F., Akamatsu, H., Brüggen, M., Feretti, L., Kang, H., Stroe, A., and Zandanel, F. (2019). Diffuse Radio Emission from Galaxy Clusters. *ssr*, 215(1):16.

Vietri, M. (2008). *Foundations of High Energy Astrophysics*. University of Chicago Press.

Vikhlinin, A., Markevitch, M., and Murray, S. S. (2001a). A Moving Cold Front in the Intergalactic Medium of A3667. *ApJ*, 551(1):160–171.

Vikhlinin, A., Markevitch, M., and Murray, S. S. (2001b). A Moving Cold Front in the Intergalactic Medium of A3667. *apj*, 551(1):160–171.

Vikhlinin, A., Markevitch, M., and Murray, S. S. (2001c). Chandra Estimate of the Magnetic Field Strength near the Cold Front in A3667. *apjl*, 549(1):L47–L50.

Voges, W., Aschenbach, B., Boller, T., Bräuninger, H., Briel, U., Burkert, W., Dennerl, K., Englhauser, J., Gruber, R., Haberl, F., Hartner, G., Hasinger, G., Kürster, M., Pfeffermann, E., Pietsch, W., Predehl, P., Rosso, C., Schmitt, J. H. M. M., Trümper, J., and Zimmermann, U. (1997). *The Rosat All-Sky Survey Bright Source Catalog*, pages 433–434. Springer Netherlands.

Walker, S. and Lau, E. (2022). Cluster Outskirts and Their Connection to the Cosmic Web. In *Handbook of X-ray and Gamma-ray Astrophysics*, page 13.

Walker, S. A., Fabian, A. C., and Sanders, J. S. (2014). Large-scale gas sloshing out to half the virial radius in the strongest cool core REXCESS galaxy cluster, RXJ2014.8-2430. *mnras*, 441:L31–L35.

Walker, S. A., Mirakhor, M. S., ZuHone, J., Sanders, J. S., Fabian, A. C., and Diwanji, P. (2022). Is there an enormous cold front at the virial radius of the perseus cluster? *The Astrophysical Journal*, 929:37.

Walker, S. A., Sanders, J. S., and Fabian, A. C. (2016). Applications for edge detection techniques using Chandra and XMM-Newton data: galaxy clusters and beyond. *mnras*, 461(1):684–697.

Walker, S. A., ZuHone, J., Fabian, A., and Sanders, J. (2018). The split in the ancient cold front in the perseus cluster. *Nature Astronomy*, 2(4):292–296.

Wang, Q. H. S., Giacintucci, S., and Markevitch, M. (2018). Bow Shock in Merging Cluster A520: The Edge of the Radio Halo and the Electron-Proton Equilibration Timescale. *apj*, 856(2):162.

Weeren, R. J. v., Röttgering, H. J. A., Brüggen, M., and Hoeft, M. (2010). Particle acceleration on megaparsec scales in a merging galaxy cluster. *Science*, 330:347–349.

Werner, N., ZuHone, J. A., Zhuravleva, I., Ichinohe, Y., Simionescu, A., Allen, S. W., Markevitch, M., Fabian, A. C., Keshet, U., Roediger, E., Ruszkowski, M., and Sanders, J. S. (2016). Deep Chandra observation and numerical studies of the nearest cluster cold front in the sky. *mnras*, 455(1):846–858.

Wik, D. R., Hornstrup, A., Molendi, S., Madejski, G., Harrison, F. A., Zoglauer, A., Grefenstette, B. W., Gastaldello, F., Madsen, K. K., Westergaard, N. J., Ferreira, D. D. M., Kitaguchi, T., Pedersen, K., Boggs, S. E., Christensen, F. E., Craig, W. W., Hailey, C. J., Stern, D., and Zhang, W. W. (2014). NuSTAR Observations of the Bullet Cluster: Constraints on Inverse Compton Emission. *apj*, 792(1):48.

Williamson, R., Benson, B. A., High, F. W., Vanderlinde, K., Ade, P. A. R., Aird, K. A., Andersson, K., Armstrong, R., Ashby, M. L. N., Bautz, M., Bazin, G., Bertin, E., Bleem, L. E., Bonamente, M., Brodwin, M., Carlstrom, J. E., Chang, C. L., Chapman, S. C., Clocchiatti, A., Crawford, T. M., Crites, A. T., de Haan, T., Desai, S., Dobbs, M. A., Dudley, J. P., Fazio, G. G., Foley, R. J., Forman, W. R., Garmire, G., George, E. M., Gladders, M. D., Gonzalez, A. H., Halverson, N. W., Holder, G. P., Holzapfel, W. L., Hoover, S., Hrubes, J. D., Jones, C., Joy, M., Keisler, R., Knox, L., Lee, A. T., Leitch, E. M., Lueker, M., Luong-Van, D., Marrone, D. P., McMahon, J. J., Mehl, J., Meyer, S. S., Mohr, J. J., Montroy, T. E., Murray, S. S., Padin, S., Plagge, T., Pryke, C., Reichardt, C. L., Rest, A., Ruel, J., Ruhl, J. E., Saliwanchik, B. R., Saro, A., Schaffer, K. K., Shaw, L., Shirokoff, E., Song, J., Spieler, H. G., Stalder, B., Stanford, S. A., Staniszewski, Z., Stark, A. A., Story, K., Stubbs, C. W., Vieira, J. D., Vikhlinin, A., and Zenteno, A. (2011). A Sunyaev-Zel'dovich-selected Sample of the Most Massive Galaxy Clusters in the 2500 deg^2 South Pole Telescope Survey. *apj*, 738(2):139.

ZuHone, J. and Su, Y. (2022). The Merger Dynamics of the X-ray Emitting Plasma in Clusters of Galaxies. *arXiv e-prints*, page arXiv:2202.06712.

ZuHone, J. A. (2011). A Parameter Space Exploration of Galaxy Cluster Mergers. I. Gas Mixing and the Generation of Cluster Entropy. *apj*, 728(1):54.

Zuhone, J. A. and Roediger, E. (2016). Cold fronts: probes of plasma astrophysics in galaxy clusters. *Journal of Plasma Physics*, 82(3):535820301.